Universidad Complutense de Madrid Universidad Politécnica de Madrid
Doctorado en Ingeniería Matemática, Estadística e Investigación Operativa

A numerical approach to predict cavitation and contact in misaligned journal bearings

A thesis submitted in partial fulfillment
of the requirements for the degree of

Doctor of Philosophy

Author: Hassán Lombera Rodríguez

Supervisor: Ph.D. José Ignacio Tello del Castillo

Madrid, 2017

If I have seen further, it is by standing on the shoulders of giants

Sir Isaac Newton

Dedicatory

To my family, who always wondered if I would ever finish this thesis

Acknowledgement

I am deeply grateful to my supervisor Prof. J. Ignacio Tello for his invaluable professional guidance, his unconditional support to my work during these years and his cares in Madrid during each stay. He was always there when I needed the help of his knowledge and experience. His thorough revisions has considerably helped me improve the content of this thesis and the papers we have submitted.

I would like to thank all the professors of both Complutense and Polytechnic University of Madrid, who have contributed to increase my academic training in the field of fluid dynamics. Special thanks to: Lourdes Tello, Francisco J. Navarro, J. Ildefonso Díaz, Pedro Galán and Arturo Hidalgo. I must also express my gratitude to Universidad de las Ciencias Informáticas and Universidad de La Habana; both in Havana, Cuba, for my academic training and constant support in order that I could finish this thesis. Special thanks to Prof. Carlos E. Novo, for his essential contribution to the experimental data and support given every time I had doubts about mechanical aspects and expected behaviours of journal bearings.

The present dissertation was only possible due to the invaluable support of many institutions. Thus, this work was partially supported by the Institute for Interdisciplinary Mathematics (IMI), at the Complutense University of Madrid, and by the project MTM2013-42907-P Ministerio de Economía y Competitividad (Spain). I also acknowledge the Iberoamerican University Association for Postgraduate Studies (AUIP) for granting me an academic mobility scholarship to defend this thesis in Madrid.

I would like to thank my wife, Maybel Díaz, for her immense love and encouragement, and for being the strength for me. I am also grateful to all my good friends, who have helped me to accomplish this task with their unfading care, counsel and support. Last but not least, I am grateful to my parents, my brother and my family in general, in particular to my mother, the most beautiful flower in the garden of my life. To those that, mentioned or not, contributed to the fulfilment of the present work, my deep and sincere thanks.

Declaration of Authorship

I hereby declare that except where specific reference is made to the work of others, the contents of this dissertation are original and have not been submitted in whole or in part for consideration for any other degree or qualification in this, or any other University. This dissertation is the result of my own work and includes nothing which is the outcome of work done in collaboration, except where specifically indicated in the text.

Hassán Lombera Rodríguez

November 2017

Abstract

This dissertation presents a numerical approach to reach the equilibrium position of a misaligned journal bearing with radial loading. We consider the hydrodynamic Reynolds equation with cavitation phenomenon, through both Reynolds and Elrod–Adams models. The device consists of an external cylinder surrounding a rotating shaft, both separated by a lubricant to prevent contact. The unknowns are the pressure of the lubricant satisfying a proper cavitation model, and the shaft position which could be misaligned. We couple the hydrodynamic model to Newton's second law, which describes the position of the shaft. This is considered an inverse problem where the coefficient of the equation is given by the unknown shaft position, which depends on the pressure. Considering the Reynolds cavitation model, we solve the direct problem minimizing a convex functional. We use a preconditioned conjugate gradient method modified with projection and restarting strategies to account for cavitation. To solve the associated inverse problem we use an interior, trust-region algorithm subject to bounds, through which we transform the constrained optimization problem into an unconstrained one. The simulations show the existence of contact points for finite loading when misalignment occurs. We provide a mathematical proof for the point contact case. Similarly, we present the admissible range of misalignment angle projections for prescribed values of the shaft eccentricity and angular coordinate. With the Elrod–Adams model, we approximate the Heaviside function by a third order Hermite polynomial and solve the direct problem by minimizing a convex and lower semi continuous functional. To solve the associated inverse problem we introduce Ant Colony Optimization, an approach inspired by the ants' foraging behaviour and communication through pheromone trails. This approach, originally developed to solve discrete optimization problems has been now successfully extended to continuous domains. Numerical results are presented to verify the different numerical approaches. To validate the proposal the predicted pressure values, in the bearing mid-plane, are compared to published experimental data.

Statement

This work describes an original research carried out by the author. Some chapters in this dissertation, however, are inspired by – or partially based on – papers; which the author, together with a number of colleagues, has published or submitted for publication.

List of publications in international journals with impact factor

Lombera, H. and J. I. Tello (2014). "A numerical approach to solve an inverse problem in lubrication theory". In: *RACSAM. Rev. R. Acad. A.* 108.2, pp. 617–631.

Díaz, M., H. Lombera, et al. (2015). "An Approach for Assembly Sequence Planning Based on Max-Min Ant System". In: *IEEE Latin America Transactions* 13.4, pp. 907–912.

Pedraza, G., M. Díaz, and H. Lombera (2016). "An Approach for Assembly Sequence Planning by Genetic Algorithms". In: *IEEE Latin America Transactions* 14.5, pp. 2066–2071.

Lombera, H. (2017). "On the numerical resolution of an inverse problem in misaligned journal bearings with cavitation". Submitted.

Lombera, H. and J. I. Tello (2017a). "Existence of solutions and finite load capacity in misaligned journal bearings with an imposed load". In preparation.

— (2017b). "On the numerical resolution of an inverse problem in misaligned journal bearings with the $ACO_{\mathbb{R}}$ metaheuristic". In preparation.

Contents

List of Figures

List of Tables

List of Algorithms

Introduction

Since ancient times man has been concerned about the power loss of machinery and the wear of parts in relative motion (Dowson, 1979). Nowadays, the research of such phenomena have received increasing attention, due to its multifactorial complexity. The movement process suffers the disturbing influence of the friction, and therefore, a percentage of the energy involved in the movement is used to overcome that friction. In 1996, it was reported that 20% of the power consumed in cars was used in overcoming friction (Pope, 1996).

For decreasing the loss of material and energy as a consequence of this interaction, a major option to consider is to diminish friction between the solid surfaces by introducing a fluid that avoids direct contact. This way, the concept of lubrication emerges. Any analysis of a system consisting of two or more bodies in relative motion that rub to each other, includes the whole study of friction, wear, and lubrication. A new field of science, defined *Tribology* in 1967 by a committee of the Organization for Economic Cooperation and Development, focuses on the study of these factors. *Tribology* is derived from the Greek word *"tribos"* meaning rubbing or sliding (Stachowiak and Batchelor, 2013).

The modern machinery is expected to work at high speed and strain, which forces scientists to carefully consider all phenomena taking place on surfaces in relative motion, namely in friction knots. A special case is a journal bearing, which is a mechanical device consisting of two cylinders closely spaced and in relative motion. The annular gap between them is filled with a fluid, the lubricant, to prevent contact. Journal bearings have been widely used for load support of rotating machinery like gearboxes, pumps, thermal engines or turbo-generators. Ideally, the axes of both cylinders are parallel when installed and remain so during the operation, under an imposed load and speed (Jang and Khonsari, 2015); see Fig. 1a.

Actually, this ideal condition hardly exists and the inner cylinder, the shaft, tends to experience some degree of misalignment while rotating inside the outer cylinder, the bearing; see Fig. 1b.

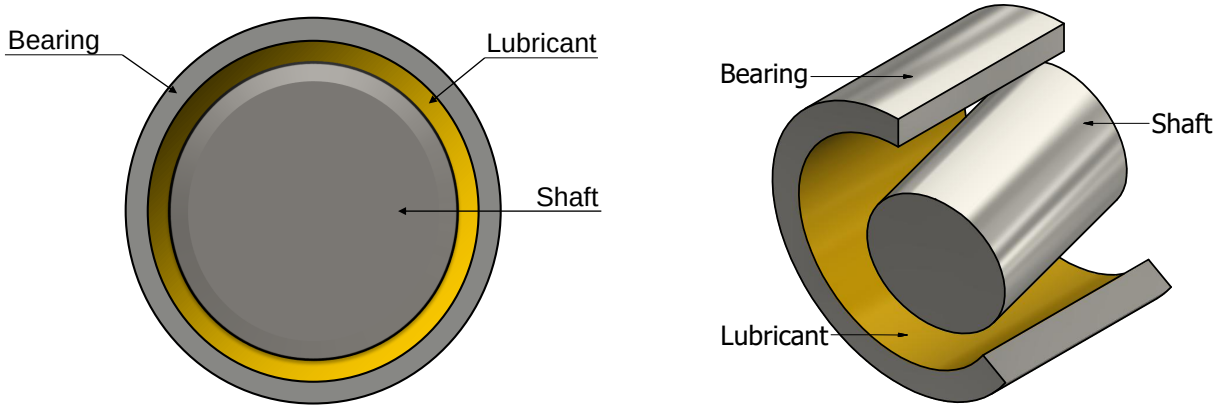

(a) Front view of a perfectly aligned journal bearing.

(b) A misaligned journal bearing.

Figure 1. A schematic for parallel and misaligned journal bearings.

Misalignment is known to have a harmful effect on the steady-state performance of a journal bearing. The principal effect is a reduction in the minimum thickness of the lubricant film. Misalignment could be parallel, angular or even a combination of them. In parallel misalignment, the centre lines of both cylinders are parallel but they are offset while in angular misalignment, the centre lines are at an angle to each other. Thus, the Reynolds Equation (RE) should be modified to allow the variation of the film thickness in both circumferential and axial direction. Substantially, reduced minimum film thickness also alters the entire pressure and temperature fields (Jang and Khonsari, 2015).

On the other hand, if the lubricant film fails, it impairs the relative movement between solid bodies and inevitably causes severe damage to the surfaces in contact. That is why, from the practical engineering view point, prediction of lubricant film behaviour is extremely important. The consequence of the lubricant film failure is severe wear. Depending on the circumstances adhesive wear, fatigue wear, abrasive wear, erosive wear, corrosive wear, oxidative wear, fretting wear, impact wear, melting wear, diffusive wear, or cavitation wear may result. A report published in 1976 revealed that the economic losses caused by friction and wear cost about 10 billions DM in West Germany each year, at 1975 values, which was equivalent to 1% of the Gross National Product (apud Stachowiak and Batchelor, 2013, p. 6). About 50% of these losses were due to abrasive wear. In France, it was assessed by Versailles Project on Advanced Materials and Standards (VAMAS), in last century, that losses due to wear were equivalent to 2% of the Gross National Product. At that time, a failure of a bearing, which usually carried a machine unavailability of 1300 MW power

generating unit, could cost as much as 4 MF per day. Similarly, it was estimated by the American Society of Mechanical Engineers (ASME) that 11% of total US energy consumption could be saved by research and development in the field of *Tribology* (Frêne, Nicolas, et al., 1997). In a recent study on energy used, it was estimated that about 100 EJ (⅓ of all energy produced) is used annually worldwide to overcome friction (Holmberg and Erdemir, 2015). The largest quantities of energy are used by industry (29%) and transportation (27%). The study concluded that in a term of 5 to 9 years it is possible to save the 17.5% of the energy use in road transports by effective implementation of new tribological solutions. This equals to annual energy savings of 11.6 EJ, fuel savings of 330 billion litres and reduction in CO_2 emission by 860 Mt. Similarly, in paper machines, 11% of the total energy used to overcome friction can be saved by the implementation of new tribological technologies (ibid.).

Moreover, cavitation is one of the most relevant processes with important economic implications in industry because of its effects. It is defined by Dowson and C. M. Taylor (1979) as the rupture of the continuous fluid film due to the formation of air bubbles inside, which makes the RE no longer valid in the cavitation area. In practice, it is very difficult to completely avoid cavitation with the conventional journal bearing (Stachowiak and Batchelor, 2013). This condition makes the use of cavitation models mandatory and has motivated several studies by many authors. The two most widely used cavitation models are the Reynolds and the Elrod–Adams models. The main difference between these models, comes from the way to obtain the free boundary that separates lubricated and cavitated areas. The former takes advantage that the pressure in the full filled area is greater than the saturation pressure, inducing the use of the theory of variational inequalities. The problem has been solved numerically by the classical Gauss-Seidel method or a point-overrelaxation method with a projection technique. These approaches seem to be enough in the sense that they solve the problem, but in many real engineering problems the discretization of the geometry of a journal bearing needs to be accomplished by a really fine mesh, which yields not only large and sparse matrices but also ill-conditioned. Under these circumstances, those classical approaches result in very time-consuming tasks, prohibited if the problem is nested inside a large one. For that reason, it would be convenient to take advantage of the underlying mathematical model to choose a proper numerical approach. In addition, for the Reynolds cavitation model, the work of Boedo and Booker (2004) suggests (but no proves) that misaligned bearings have infinite load and moment capacity as the end-plane minimum film thickness

approaches zero, which contradicts finite capacity trends reported in previous numerical and experimental studies; see (Gómez-Mancilla and Nosov, 2002; Vijayaraghavan and Keith, 1990) for instance.

Furthermore, the Elrod–Adams model introduces the hypothesis that the cavitation region is a fluid-air mixture. In this sense, an additional unknown, the saturation of fluid in the mixture appears, representing a multivalued non-linear saturation-pressure relation, posed by the Heaviside operator. Numerical methods for solving this model are mainly based on the characteristics discretization for the non-linear convection term and a duality method for the Heaviside operator approximated by the Yosida regularization; see (Durany, Pereira, and Varas, 2006; Durany and Vázquez, 1992) for instance.

In addition, most of the papers in the literature deal with imposed geometry in the associated RE, i.e. the film thickness h for the journal bearing is a given datum and the unknown is the pressure p. In real engineering applications the position of the shaft in a journal bearing, that defines the function h, is unknown. To obtain h, a new equation is needed; thanks to Newton's second law the problem is well posed. It is considered an inverse problem where the coefficient h depends on the unknown p. In this sense, Ciuperca, Jai, and Tello (2017) performed an equilibrium analysis for a mass-conserving model in presence of cavitation. In their work, the balance of forces allows to obtain the unknown position of the surfaces, defined with one degree of freedom. The general characterization of the behaviour of a misaligned journal bearing is very complex when considering other realistic factors as temperature, elasticity, piezoviscosity, roughness and also including the prediction of its final position. For that reason most researches focus on specific topics. The provided analysis reveals the following:

- When considering cavitation, the solution of the RE in the cavitated area is not longer valid and needs to be changed as well as its numerical resolution.
- To predict the final position of the shaft in a journal bearing with radial loading is of major concern in real engineering applications. It involves the statement of a balance by coupling several mathematical models.
- Existent numerical solutions to the Reynolds cavitation model do not take advantage of the underlying mathematical model, resulting in very time-consuming tasks, prohibited if the problem is nested inside a large one.
- The Elrod–Adams cavitation model involves a non-linearity which makes the coupled problem harder

to solve. Existent algorithms for solving the non-linearity involves an additional iterative algorithm nested to the problem, which complicates the solution.

- When considering both radial and angular misalignment in the analysis, the variation of the film thickness in the circumferential and axial directions needs to be carefully taken into consideration.
- Few research efforts on misalignment effects exist, most of them of numerical nature making the results of such studies too complex to evaluate.
- There is a reference that suggests infinite load and moment capacity as the end-plane minimum film thickness approaches zero for misaligned journal bearings with the Reynolds cavitation model. This result differs markedly from finite capacity trends reported in previous numerical and experimental studies.
- The non-prediction of contact in a journal bearing with radial loading implies the use of such devices in an improper operating regime, leading to foreseeable wear and avoidable economic losses.

Thus, in this context, a **research problem** arises:

How to determine the shaft position and the pressure distribution in a misaligned journal bearing with radial loading, to predict contact and cavitation respectively?

In this thesis, we aim the following **objectives**:

1. To develop a computational algorithm that allows determining the shaft position and the pressure distribution in a misaligned journal bearing with radial loading to predict contact and cavitation, for both Reynolds and Elrod–Adams models.
2. To determine the existence of contact points for finite loading in misaligned journal bearings considering the Reynolds cavitation model.

We hold the following **research hypothesis**:

If after an initial pressure in the lubricant generated by an initial supposed displacement of the shaft axis, we apply our proposed algorithm until reaching the equilibrium between the imposed load and the hydrodynamic load, we can determine the final position of the shaft and the final pressure distribution to predict contact and cavitation in a misaligned journal bearing.

The contributions of the research are the following:

Theoretical

1. The admissible range of misalignment angle projections for prescribed values of the shaft eccentricity and angular coordinate; see Sect. 2.1.2.
2. A theorem and its mathematical proof on the existence of contact points for finite loading in misaligned journal bearings considering the Reynolds cavitation model; see Sect. 3.1.
3. A preconditioned conjugate gradient method modified with both projection and restarting strategies to account for cavitation; see Sect. 3.2.
4. The approximation of the Heaviside function in the Elrod–Adams model by a cubic Hermite polynomial which allows to solve the direct problem by minimizing a convex and lower semi continuous (l.s.c) functional; see Sect. 4.1.2.

Computational

1. The resolution of the inverse problem, considering misalignment and the Reynolds cavitation model, based on an interior trust-region algorithm subject to bounds, through which we transform the constrained optimization problem into an unconstrained one.
2. The resolution of the inverse problem, considering misalignment and the Elrod–Adams cavitation model, based on the Ant Colony Optimization for continuous domain ($ACO_{\mathbb{R}}$).

Scope and outline of the thesis

The dissertation focuses on the prediction of contact and cavitation in a misaligned journal bearing with radial loading and a rigid geometry, considering a stationary regime of a Newtonian, isoviscous, isothermal and incompressible lubricant. Two cavitation models, the Reynolds and the Elrod–Adams models are fully depicted. When considering the latter, an axial feeding groove is added to the mathematical formulation.

The outline of this thesis is the following. In Chap. 1 we present a literature review on hydrodynamic lubrication in journal bearings. In Chap. 2 we provide a deep revision on the mathematical details for the proposed models. In particular, we derive the fluid film thickness model for a misaligned journal bearing and pose two suitable variational formulations for the hydrodynamic problem considering the Reynolds and the Elrod–Adams cavitation models respectively. We also present the admissible range of misalignment angle projections for prescribed values of the shaft eccentricity and angular coordinate. We properly state the

problem of a loaded misaligned journal bearing for stationary regime, considering the balance of force and torque components involved.

In Chap. 3 we state and solve the inverse problem for the Reynolds cavitation model. Namely, we prove the finite load capacity of a misaligned journal bearing for the point contact case. To solve the direct problem, we consider a finite element discretization and accomplish the minimization stage by a Preconditioned Conjugate Gradient Method (PCG), modified with both projection and restarting strategies to account for cavitation. We also explain the resolution of the inverse problem by an interior, trust-region algorithm subject to bounds. Numerical experiments and discussion are also included.

In Chap. 4 we state and solve the inverse problem for the Elrod–Adams cavitation model. We provide the approximation of the Heaviside function and propose a functional whose minimum is the solution to the direct problem. The resolution of the inverse problem, based on $ACO_{\mathbb{R}}$, is also explained. Numerical experiments and discussion are also included.

Conclusions and suggestions for Future work are also provided.

CHAPTER 1

Literature review

1.1 On the beginning of the theory of hydrodynamic lubrication

Hydrodynamic lubrication is a phenomenon characterized by a lubricant flowing in the narrow gap between two closely spaced surfaces in relative motion. Important and well-known scientists, engineers and tribologists investigated in the past the relationship between friction, wear and lubrication, especially applied to journal bearings. Gustave Adolph Hirn (1815-1890), accomplished in 1847 the first experiments on hydrodynamic lubrication and rediscovered the laws of Amontons and of Coulomb. In 1879, Robert Henry Thurston (1839-1903), published the results of his study on friction and lubrication. He showed that, with increasing speed, the friction coefficient of a lubricated bearing diminishes below its static value, passes through a minimum and then increases. He also specified that the speed corresponding to the minimum of friction depends on the load applied to the bearing (Frêne, Nicolas, et al., 1997).

In 1883, Nikolai Pavlovich Petrov (1836-1920) introduced the results of his studies and tests on lubricated bearings. He proved that, among the physical characteristics of an oil, the viscosity has a preponderant role in bearing friction. He stipulated that a fluid film totally separates the surfaces of both shaft and bearing, and that a constant pressure should be produced in this film. Petrov, also looked through the work of Hirn and reused the term of mediate friction to characterize hydrodynamic lubrication (ibid.). In 1885, a remarkable discovery was the existence of hydrodynamic pressure in the lubricant film of a bearing by Beauchamp Tower (1845-1904), which served as a basis for accomplishing the theory of lubrication. For-

tunately, Tower's discovery results provided experimental confirmation to Reynolds, who was working on a hydrodynamic theory of lubrication at that time. The result of this was a theory of hydrodynamic lubrication published in the Proceedings of the Royal Society by Reynolds; see (Reynolds, 1886). In that early work, Reynolds proposed the equation that at present is named after him and provided the first analytical proof that a viscous liquid can physically separate two sliding surfaces by hydrodynamic pressure, resulting in low friction and theoretically zero wear (Stachowiak and Batchelor, 2013). That work represents the seminal paper on Lubrication Theory and in fact, most of mathematical models of hydrodynamic lubrication processes between solid surfaces have the RE as their key point. A rigorous approach for the deduction of the classical linear RE from Navier–Stokes may be found in (Bayada and Chambat, 1986b).

It was not until the beginning of the 20th century that Reynolds theory on hydrodynamic lubrication was used for calculating thrust and journal bearings. In 1902, Richard Stribeck confirmed the hydrodynamic effects and performed the original research into the limits of hydrodynamic lubrication. He proposed the relationship between friction, load, speed and viscosity that is still used today to present the various types of lubrication. The limits of hydrodynamic lubrication are summarized in Fig. 1.1. Three zones can be

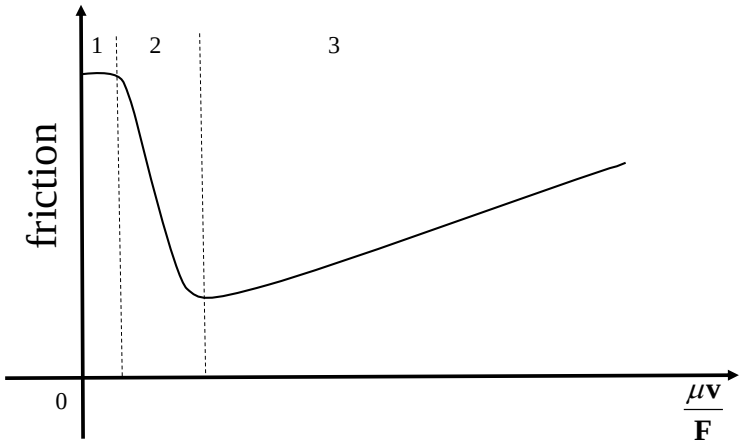

Figure 1.1. Schematic diagram for the limits of hydrodynamic lubrication.

identified, each one corresponding to a type of lubrication depending on the level of pressure established in the contact. For low pressure (0.1 to 50 MPa), zone 1 corresponds to boundary lubrication; surface separation is ensured by lubricant molecules attached to the surfaces; see Fig. 1.2a. This type of lubrication is related to the physico-chemistry of surfaces and of lubricants, for low and moderate speeds and for relatively low loads. In zone 2, the hydrodynamic effect described by RE takes some importance and tends to separate

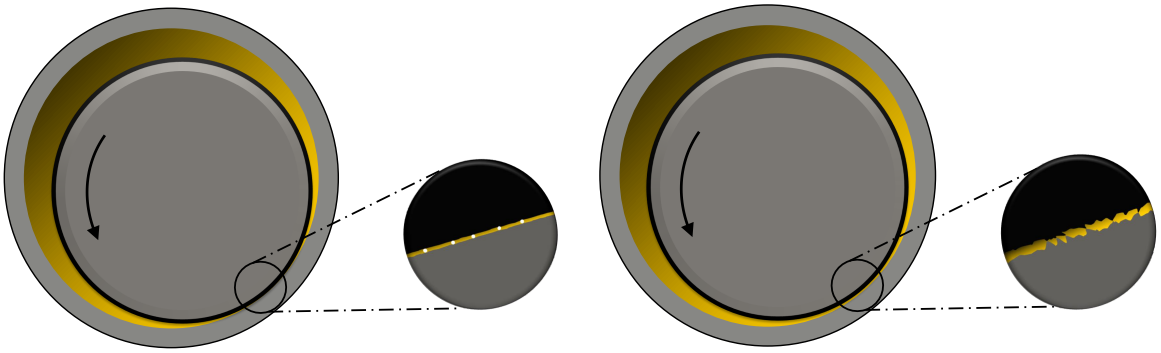

(a) Boundary lubrication regime.

(b) Mixed lubrication regime.

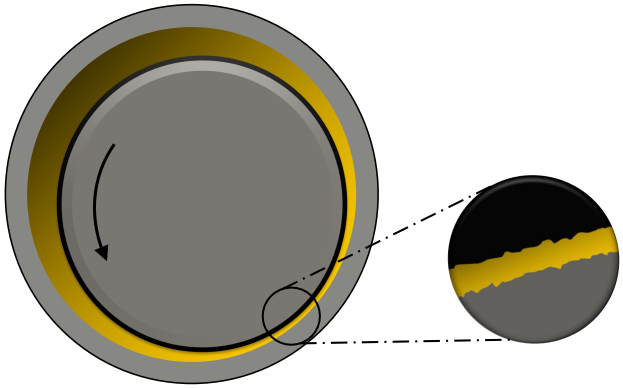

(c) Hydrodynamic lubrication regime.

Figure 1.2. Types of lubrication regimes present on the Stribeck curve.

the areas still in contact over a part of their asperities; this type of lubrication is the mixed lubrication; see Fig. 1.2b. Zone 3 corresponds to hydrodynamic lubrication and is described by RE; see Fig. 1.2c. In this region a full film separates the surfaces and friction is proportional to the speed if the lubricant viscosity is constant with temperature (Frêne, Nicolas, et al., 1997). In general, it was found that when the friction measurements from a journal bearing were plotted on a graph against a controlling parameter defined as $\frac{\mu \mathbf{v}}{\mathbf{F}}$, for all but very small sliding speeds, the friction was proportional to the above parameter which is known as the "Stribeck number" (Stachowiak and Batchelor, 2013).

In 1904, Arnold Johannes Wilhelm Sommerfeld used a change of variables and succeeded in obtaining an analytical solution of the RE for infinitely long journal bearings ($\frac{\partial p}{\partial x} = 0$), where x is in the direction of the journal axis (Frêne, Nicolas, et al., 1997). Nevertheless, the used boundary conditions did not correspond to the physical reality, as they did not take into account the film rupture in the bearing. In addition, the pressure

distribution obtained was negative in the divergent zone of the film. In 1914, Ludwig Karl Friedrich Gümbel suggested that only the positive part of the pressure distribution should be included for the calculation of the bearing load, omitting the negative part. The load calculated was not exact either. Herbert Walker Swift in 1932, and later W. Stieber in 1933 independently presented boundary conditions for film exit, representing the reality in an improved way (Stieber, 1933; Swift, 1932). With their proposals, the fluid film breaks in its divergent zone along the boundary, where the pressure has the value of the saturated pressure and its gradient is zero. Such conditions agree with the continuity of flow at the film exit and are named the boundary conditions of Reynolds. They are universally used for calculating bearings with constant loads (Frêne, Nicolas, et al., 1997). This model considers as interface conditions:

$$p_c = \frac{\partial p}{\partial \mathbf{n}} = 0, \tag{1.1.1}$$

where $\mathbf{n}$ stands for the unitary normal vector to the free boundary. In 1941, a numerical method for solving the RE with such boundary conditions was proposed in (Christopherson, 1941).

In 1953, Fred William Ocvirk proposed to neglect circumferential pressure gradient compared to the axial one in the RE. This way he was presenting his approximate method for short bearing (F. W. Ocvirk and DuBois, 1953). The solution is analytical and uses Gümbel's boundary conditions. The results are almost exact for journal bearings having an L/D ratio (bearing length over diameter) smaller than 0.25. Calculations are in consequence considerably simplified (Frêne, Nicolas, et al., 1997).

A type of slider, with steps, consisting of two parallel parts, but shifted, was described by John William Strutt, Lord Rayleigh. He showed that this type of slider exhibits a load carrying capacity for a given minimum film thickness greater than for any known slider type (ibid.). In 1917, Lord Rayleigh was the first one in calculating the load and the friction torque of a hydrostatic thrust bearing.

The review of all existing papers since the beginning of last century represents a considerable effort that goes beyond the aims of this document. We presented here only a brief review of major achieved progresses in the beginning of hydrodynamic lubrication, that will allow us to succeed *"standing on the shoulders of giants"*.

1.2 Tribology societies, institutes, and authors studying journal bearings

Many *Tribology* societies and institutes, worldwide, have dedicated their efforts to develop advanced studies of lubrication, friction, and wear from the beginning of *Tribology* to the present. Table 1.1 shows a sample of such organizations involved in research in or advocacy of *Tribology*.

Table 1.1. A list of some organizations involved in research in or advocacy of *Tribology*.

- American Bearing Manufacturers Association
- American Gear Manufacturers Association
- American Society of Mechanical Engineers - Tribology Group
- Asociación Argentina de Tribología
- Austrian Center of Competence for Tribology
- Austrian Tribology Society
- Egyptian Society of Tribology
- Finnish Society for Tribology
- French Association for Mechanics - Tribology Group
- Gesellschaft für Tribologie e.V.
- Institution of Engineering and Technology - Tribology Network
- Institut National des Sciences Appliquées de Lyon
- Institution of Mechanical Engineers - Tribology Group
- International Tribology Council
- Italian Tribology Association
- Japanese Society of Tribologists
- Korean Society of Tribologists and Lubrication Engineers
- Malaysian Tribology Society
- Red Temática de Ingeniería de Superficies y Tribología
- Serbian Tribology Society
- Society of Bulgarian Tribologists
- Society of Tribologists and Lubrication Engineers
- South African Institute of Tribology
- Tribology Institute of Chinese Mechanical Engineering Society
- Tribology Society of India

They have all shown their commitment and common interest in advancing the science of *Tribology* and the practice of lubrication engineering. Two institutions, the University of Leeds in England and the *Institut National des Sciences Appliquées de Lyon* in France, have organized the Leeds-Lyon Symposium on *Tribology* for many years, where important scientists from around the world have presented significant results on several tribological phenomena and "best practices" for lubrication fields.

A brief examination of the *Tribology* literature shows that bearings have enjoyed more attention than any other engine component (D. R. Adams, 1991, p. 8). In journal bearings, as in other lubricated devices, it is very important to consider a well suited mathematical model in order to predict the behaviour of the lubricant pressure distribution, the formation of air bubbles near the contact region as well as the gap profile which

balances the hydrodynamic load and a given load vector (Arregui, Cendán, and Vázquez, 2002). These previous facts have widely motivated an increasing study by many authors. Figure 1.3 shows a sample of related groups of authors who have studied different topics on journal bearings. Data have been gathered from Google Scholar and its visualization accomplished by the VOSviewer application (Eck and Waltman, 2015). Each circle represents an author and the size of each circle indicates the activity of the author in terms of publications on journal bearings. The smaller the distance between two authors the higher the number of co-citations. Colors represent groups of related authors.

Accordingly to the bibliography about journal bearings, studied for this work and represented in Fig. 1.3, Guy Bayada, Carlos Vázquez, José Durany, Mohammed Jai, Ionel S. Ciuperca, Sébastien Martin, I. Hafidi, Gustavo Buscaglia, Jean Frêne, Michel Fillon, J. Y. Jang, J. Sun, J. Ignacio Tello, Michael M. Khonsari, and J. F. Booker are the authors with more papers about this topic.

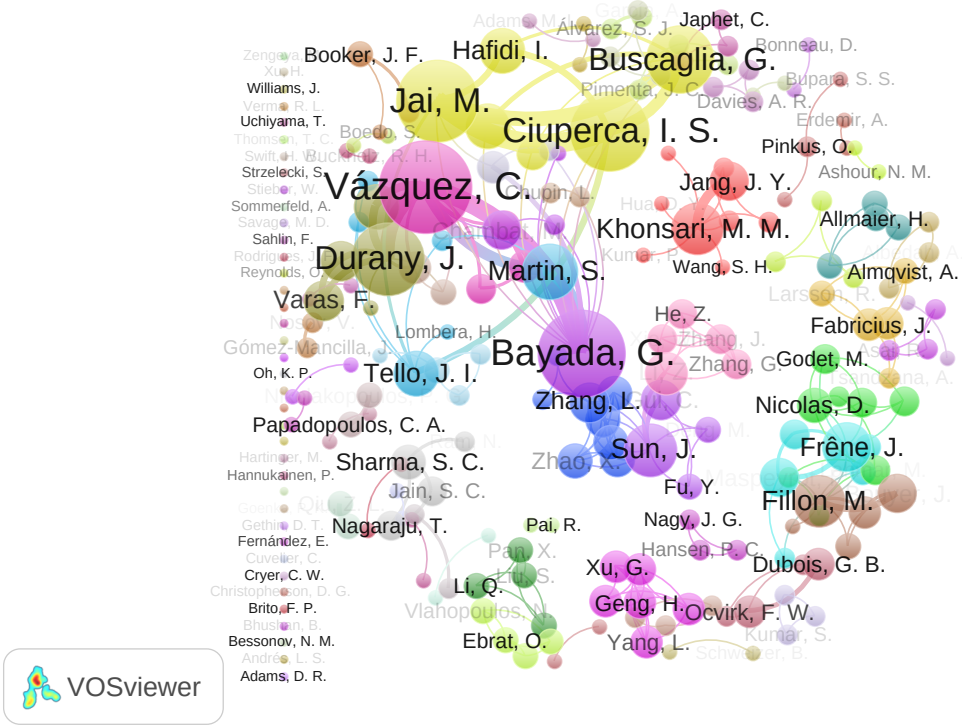

Figure 1.3. Sample of related groups of authors studying journal bearings.

On the other hand, Fig. 1.4 shows which topics have been currently addressed by those researchers, accordingly to the bibliography about journal bearings of this work. Cavitation is definitely included in most

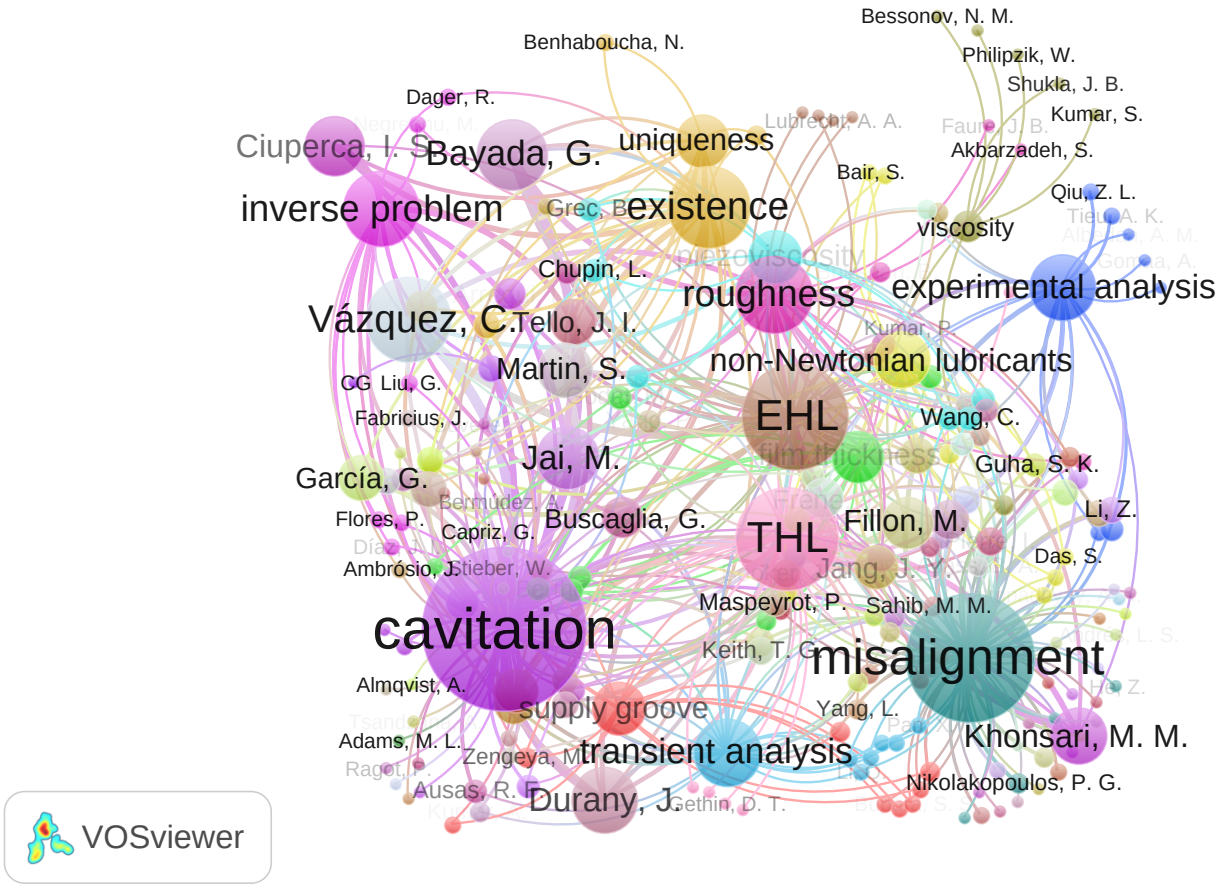

Figure 1.4. Sample of the major topics on journal bearings and researchers working on them.

works. It is expected because it has important economic implications in industry. Other topics have also received attention. Thermohydrodynamic Lubrication (THL) and Elastohydrodynamic Lubrication (EHL), roughness and non-Newtonian lubricants have been deeply studied by the scientific community. Similarly, misalignment has received a lot of attention since it is responsible for most common machine dynamic problems happening in the field. Fig. 1.4 also shows a sample of authors who have worked on the solution of the inverse problem related to journal bearings. Solving this particular problem is really important, as in most interesting real problems the film thickness h is unknown and the data is a function of the pressure. We noticed, in this study, there is not any result that addresses the inverse problem in journal bearing considering cavitation and misalignment at the same time, or at least we are not aware of it.

Section 1.3 provides more details on why these topics: cavitation, misalignment and the inverse problem,

are three of the most significant and are included as fundamentals in this dissertation.

1.3 On misalignment and cavitation in journal bearings

Misalignment

In the case where misalignment is not allowed, the mathematical model assumes that the clearance normalized film thickness, $\bar{h}$, only depends on the circumferential coordinate and is expressed as:

$$\bar{h} = 1 + \bar{\rho}\cos(\theta - \alpha), \tag{1.3.1}$$

where $\bar{\rho} \in [0, 1)$ stands for the normalized shaft eccentricity, α is the shaft angular coordinate and θ represents a point on the external circumference. The assumption posed by Eq. (1.3.1) is equivalent to the supposition that both shaft and bearing axes are perfectly parallel to each other, and that the eccentricity $\bar{\rho}$ does not depend on the axial coordinate. Thus, this expression restricts the physical simulating capacity of the study since in reality it becomes impossible to fully avoid radial and angular misalignments (Gómez-Mancilla and Nosov, 2001). The most common causes of misalignment are elastic and thermal deflections of the shaft and bearing misalignment, as a result of assembly errors. Large misalignment can decrease the bearing clearance and its load capacity. It can increase the temperature and has the potential to reduce the operating velocity threshold (ibid.). In addition, misalignment and residual unbalance are the typical causes for rotor vibration. Both excitations are responsible for most common machine dynamic problems happening in the field.

One of the first documented researches on journal bearing misalignment is reported by S. A. McKee and T. R. McKee (1932), who experimentally observed that measured peak pressures move from the bearing mid-plane towards the bearing ends when the journal is subjected to misalignment. Same result was found by Bouyer and Fillon (2002) in an experimental analysis of misalignment effects on hydrodynamic plain journal bearing performance. They experimentally studied the hydrodynamic plain journal bearing submitted to a misalignment torque. The misalignment caused more significant changes in bearing performance when the rotational speed or load was low (ibid.). Piggott showed that a 40% reduction in bearing load capacity was induced by a 0.0002 rad misalignment. These observations clearly revealed the importance of misalignment in bearing performance (Piggott, 1942). Subsequently, Dubois, Mabie, and F. Ocvirk (1951) showed that the

pressure distribution of a misaligned bearing was not symmetric, and reported that the maximum pressure was located as well at the bearing ends. They observed that when a bearing is subjected to severe misalignment, the maximum pressure increases and the bearing performance deteriorates due to the permanent deformation at bearing ends (ibid.). In presence of cavitation it has been shown that the maximum pressure is shifted to the bearing ends as well. The location of the maximum pressure is influenced by the orientation of the misalignment. Besides, the maximum pressure is greater than that for the aligned bearing and an increase in the degree of misalignment could yield two peak values in the pressure, axially near both ends (Jang and Khonsari, 2015).

Representative numerical studies about loaded misaligned journal bearings by (Asanabe, Akakoski, and Asai, 1971; Gómez-Mancilla and Nosov, 2002; Pinkus and Bupara, 1979; Vijayaraghavan and Keith, 1990) suggest that misaligned bearings have a finite load capacity as the end-plane film thickness goes to zero. Moreover, perfectly aligned journal bearings have a theoretically infinite load capacity, see (Ciuperca, Jai, and Tello, 2009; Pinkus and Sternlicht, 1961) for instance. Conversely, Boedo and Booker (2004) suggest (but no prove) that misaligned bearings have infinite load and moment capacity as the end-plane minimum film thickness approaches zero under transient journal squeeze motion and under steady load and speed conditions. These results differ markedly from finite capacity trends reported in previously mentioned numerical and experimental studies. We show numerically, by finding contact points, that misaligned journal bearings have finite load capacity for the Reynolds cavitation model. A mathematical proof is provided in Sect. 3.1 to demonstrate the finite load capacity of the system for the point contact case.

Nikolakopoulos and Papadopoulos (1994) presented an analysis of misaligned journal bearing operating, considering both the linear and non-linear plain journal bearing characteristics. The Finite Element Method (FEM) was used to solve the RE. They calculated the linear and non-linear dynamic properties for misaligned bearings depending on the developed forces and moments as functions of the displacements and misalignment angles (ibid.).

An analytical solution for misaligned journal bearing axes (short bearing) at its steady-state was obtained in (Gómez-Mancilla and Nosov, 2001). The same approach for modelling misalignment was used in (Gómez-Mancilla and Nosov, 2002). The solution is expanded in series over a small parameter a, which characterizes the non parallelism of journal bearing axes. In our model we characterize misalignment using

an equivalent derivation procedure, but we do not make that power series expansion, in order to propose a general characterization for misaligned journal bearings; see Sect. 2.1.2 for details.

Thus, as a journal bearing almost always operates with some misalignment between its shaft and bearing, it is important to include this issue in the analysis.

Cavitation models. Their numerical resolution

Mathematical models that we consider in Lubrication Theory, assume that the unknown pressure p is constant through the thickness of the fluid film, which allows one to approximate the three dimensional Navier–Stokes equations by the bidimensional RE; see (Bayada and Chambat, 1986b) for details. In presence of cavitation, the RE is no longer valid and this condition makes the use of cavitation models mandatory. A review on the mathematical and physical analysis for different cavitation models is presented in (Bayada and Chambat, 1986a). Also, Álvarez (1986) studied two different models for describing the fluid pressure distribution in journal bearings: a stationary model and a transient model. He considered cavitation and demonstrated uniqueness of the solution.

The common feature of the models lies in the domain decomposition into two parts: a lubricated region and a cavitated region. In the former the RE is verified while in the latter the pressure is taken to be a constant (Bayada and Vázquez, 2007). The main difference between models comes from the way to obtain the free boundary that separates lubricated and cavitated areas. In Sect. 2.3 and Sect. 2.6 we give details on the derivation of both cavitation models.

Several papers have used the theory of variational inequalities taking advantage that the pressure in the full filled area is greater than the saturation pressure. In fact, the idea was reinforced when Cryer justified the work of Christopherson (1941), associating that study to an obstacle problem (Cryer, 1971). This is known as the Reynolds cavitation model (Bayada and Vázquez, 2007). In 1975, Rohde and McAllister presented a variational formulation for hydrodynamic lubrication, from which the associated free boundary problem arose naturally. The Finite Difference Method (FDM) and the FEM were discussed as strategies for obtaining approximate solutions (Rohde and McAllister, 1975). In fact, due to the nature of the Reynolds cavitation model and easy computational approach, it has been used in a large list of mathematical works; see (Capriz and Cimatti, 1983; Cimatti, 1984; Cimatti, 1986; Cuvelier, 1979; Liu, 2004; Rodrigues, 1993)

for instance. In general, for the numerical resolution of this model, techniques based on the FEM have been widely used. The discrete problem has been solved by the classical Gauss-Seidel method or a point-overrelaxation method, including both a projection technique to consider cavitation; see (Calvo, Durany, and Vázquez, 1997; Cuvelier, 1979) for instance. In this work, we also use the Reynolds cavitation model including a FEM discretization. Nevertheless, we solve the system of linear equations by minimizing a convex functional, using a PCG with both projection and restarting strategies. The choice obeys two major reasons: the fact that we solve a convex functional and that matrices resulting from the discretization of Partial Differential Equations (PDE)(e.g. FEM or Finite Volume Method (FVM)), in addition to be sparse are usually ill-conditioned, for which preconditioning is widely recommended.

Another model to describe cavitation is the Elrod–Adams model (Elrod and M. L. Adams, 1975). In that work, the authors introduce the hypothesis that the cavitation region is a fluid-air mixture and an additional unknown ϑ appears (the saturation of fluid in the mixture[1]). This model, which still relies on the RE has been widely used in *Tribology* (Martin, 2008). Unlike some other models, such as the Reynolds cavitation model, it does allow the starvation phenomena to take place. Its interest also relies on the evidence that it is a mass-preserving model. In (Bayada and Chambat, 1986a; Durany and Vázquez, 1992) comparisons for journal bearings are made, between their operating parameters computed by the Reynolds and the Elrod–Adams cavitation models.

Vijayaraghavan and Keith (1989) analysed the effect of cavitation on the performance of a line-grooved misaligned bearing for both flooded and starved inlet conditions. They used the mass-conserving cavitation algorithm in their analysis. They took into account the lubricant rupture and the reformation phenomena. One year later, they showed that at the higher degrees of misalignment, the performance characteristics of the bearing are significantly different from those for an aligned journal bearing (Vijayaraghavan and Keith, 1990).

Numerical methods for solving the Elrod–Adams model for cavitation in different devices and conditions were presented in (Bayada, Chambat, and Vázquez, 1998; Bermúdez and Durany, 1989; Durany and Vázquez, 1992; El Alaoui Talibi and Bayada, 1991), among others. Similarly, numerical experimentations of various schemes based both on stationary upwind methods and pseudo-stationary techniques were conducted

[1] It represents the lubricant concentration

in (Calvo, Durany, and Vázquez, 1997). These methods are mainly based on the characteristics discretization for the non-linear convection term and a duality method for the multivalued non-linear saturation-pressure relation, posed by the Heaviside operator. Namely, they use an approach based on the Method of Characteristics (MC) to discretize a total derivative in the final formulation. This technique was also used in (Durany, García, and Vázquez, 2002; Durany, Pereira, and Varas, 2008; Durany, Pereira, and Varas, 2010; Lombera and Tello, 2014) among others, and it is the strategy chosen to solve our problem as well. Additionally, the first three used a Yosida regularization for the Heaviside operator as in (Bermúdez and Moreno, 1981). In contrast, in (Lombera and Tello, 2014) it is used a regularization of this function by a cubic interpolating Hermite polynomial that allowed to express the solution of the direct problem as a minimum of a convex functional. This approach is also used in the present work.

1.4 The inverse problem. Its numerical resolution

Most of the papers previously mentioned deal with imposed geometry in the associated RE, i.e. the gap function h for the journal bearing is a given datum and the unknown is the pressure p. In real engineering applications the position of the shaft, that defines the gap function h, is unknown. So, Newton's second law is introduced to obtain that position. The problem consists in finding the pressure of the lubricant, its concentration ϑ in the cavitation area and the shaft position. If misalignment is considered, two more variables need to be found, which stand for the angular misalignment projections. The problem is considered as an inverse problem where the coefficient h depends on the unknown p.

J. I. Díaz and Tello (2004) addressed such a problem, considering the simple case in which the surfaces are two parallel planes, and assuming prescribed the total force applied upon one of the surfaces. They provided some sufficient conditions on the total force in order to solve the inverse problem. Ciuperca, Hafidi, and Jai (2006) also studied analytically the inverse problem for a more general geometry. Specifically, they studied the asymptotic behaviour of the position in the evolution problem.

Furthermore, Ciuperca, Jai, and Tello (2009) studied the inverse problem for journal bearings using the Reynolds cavitation model. In that work the inner cylinder is parallel to the exterior one and misalignment is not allowed. They proved the existence of shaft equilibrium positions when the hydrodynamic force created by the pressure film balances an external radial force. The authors proved the non-existence of

contact for any force, even for the case where the shape of the external surface presents some rugosity. Additionally, Ciuperca and Tello considered the problem for both cases, a rigid surface moving over a flat plane and the elastohydrodynamic problem; see (Ciuperca and Tello, 2011a; Ciuperca and Tello, 2011b) for instance. Similarly, Ciuperca, Jai and Tello studied the existence of equilibrium positions for the load problem in Lubrication Theory. In their work, the balance of forces allows to obtain the unknown position of the surfaces, defined with one degree of freedom (Ciuperca, Jai, and Tello, 2017).

As for the numerical resolution of the inverse problem which entails the balance between an imposed load on the device and the hydrodynamic load we can mention the work of (Durany, García, and Vázquez, 2002). They developed a numerical scheme which combines fixed point algorithms, the MC, duality techniques and finite element approximations. In (Durany, Pereira, and Varas, 2010) the authors used an implicit Euler method to deal with the dynamical shaft problem coupled with the fluid hydrodynamic problem. At each time step the resulting non-linear system is solved by the Broyden method combined with the Armijo–Goldstein criterion to choose a proper step length in the descent direction. Conversely, in (Lombera and Tello, 2014) the authors proposed a different approach to deal with the shaft model. It was based on first solving the Elrod–Adams equation for a known position by minimizing a convex and l.s.c functional and then using an iterative method to reach the equilibrium, namely a trust-region strategy. A similar approach will be used in this work for the Reynolds cavitation model. In general, there are a lot of gradient based algorithms for continuous optimization that can be used for solving problems like the one addressed in this work. They allow to find a local minimum, but the optimized function needs to be continuous and differentiable. Thus, their usefulness is limited due to such prerequisites. Line search and trust-region approaches are two of the fundamental strategies in optimization algorithms that must be mentioned; see (Nocedal and Wright, 2006) for a wide explanation on these approaches.

On the other hand, metaheuristics are a family of optimization techniques, which have seen increasingly rapid development and application to numerous problems in computer science and other related fields. Normally, they require the problem to be partitioned into a set of components to look for the solution in an optimal combination or permutation of them. One of the more recent, prominent and actively developed metaheuristic is Ant Colony Optimization (ACO) which was inspired by the ants' foraging behaviour. It was originally introduced by Dorigo (1992), to solve discrete optimization problems where each decision

variable is characterized by a set of components; see (M. Dorigo, Maniezzo, and Colorni, 1996; Stützle and Hoos, 2000) for instance. Many successful implementations of the ACO metaheuristic have been applied to a number of different discrete optimization problems (Liao, 2011). These applications mainly concern NP-hard combinatorial optimization problems including problems in routing (Gambardella, Taillard, and Agazzi, 1999), assembly sequence planning (M. Díaz, Lombera, et al., 2015), bioinformatics (Blum, Vallès, and Blesa, 2008) and many other areas.

ACO was initially designed to solve the Traveling Salesman Problem (TSP), where a salesman must visit a list of cities exactly once, using the shortest possible route. The cities and paths between them can be represented as a connected graph, and the ants move from one city to another following the pheromone trails on the edges. Let $\mathcal{T}_{ij}(t)$ be the trail intensity on edge (i, j) at time t. Then, each ant chooses the next city to visit depending on the intensity of the associated trail. When the ants have completed their city tours, the trail intensity is updated according to:

$$\mathcal{T}_{ij}(t+1) = \varpi\mathcal{T}(t) + \Delta\mathcal{T}_{ij}, \qquad \varpi \in [0, 1], \tag{1.4.1}$$

where ϖ is a coefficient such that $(1 - \varpi)$ represents the evaporation of trail and

$$\Delta\mathcal{T}_{ij} = \sum_{k=1}^{m} \Delta\mathcal{T}_{ij}^{k}, \tag{1.4.2}$$

where $\Delta\mathcal{T}_{ij}^{k}$ is the pheromone quantity laid by the k$^{\text{th}}$ ant on edge (i, j), defined as:

$$\Delta\mathcal{T}_{ij}^{k} = \begin{cases} \frac{1}{W_k}, & \text{if edge } (i, j) \text{ is in the trajectory of the k}^{\text{th}} \text{ ant,} \\ 0, & \text{otherwise,} \end{cases} \tag{1.4.3}$$

with W_k the tour length of the k$^{\text{th}}$ ant (Dorigo, 1992). The transition probability $\mathcal{P}_{ij}^{k}$ from city i to city j for the k$^{\text{th}}$ ant is defined as:

$$\mathcal{P}_{ij}^{k} = \frac{[\mathcal{T}_{ij}]^a [\eta_{ij}]^b}{\sum_{l \in \text{allowed}_k} [\mathcal{T}_{il}]^a [\eta_{il}]^b}, \tag{1.4.4}$$

where $\eta_{ij} = 1/d_{ij}$ is called visibility and d_{ij} is the associated cost to travel from city i to city j; a and b are parameters that control the relative importance of trail versus cost, and allowed_k is the set of allowed cities

the k^{th} ant can move to from city i (Garcia-Najera and Bullinaria, 2007). Genetic Algorithm, Simulated Annealing, Tabu Search and Particle Swarm Optimization are other approaches we find in the literature to deal with combinatorial optimization problems; see for instance (Pedraza, M. Díaz, and Lombera, 2016; Piniganti, 2014; Srinivas and Patnaik, 1994; Y. Zhang, Wang, and Ji, 2015) for a detailed explanation of them.

Since the emergence of these approaches as combinatorial optimization tools, attempts have been made to use them for addressing continuous problems (Socha, 2008). Now, these metaheuristics that were originally developed for combinatorial optimization are adapted to the continuous case. Examples include the Continuous Genetic Algorithm (Chelouah and Siarry, 2000), Enhanced Simulated Annealing (Siarry, Berthiau, et al., 1997), or Enhanced Continuous Tabu Search (Chelouah and Siarry, 1999). There are also included some ant related methods. In this sense, Socha and M. Dorigo (2008), proposed one of the most popular and easy to implement ACO algorithms for continuous domains, called $ACO_{\mathbb{R}}$. It uses a solution archive as a form of pheromone model for the derivation of a probability distribution over the search space. However, its use in problems with many decision variables have some limitations, reported in (Leguizamón and Coello, 2010a). Thus, Leguizamón and Coello (2010b) proposed an Alternative Ant Colony Optimization for continuous domain ($DACO_{\mathbb{R}}$)[2] which could be more appropriate for large scale unconstrained continuous optimization problems. Later on, Liao, Montes de Oca, et al. (2011) proposed an Incremental Ant Colony Optimization with Local Search for continuous domain ($IACO_{\mathbb{R}}$-LS). This algorithm uses a growing solution archive as an extra search diversification mechanism and a local search to intensify the search. Subsequently, Liao, Stützle, et al. (2014) proposed an ACO algorithm for continuous optimization that combines algorithmic components from $ACO_{\mathbb{R}}$, $DACO_{\mathbb{R}}$ and $IACO_{\mathbb{R}}$-LS. They called it Unified Ant Colony Optimization for continuous domain ($UACO_{\mathbb{R}}$). It is unified, because from $UACO_{\mathbb{R}}$, we can instantiate the original $ACO_{\mathbb{R}}$, $DACO_{\mathbb{R}}$ and $IACO_{\mathbb{R}}$-LS algorithms by using specific combinations of the available algorithmic components and parameter settings. Since in our inverse problem, we only deal with four decision variables and considering that $ACO_{\mathbb{R}}$ has proven to be an efficient, versatile and easy to implement tool for continuous optimization, we propose its use in our work. However, we do deal with a large scale direct problem and motivated by the inherent parallelism of the $ACO_{\mathbb{R}}$ and possible computation speed up we suggest an implementation of the

[2] "D" stands for *diversity*

algorithm with parallel regions for time-consuming tasks, using Open Multi-Processing (OpenMP).

1.5 Other notable topics

Moreover, we mention other topics which have also received attention on the subject of misaligned journal bearings. Literature concerning the topics of thermohydrodynamic and elastohydrodynamic lubrication can be found in (Abass and Sahib, 2013; Bouyer and Fillon, 2003; He, J. Zhang, et al., 2012; Kumar and Khonsari, 2009; Pierre, Bouyer, and Fillon, 2002; Pierre, France, et al., 2004; Sun, Deng, et al., 2010; Thomsen and Klit, 2012; Xu, Zhou, et al., 2015). Besides, lubrication is not the only way to decrease the effect of friction; the materials used and the quality of polished surfaces are also of major concern. However, if surfaces are extremely polished, it is probable a contrary trend to decrease load capacity. It has often been observed in engineering practice that there is a risk of sudden seizure if the surface is too smooth. In this sense, it is commonly believed that small asperities play a useful role as a reservoir for the lubricant between asperities (Stachowiak and Batchelor, 2013). The effect of surface roughness on the performance characteristics of bearings can be found in (Guha, 2000; Sharma, Jain, and Nagaraju, 2002). In general, roughness is one of the challenges of the field; see (Bayada, Martin, and Vázquez, 2005a; Bayada, Martin, and Vázquez, 2005b; Bayada, Martin, and Vázquez, 2005c; Bayada, Martin, and Vázquez, 2005d; Bayada, Martin, and Vázquez, 2006; Martin, 2008) and references there in, to study its effects in journal bearings for different scenarios. More recent results on this topic can be found in (Sun, Deng, et al., 2010; Sun, Zhu, et al., 2014).

The current research on journal bearings also includes the applications of non-Newtonian fluids to improve performance of modern machines (Jang and Khonsari, 2015). Such non-Newtonian fluids have shown that the stress is not directly proportional to the shear strain, and the formulation of the governing equations needs to be changed. Literature on non-Newtonian fluids includes the works of (Abass and Sahib, 2013; Boucherit, Lahmar, and Bou-Said, 2008; Das, Guha, and Chattopadhyay, 2002; Jang, Khonsari, and Bair, 2007; Osman, 2001). The general characterization of the behaviour of a misaligned journal bearing considering all mentioned factors and including the prediction of its final position is very complex. For that reason most researches focus on specific topics.

1.6 Partial conclusions on the literature review

After studying the principal authors and the topics they are currently working on journal bearings we can conclude that cavitation is definitely important and it must be included in our research. As for its mathematical formulation many authors use the Reynolds cavitation model based on the variational inequality but others use the Elrod–Adams model. The former is unquestioned easier to implement while the latter entails more difficulties when programming. However, the latter is more realistic as there is evidence that it is a mass-preserving model. We develop our proposal including they two, as we think both have advantages and disadvantages. It is important to remark that for both cavitation models, experiments have yielded the same results when roughness is not considered relevant.

In addition, misalignment has been also addressed by many authors. Its importance is also unquestioned. It is responsible for most common machine dynamic problems happening in the field. Nevertheless, most mathematical models proposed in the literature entail a solution expanded in series over a small parameter a, which characterizes the non parallelism of journal bearing axes. In our model we characterize misalignment using an equivalent derivation procedure, but we do not make that power series expansion, in order to propose a general characterization for misaligned journal bearings. We consider that the torque effect must also be taken into account.

Concerning the inverse problem its solution is really important, as in most interesting real problems in engineering applications the fluid film thickness h is partially unknown and the data is a function of the pressure. We are not aware of any result that addresses the inverse problem in journal bearing considering cavitation and misalignment at the same time. Similarly, we could not find any result that solves the inverse problem of this work by the $ACO_{\mathbb{R}}$ metaheuristic.

Additionally, we must mention other topics which have also received attention in journal bearings. Thermohydrodynamic lubrication, elastohydrodynamic lubrication and roughness are three of the most significant. We plan to include them for future work.

CHAPTER 2

Mathematical modelling

In this chapter we provide a deep revision on the mathematical details of the models used in this dissertation. In particular, we derive the fluid film thickness model for journal bearings, considering both the parallel and the misaligned case. We also derive the RE and the Generalized Reynolds Equation (GRE). Subsequently, we pose two suitable variational formulations for the hydrodynamic problem considering the Reynolds and the Elrod–Adams cavitation models respectively, which we derived in advance. In addition, we present the admissible range of misalignment angle projections for prescribed values of the shaft eccentricity and angular coordinate. We properly state the problem of a loaded misaligned journal bearing for stationary regime, considering the balance of force and torque components involved.

2.1 Fluid film thickness

In this section we depict the formulations of the fluid film thickness of a journal bearing, for the parallel and the misaligned case. Actually, there are similar results that can be found in the literature; see (Frêne, Nicolas, et al., 1997; Gómez-Mancilla and Nosov, 2001) for instance. However, for making the thesis self-contained we present their derivations in this section.

2.1.1 Parallel case

Figure 2.1 depicts the cross section of a journal bearing. The inner cylinder, the shaft of radius R, rotates in counter-clockwise direction at a constant velocity ω, about the X axis. The film pressure generated by the moving surfaces, forces the lubricant through a wedge shaped zone of thickness h, which varies according to the angle α. It is assumed a coordinate system in which "y" represents the circumferential coordinate, "z" is the coordinate across the fluid film and "x" depicts the journal bearing axial dimension, orthogonal to the zy-plane. Let O_b and O_j be the centres of the bearing and shaft respectively. The over line symbol $\overline{}$ denotes a line segment. The origin of coordinate "y" is located over the line segment $\overline{O_bO_j}$, to place the minimum gap of the device at an angle $\Phi = \pi$. Moreover, the reference $z = 0$ is taken on the bearing surface. The model characterizes the parallel misalignment, where the shaft is allowed to move with two degrees of freedom. Let M be a point over the bearing surface, represented by the angular coordinate $\Phi = (\overline{O_bA}, \overline{O_bM})$,

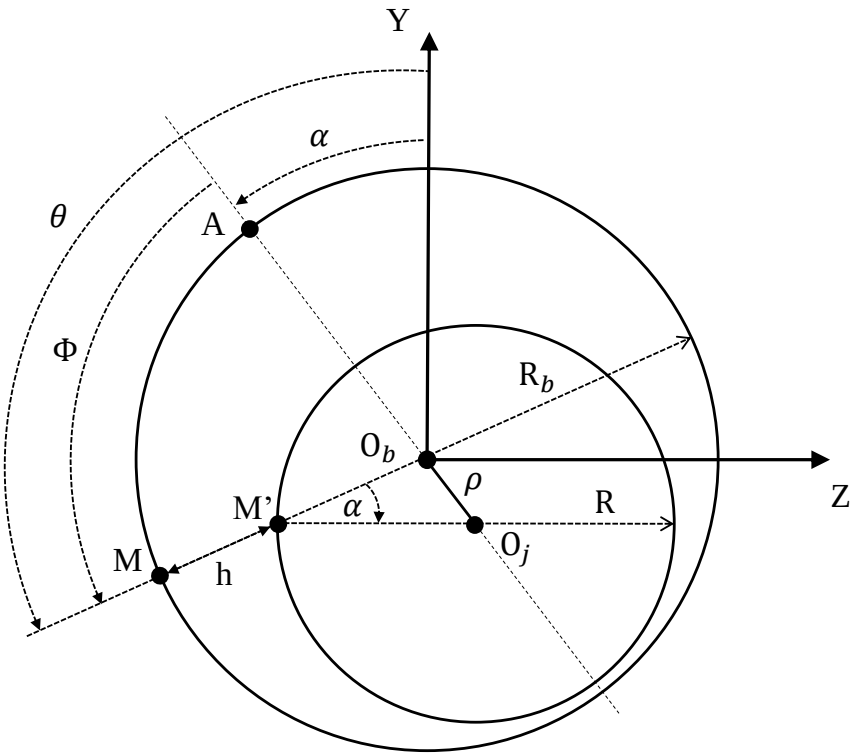

Figure 2.1. Cross section of a journal bearing.

where $\overline{O_bA}$ and $\overline{O_bM}$ are line segments. The fluid film thickness is given by:

$$h = \overline{O_bM} - \overline{O_bM'} = R_b - \overline{O_bM'}. \tag{2.1.1}$$

Applying the sine rule for the triangle $O_jM'O_b$ we have:

$$\frac{\overline{O_jM'}}{\sin(O_jO_bM')} = \frac{R}{\sin(O_jO_bM')} = \frac{R}{\sin(\pi-\Phi)} = \frac{R}{\sin(\Phi)} = \frac{\rho}{\sin(\alpha)}, \tag{2.1.2}$$

where

$$\sin(\alpha) = \frac{\rho}{R}\sin(\Phi) \qquad \text{and} \qquad \overline{O_bM'} = \frac{R}{\sin(\Phi)}\sin(O_bO_jM'). \tag{2.1.3}$$

Notice that:

$$(O_bO_jM') = \Phi - \alpha = \Phi - \arcsin\left(\frac{\rho}{R}\sin(\Phi)\right), \tag{2.1.4}$$

and therefore:

$$\overline{O_bM'} = \frac{R}{\sin(\Phi)}\sin\left(\Phi - \arcsin\left(\frac{\rho}{R}\sin(\Phi)\right)\right). \tag{2.1.5}$$

Taking into account that:

$$\arcsin\left(\frac{\rho}{R}\sin(\Phi)\right) = \arccos\left(\left[1-\left(\frac{\rho}{R}\sin(\Phi)\right)^2\right]^{1/2}\right), \tag{2.1.6}$$

we can calculate the sine of the sum indicated in the Eq. (2.1.5), from which we obtain:

$$\begin{aligned}
\overline{O_bM'} &= \frac{R}{\sin(\Phi)}\left(\sin(\Phi)\cos\left(\arccos\left(\left[1-\left(\frac{\rho}{R}\sin(\Phi)\right)^2\right]^{1/2}\right)\right) - \cos(\Phi)\sin\left(\arcsin\left(\frac{\rho}{R}\sin(\Phi)\right)\right)\right),\\
\overline{O_bM'} &= \frac{R}{\sin(\Phi)}\left(\sin(\Phi)\left[1-\left(\frac{\rho}{R}\sin(\Phi)\right)^2\right]^{1/2} - \cos(\Phi)\frac{\rho}{R}\sin(\Phi)\right),\\
\overline{O_bM'} &= R\left[1-\left(\frac{\rho}{R}\sin(\Phi)\right)^2\right]^{1/2} - \rho\cos(\Phi).
\end{aligned} \tag{2.1.7}$$

Substituting Eq. (2.1.7) in Eq. (2.1.1) we have:

$$h = R_b - \left(R\left[1-\left(\frac{\rho}{R}\sin(\Phi)\right)^2\right]^{1/2} - \rho\cos(\Phi)\right). \tag{2.1.8}$$

Let C be the radial clearance. It must be noticed the relation:

$$\frac{\rho}{R} < \frac{C}{R_b} \ll 1. \tag{2.1.9}$$

Thus, the term $\left(\frac{\rho}{R}\sin(\Phi)\right)^2$ can be neglected compared to unit (Frêne, Nicolas, et al., 1997, p. 116). The fluid film thickness becomes:

$$\begin{aligned} h &\approx R_b - R + \rho\cos(\Phi), \\ h &\approx C + \rho\cos(\Phi). \end{aligned} \tag{2.1.10}$$

In Fig. 2.1 we can notice the relation $\Phi = \theta - \alpha$. Thus, Eq. (2.1.10) can be rewritten as:

$$h \approx C + \rho\cos(\theta - \alpha). \tag{2.1.11}$$

where ρ and α depict the shaft position in polar coordinates and θ represents a point on the external circumference at the height $Y = y$.

The non-dimensional expression

For the non-dimensional expression, we introduce the following non-dimensional variables:

$$\bar{h} = \frac{h}{C}, \qquad \bar{\rho} = \frac{\rho}{C}. \tag{2.1.12}$$

Then, Eq. (2.1.11) can be rewritten as:

$$\bar{h} = 1 + \bar{\rho}\cos(\theta - \alpha), \qquad \bar{\rho} \in [0, 1). \tag{2.1.13}$$

Let $\bar{h}_{min}$ be the minimum value of $\bar{h}$. Notice that it occurs when $\cos(\theta - \alpha) = -1$, so:

$$\bar{h}_{min} = 1 - \bar{\rho}.$$

A contact exists for $\bar{\rho} = 1$.

2.1.2 Misaligned case

In Fig. 2.2 we show the journal bearing axes along with their projections on the xy-plane and xz-plane. The origin O is located at the centre of the bearing "left" end-plane O_b, and the shaft rotates at a constant velocity ω about the X axis. The coordinate system has been rotated, in favour of the graphic comprehension.

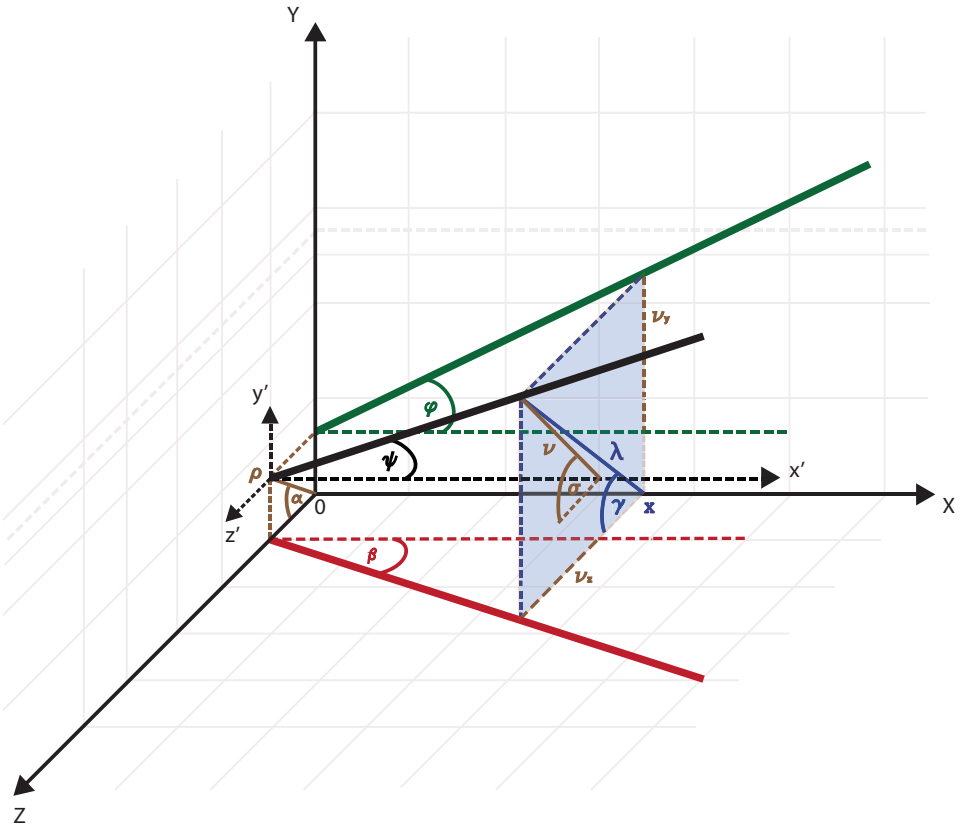

Figure 2.2. Axes and projections in a misaligned journal bearing.

Notice that the axis is rotated an angle ψ, characterized by its projections φ and β on the xy-plane and xz-plane respectively. We create a cross section of the inner cylinder along the plane $X = x$. The cross section is approximated by a circumference. We compute the position of the inner cylinder centre, on that plane, considering the eccentricity λ of its axis. Taking into account the auxiliary coordinate system $(x^{'}, y^{'}, z^{'})$ located in the yz-plane, at the position $(\rho \sin\alpha, \rho \cos\alpha)$, the coordinates of the shaft, on the plane $X = x$, will

be:

$$S_y = v_y + \rho \sin\alpha = x\tan\varphi + \rho\sin\alpha,$$
$$S_z = v_z + \rho \cos\alpha = x\tan\beta + \rho\cos\alpha.$$

Therefore, the eccentricity λ is:

$$\lambda = \left({S_y}^2 + {S_z}^2\right)^{1/2},$$
$$\lambda = \left[(x\tan\varphi + \rho\sin\alpha)^2 + (x\tan\beta + \rho\cos\alpha)^2\right]^{1/2},$$
$$\lambda = \left(x^2\tan^2\varphi + 2x\rho\tan\varphi\sin\alpha + x^2\tan^2\beta + 2x\rho\tan\beta\cos\alpha + \rho^2\right)^{1/2}.$$

We introduce the angle γ, computed as a function of the eccentricity components:

$$\gamma = \arctan\frac{S_y}{S_z},$$
$$\gamma = \arctan\frac{x\tan\varphi + \rho\sin\alpha}{x\tan\beta + \rho\cos\alpha}.$$

By analogy to the parallel case, see Sect. 2.1.1, we approximate the fluid film thickness as follows:

$$h(\rho,\alpha,\varphi,\beta,\theta,x) = C + \lambda(\rho,\alpha,\varphi,\beta,\theta,x)\cos(\theta - \gamma(\rho,\alpha,\varphi,\beta,x)), \tag{2.1.14}$$

where C represents the radial clearance and θ represents a point on the external circumference at the height $Y = y$. To simplify the notation, we drop arguments of function h, λ and γ from now on.

The non-dimensional expression

For the non-dimensional expression, we introduce the following non-dimensional variables in addition to the ones defined in Eq. (2.1.12):

$$\bar{x} = \frac{x}{L}, \qquad \bar{\lambda} = \frac{\lambda}{C}. \tag{2.1.15}$$

Then, Eq. (2.1.14) can be rewritten as:

$$\bar{h} = 1 + \bar{\lambda}\cos(\theta - \bar{\gamma}), \tag{2.1.16}$$

where

$$\bar{\lambda} = \frac{1}{C}\left[(\bar{x}\tan\varphi + C\bar{\rho}\sin\alpha)^2 + (\bar{x}\tan\beta + C\bar{\rho}\cos\alpha)^2\right]^{1/2} \tag{2.1.17}$$

and

$$\bar{\gamma} = \arctan\frac{\bar{x}\tan\varphi + C\bar{\rho}\sin\alpha}{\bar{x}\tan\beta + C\bar{\rho}\cos\alpha}. \tag{2.1.18}$$

Admissible range for the misalignment angle projections given $\bar{\rho}$ and α

In this section we present the admissible range of the misalignment angle projections φ and β to ensure we have no contact for given values of $\bar{\rho}$ and α. In the normalized case, we have one point contact at $\bar{x} = 0$ and $\bar{x} = 1$. The solution of the former is trivial ($\bar{\rho} < 1$) and we will focus on the latter. We have the condition $\bar{\lambda}^2 < 1$ which expands to:

$$(\bar{x}\tan\varphi + C\bar{\rho}\sin\alpha)^2 + (\bar{x}\tan\beta + C\bar{\rho}\cos\alpha)^2 < C^2. \tag{2.1.19}$$

Working on the first term we get

$$(\bar{x}\tan\varphi + C\bar{\rho}\sin\alpha)^2 < C^2.$$

Considering the negative solution and the contact:

$$\begin{aligned} -\tan\varphi - C\bar{\rho}\sin\alpha &< C, \\ -C(1 + \bar{\rho}\sin\alpha) &< \tan\varphi. \end{aligned} \tag{2.1.20}$$

Considering the positive solution and the contact:

$$\begin{aligned} \tan\varphi + C\bar{\rho}\sin\alpha &< C, \\ \tan\varphi &< C(1 - \bar{\rho}\sin\alpha). \end{aligned} \tag{2.1.21}$$

Putting Eq. (2.1.20) and Eq. (2.1.21) together we can set the range for $\tan\varphi$:

$$-C(1+\bar{\rho}\sin\alpha) < \tan\varphi < C(1-\bar{\rho}\sin\alpha). \tag{2.1.22}$$

Following the same procedure we set the range for $\tan\beta$ as a function of $\tan\varphi$:

$$-\left[C^2-(\tan\varphi+C\bar{\rho}\sin\alpha)^2\right]^{1/2} - C\bar{\rho}\cos\alpha < \tan\beta < \left[C^2-(\tan\varphi+C\bar{\rho}\sin\alpha)^2\right]^{1/2} - C\bar{\rho}\cos\alpha. \tag{2.1.23}$$

Note that constraint (2.1.23) was obtained in the same way as the solution of inequality $x^2+y^2<1$, which represents a circle, i.e.

$$-1<x<1, \quad -(1-x^2)^{1/2} < y < (1-x^2)^{1/2}. \tag{2.1.24}$$

2.2 Derivation of the Reynolds Equation

The derivation of the RE can be found in different references; see (Liñan, 1999) for instance. To make this thesis self-contained we provide its derivation in the current section. Thus, we obtain the governing equation for an incompressible fluid, confined at small distance h between a surface and an object that slips on the first one; see Fig. 2.3. For a better understanding of the phenomenon, we will place the coordinate system on the object, as in (ibid.), in such a way that we get a moving surface with respect to the object, that will remain fixed. The following assumptions are used in the analysis. The distance between the surface and the

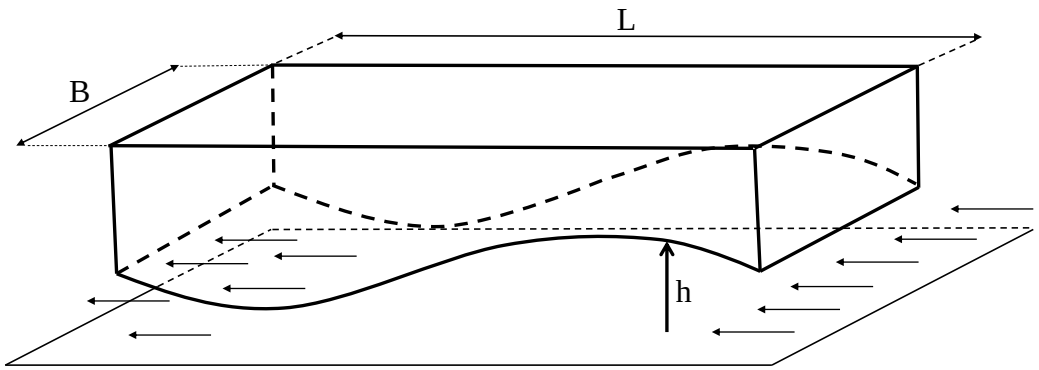

Figure 2.3. A fluid example, confined between a surface and a moving object.

object is assumed to be defined by the function $h(x,t)$, where $0 < h(x,t) < \tilde{H}$, with $\tilde{H}$ the largest distance that can exist between them. Similarly, $0 < h(x,t) \ll L$ and $0 < h(x,t) \ll B$. The origin of the analysis are the conservation principles of Navier-Stokes for incompressible fluids, where $\mathbf{u} = (u, v, w)$ and $\mathbf{v} = (U, V, W)$ stand for the fluid and object velocity vector respectively. Let ϱ, μ, $\mathbf{g}$, p and t be the fluid density, the fluid viscosity, the gravity vector, the fluid pressure and the time respectively.

Mass conservation for incompressible fluids

$$\nabla \cdot (\mathbf{u}) = 0. \tag{2.2.1}$$

Momentum conservation for incompressible fluids

$$\varrho \frac{\partial \mathbf{u}}{\partial t} + \varrho(\mathbf{u}\nabla\mathbf{u}) = -\varrho\mathbf{g} - \nabla p + \frac{\mu}{2}\nabla \cdot (\nabla\mathbf{u} + (\nabla\mathbf{u})^T). \tag{2.2.2}$$

Let $\mathbf{w} = \mathbf{u} - \mathbf{v}$ be the relative velocity between the fluid and the moving object. We rewrite the Eq. (2.2.2) in terms of $\mathbf{w}$:

$$\begin{aligned}
\varrho \frac{\partial}{\partial t}(\mathbf{u} - \mathbf{v}) + \varrho\Big((\mathbf{u} - \mathbf{v})\nabla(\mathbf{u} - \mathbf{v})\Big) &= -\varrho\mathbf{g} - \nabla p + \frac{\mu}{2}\nabla \cdot (\nabla(\mathbf{u} - \mathbf{v}) + (\nabla(\mathbf{u} - \mathbf{v}))^T), \\
\varrho \frac{\partial}{\partial t}(\mathbf{u} - \mathbf{v}) + \varrho\Big((\mathbf{u} - \mathbf{v})\nabla(\mathbf{u} - \mathbf{v})\Big) &= -\varrho\mathbf{g} - \nabla p + \frac{\mu}{2}\nabla \cdot (\nabla\mathbf{u} - \nabla\mathbf{v} + (\nabla\mathbf{u})^T - (\nabla\mathbf{v})^T),
\end{aligned}$$

Since $\mathbf{v}$ only depends on time, $\nabla\mathbf{v}$ vanishes and we obtain:

$$\begin{aligned}
\varrho \frac{\partial \mathbf{u}}{\partial t} - \varrho \frac{\partial \mathbf{v}}{\partial t} + \varrho(\mathbf{u} - \mathbf{v})\nabla\mathbf{u} &= -\varrho\mathbf{g} - \nabla p + \frac{\mu}{2}\nabla \cdot (\nabla\mathbf{u} + (\nabla\mathbf{u})^T), \\
\varrho \frac{\partial \mathbf{u}}{\partial t} + \varrho\mathbf{u}\nabla\mathbf{u} &= \varrho \frac{\partial \mathbf{v}}{\partial t} + \varrho\mathbf{v}\nabla\mathbf{u} - \varrho\mathbf{g} - \nabla p + \frac{\mu}{2}\nabla \cdot (\nabla\mathbf{u} + (\nabla\mathbf{u})^T).
\end{aligned} \tag{2.2.3}$$

We perform a dimensional analysis of Eq. (2.2.1) and Eq. (2.2.3), for computing the order of magnitude of each term. We assume that the dimensions of the object are close, e.g. $\frac{B}{L} \simeq 1$. The distance $h \simeq \tilde{H}$ between the object and the surface is negligible compared to the dimensions of the surface, $\frac{\tilde{H}}{L} \ll 1$ and $\frac{\tilde{H}}{B} \ll 1$.

We assume that the velocity components have variations U_c, V_c, W_c in a characteristic time T_c. Thus, we

have:

$$U_c \sim \frac{L}{T_c}, \tag{2.2.4}$$

$$V_c \sim \frac{B}{T_c}, \tag{2.2.5}$$

$$W_c \sim \frac{\tilde{H}}{T_c}. \tag{2.2.6}$$

Then:

$$\frac{U_c}{W_c} \sim \frac{L}{\tilde{H}}, \quad \frac{W_c}{U_c} \sim \frac{\tilde{H}}{L} \sim 0, \quad \text{since} \quad \tilde{H} \ll L \quad \text{and therefore} \quad W_c \ll U_c.$$

Similarly:

$$\frac{W_c}{V_c} \sim \frac{\tilde{H}}{B} \sim 0, \quad \text{and} \quad W_c \ll V_c.$$

Performing the dimensional analysis in Eq. (2.2.1) we have:

$$\begin{array}{ccccccc} \frac{\partial u}{\partial x} & + & \frac{\partial v}{\partial y} & + & \frac{\partial w}{\partial z} & = & 0, \\ \downarrow & & \downarrow & & \downarrow & & \\ \frac{U_c}{L} & & \frac{V_c}{B} & & \frac{W_c}{\tilde{H}} & & \\ \downarrow & & \downarrow & & \downarrow & & \\ \frac{1}{T_c} & & \frac{1}{T_c} & & \frac{1}{T_c} & & \end{array} \qquad \text{using Eqs. (2.2.4-2.2.6).}$$

Therefore, all terms are comparable and equally important.

Next, we analyse the x component of Eq. (2.2.3). Notice that in this direction there is no gravity component.

$$\begin{array}{ccccccccccccc} \varrho\frac{\partial u}{\partial t} & + & \varrho u\frac{\partial u}{\partial x} & + & \varrho v\frac{\partial u}{\partial y} & + & \varrho w\frac{\partial u}{\partial z} & = & \varrho\frac{\partial U}{\partial t} & + & \varrho U\frac{\partial u}{\partial x} & + & \varrho V\frac{\partial u}{\partial y} & + & \varrho W\frac{\partial u}{\partial z} & - & \frac{\partial p}{\partial x} & + & \frac{\mu}{2}\nabla\cdot(\nabla u+(\nabla u)^T). \\ \downarrow & & \downarrow & & \downarrow & & \downarrow & & \downarrow & & \downarrow & & \downarrow & & \downarrow & & \downarrow & & \downarrow & & \downarrow \\ \varrho\frac{U_c}{T_c} & & \varrho\frac{{U_c}^2}{L} & & \varrho\frac{V_cU_c}{B} & & \varrho\frac{W_cU_c}{\tilde{H}} & & \varrho\frac{U_c}{T_c} & & \varrho\frac{{U_c}^2}{L} & & \varrho\frac{V_cU_c}{B} & & \varrho\frac{W_cU_c}{\tilde{H}} & & \frac{p}{L} & & (\mu\frac{U_c}{L^2} \;\; \mu\frac{U_c}{B^2} \;\; \mu\frac{U_c}{\tilde{H}^2}) \end{array}$$

The dominant term is $\mu\frac{U_c}{\tilde{H}^2}$. When comparing it with the remaining orders, the other terms vanish, except $\frac{p}{L}$

and $\varrho\frac{U_c}{T_c}$. The former, because it involves the unknown, the latter because since T_c is large enough, the term $\frac{U_c}{\tilde{H}^2} \gg \frac{U_c}{T_c}$. Finally, we get:

$$-\frac{\partial p}{\partial x} + \mu\frac{\partial^2 u}{\partial z^2} = 0. \tag{2.2.7}$$

After applying the same analysis for the y component we have:

$$-\frac{\partial p}{\partial y} + \mu\frac{\partial^2 v}{\partial z^2} = 0. \tag{2.2.8}$$

In the case of the z component we firstly analyse the orders of magnitude of Eqs. (2.2.7-2.2.8).

$$\frac{p}{L} = \mu\frac{U_c}{\tilde{H}^2},$$
$$p = \mu\frac{L^2}{\tilde{H}^2 T_c}.$$

Similarly,

$$\frac{p}{B} = \mu\frac{V_c}{\tilde{H}^2},$$
$$p = \mu\frac{B^2}{\tilde{H}^2 T_c}.$$

Then, analysing the z component of Eq. (2.2.3) we obtain:

$$\begin{array}{ccccccccccccccccc}
\varrho\frac{\partial w}{\partial t} & + & \varrho u\frac{\partial w}{\partial x} & + & \varrho v\frac{\partial w}{\partial y} & + & \varrho w\frac{\partial w}{\partial z} & = & \varrho\frac{\partial W}{\partial t} & + & \varrho U\frac{\partial w}{\partial x} & + & \varrho V\frac{\partial w}{\partial y} & + & \varrho W\frac{\partial w}{\partial z} & - & \varrho g & - & \frac{\partial p}{\partial z} & + & \frac{\mu}{2}\nabla\cdot(\nabla w + (\nabla w)^T). \\
\downarrow & & \downarrow & & \downarrow & & \downarrow & & \downarrow & & \downarrow & & \downarrow & & \downarrow & & \downarrow & & \downarrow & & \downarrow & & \downarrow \\
\varrho\frac{W_c}{T_c} & & \varrho\frac{U_c W_c}{L} & & \varrho\frac{V_c W_c}{B} & & \varrho\frac{{W_c}^2}{\tilde{H}} & & \varrho\frac{W_c}{T_c} & & \varrho\frac{U_c W_c}{L} & & \varrho\frac{V_c W_c}{B} & & \varrho\frac{{W_c}^2}{\tilde{H}} & & \varrho g & & \frac{p}{\tilde{H}} & & (\mu\frac{W_c}{L^2} \;\; \mu\frac{W_c}{B^2} \;\; \mu\frac{W_c}{\tilde{H}^2})
\end{array}$$

Applying the orders of magnitude of Eqs. (2.2.7-2.2.8) and the order $\frac{p}{\tilde{H}}$ we get the real order of magnitude of term $\frac{\partial p}{\partial z}$:

$$\begin{array}{ccc}
\frac{\partial p}{\partial z} & & \\
\downarrow & & \\
\frac{L^2}{\tilde{H}^2 T_c \tilde{H}} & \longrightarrow & \frac{L^2}{\tilde{H}^3 T_c},
\end{array}$$

Therefore, it is the dominant term. We can conclude that:

$$-\frac{\partial p}{\partial z} = 0. \tag{2.2.9}$$

Notice the physical meaning of Eq. (2.2.9) under the assumptions used in the derivation: *the pressure variations in the height, are negligible with respect to the pressure variations along the other directions*.

Finally, we obtain the following system of equations:

$$\begin{aligned} \frac{\partial p}{\partial x} + \mu\frac{\partial^2 u}{\partial z^2} &= 0, \\ -\frac{\partial p}{\partial y} + \mu\frac{\partial^2 v}{\partial z^2} &= 0, \\ -\frac{\partial p}{\partial z} &= 0. \end{aligned}$$

with the following boundary conditions:

$$u = v = 0, \quad w = \frac{\partial h}{\partial t}, \quad \text{at} \quad z = h. \tag{2.2.10}$$

$$u - U = v - V = w = W = 0, \quad \text{at} \quad z = 0. \tag{2.2.11}$$

We then integrate the Eq. (2.2.7):

$$\begin{aligned} -\frac{\partial p}{\partial x} + \mu\frac{\partial^2 u}{\partial z^2} &= 0, \\ \mu\frac{\partial^2 u}{\partial z^2} &= \frac{\partial p}{\partial x}, \\ \int_0^z \mu\frac{\partial^2 u}{\partial z^2}\mathrm{d}z &= \int_0^z \frac{\partial p}{\partial x}\mathrm{d}z, \\ \frac{\partial u}{\partial z} &= \frac{1}{\mu}\frac{\partial p}{\partial x}(z + C_1), \\ \int_0^z \frac{\partial u}{\partial z}\mathrm{d}z &= \int_0^z \frac{1}{\mu}\frac{\partial p}{\partial x}(z + C_1)\mathrm{d}z, \\ u &= \frac{1}{\mu}\frac{\partial p}{\partial x}(\frac{z^2}{2} + C_1 z + C_2), \end{aligned}$$

$$u = \frac{z^2}{2\mu}\frac{\partial p}{\partial x} + C_1 z + C_2. \tag{2.2.12}$$

Substituting and evaluating the initial condition $u(0) = U$ we obtain:

$$U = C_2. \tag{2.2.13}$$

Substituting and evaluating the initial condition $u(h) = 0$, together with the result in Eq. (2.2.13) we have:

$$\begin{aligned} 0 &= \frac{h^2}{2\mu}\frac{\partial p}{\partial x} + C_1 h + U, \\ C_1 &= \frac{-U - \frac{h^2}{2\mu}\frac{\partial p}{\partial x}}{h}, \\ C_1 &= -\frac{U}{h} - \frac{h}{2\mu}\frac{\partial p}{\partial x}. \end{aligned} \tag{2.2.14}$$

Substituting results from Eq. (2.2.14) and Eq. (2.2.13) in Eq. (2.2.12) we obtain:

$$\begin{aligned} u &= \frac{z^2}{2\mu}\frac{\partial p}{\partial x} + \Big[-\frac{U}{h} - \frac{h}{2\mu}\frac{\partial p}{\partial x}\Big] z + U, \\ u &= \frac{z^2}{2\mu}\frac{\partial p}{\partial x} - \frac{U}{h}z - \frac{h}{2\mu}\frac{\partial p}{\partial x}z + U, \\ u &= \frac{1}{2\mu}\frac{\partial p}{\partial x} z(z-h) + U(1 - \frac{z}{h}). \end{aligned} \tag{2.2.15}$$

Similarly, we obtain the expression for the v component:

$$v = \frac{1}{2\mu}\frac{\partial p}{\partial y} z(z-h) + V(1 - \frac{z}{h}). \tag{2.2.16}$$

This way, we obtain the expressions for the velocity components in terms of the pressure gradient and the object velocity. Then, we must find p which is independent of z. Therefore, we define the flow rate q_i as the amount of fluid flowing in the direction i, from 0 to h. The flow rate q_x is:

$$q_x = \int_0^h u \mathrm{d}z = \int_0^h \Big(\frac{1}{2\mu}\frac{\partial p}{\partial x} z(z-h) + U(1 - \frac{z}{h}) \Big) \mathrm{d}z,$$

$$
\begin{aligned}
&= \frac{h^3}{6\mu}\frac{\partial p}{\partial x} - \frac{h^3}{4\mu}\frac{\partial p}{\partial x} + Uh - \frac{Uh}{2}, \\
&= \frac{Uh}{2} + \frac{2h^3\frac{\partial p}{\partial x} - 3h^3\frac{\partial p}{\partial x}}{12\mu}, \\
&= \frac{Uh}{2} - \frac{h^3}{12\mu}\frac{\partial p}{\partial x}.
\end{aligned} \tag{2.2.17}
$$

Similarly, we found the expression for the flow rate q_y:

$$
q_y = \int_0^h v\mathrm{d}z = \frac{Vh}{2} - \frac{h^3}{12\mu}\frac{\partial p}{\partial y}. \tag{2.2.18}
$$

We now substitute the expressions for u, v, w in the mass conservation Eq. (2.2.1), and we integrate along the z direction:

$$
\int_0^h \frac{\partial u}{\partial x}\mathrm{d}z + \int_0^h \frac{\partial v}{\partial y}\mathrm{d}z + \int_0^h \frac{\partial w}{\partial z}\mathrm{d}z = 0. \tag{2.2.19}
$$

We then apply the Leibniz's integral rule for the first two terms:

$$
\frac{\partial}{\partial x}\int_0^h u\mathrm{d}z - u(h)\frac{\partial h}{\partial x} + u(0)\frac{\partial 0}{\partial x} + \frac{\partial}{\partial y}\int_0^h v\mathrm{d}z - v(h)\frac{\partial h}{\partial y} + v(0)\frac{\partial 0}{\partial y} + w\Big|_0^h = 0.
$$

Since $u(h) = v(h) = \frac{\partial 0}{\partial x} = \frac{\partial 0}{\partial y} = 0$ and $w(h) = \frac{\partial h}{\partial t}$ we have:

$$
\frac{\partial}{\partial x}\int_0^h u\mathrm{d}z + \frac{\partial}{\partial y}\int_0^h v\mathrm{d}z + \frac{\partial h}{\partial t} = 0. \tag{2.2.20}
$$

Substituting the flow rates of Eq. (2.2.17) and Eq. (2.2.18) in Eq. (2.2.20) we obtain:

$$
\begin{aligned}
\frac{\partial}{\partial x}\Big(\frac{Uh}{2} - \frac{h^3}{12\mu}\frac{\partial p}{\partial x}\Big) + \frac{\partial}{\partial y}\Big(\frac{Vh}{2} - \frac{h^3}{12\mu}\frac{\partial p}{\partial y}\Big) + \frac{\partial h}{\partial t} &= 0, \\
\frac{\partial}{\partial x}\Big(\frac{Uh}{2}\Big) - \frac{\partial}{\partial x}\Big(\frac{h^3}{12\mu}\frac{\partial p}{\partial x}\Big) + \frac{\partial}{\partial y}\Big(\frac{Vh}{2}\Big) - \frac{\partial}{\partial y}\Big(\frac{h^3}{12\mu}\frac{\partial p}{\partial y}\Big) + \frac{\partial h}{\partial t} &= 0, \\
6\mu\frac{\partial}{\partial x}(Uh) - \frac{\partial}{\partial x}\Big(h^3\frac{\partial p}{\partial x}\Big) + 6\mu\frac{\partial}{\partial y}(Vh) - \frac{\partial}{\partial y}\Big(h^3\frac{\partial p}{\partial y}\Big) + 12\mu\frac{\partial h}{\partial t} &= 0,
\end{aligned}
$$

from which we obtain the well-known RE for incompressible fluids:

$$-\nabla \cdot (h^3 \nabla p) = -6\mu \nabla \cdot (h\mathbf{v}) - 12\mu \frac{\partial h}{\partial t}, \tag{2.2.21}$$

where:

h : stands for the fluid film thickness,

μ : stands for the fluid viscosity,

$\mathbf{v}$: stands for the velocity of the moving object.

□

2.3 The Reynolds cavitation model

In this section we present the governing equations in a stationary regime for the hydrostatic pressure in a journal bearing, considering a small fluid film thickness and the cavitation phenomenon. Namely, we introduce the Reynolds cavitation model, which includes boundary conditions for film exit that were previously proposed in the works of Swift and Stieber; see (Stieber, 1933; Swift, 1932). In fact, this model is known as Reynolds cavitation model or Swift-Stieber model.

Let L, R be the length and the cross section radius respectively of the shaft. We consider the circumferential coordinate unfolded $y \in (0, 2\pi R)$ and the axial dimension $x \in [0, L]$. We define the region $\Omega : [0, 2\pi R] \times [0, L]$. The unknowns of the problem are:

$$\begin{aligned}
&p(y, x) : \Omega \to \mathbb{R}^+, && \text{fluid pressure,} \\
&\rho \in [0, C), && \text{left end-plane eccentricity,} \\
&\alpha \in [0, 2\pi], && \text{left end-plane angular position,} \\
&\beta \in [-2C/L, 2C/L], && \text{misalignment angle projection on } xz\text{-plane,} \\
&\varphi \in [-2C/L, 2C/L], && \text{misalignment angle projection on } xy\text{-plane,}
\end{aligned} \tag{2.3.1}$$

and they satisfy the constraint

$$C^2 > \lambda^2,$$

i.e.

$$C^2 > x^2 \tan^2\beta + 2x\rho \tan\varphi \sin\alpha + x^2 \tan^2\beta + 2x\rho \tan\beta \cos\alpha + \rho^2.$$

Under certain operating conditions of a journal bearing, the fluid pressure can reach a minimum value, related to the lubricant vapour pressure. Below this value, cavitation occurs, and the cavitated area is filled by a vapour at a constant pressure p_c. We will consider $p_c = 0$ as an approximation of the pressure value at which the phenomenon occurs. In this region the RE is no longer valid and a cavitation model is needed to describe the phenomenon. We look for a function $p \geq 0$ in Ω satisfying the RE, where $p > 0$ (the lubricated region). We assume there is not mass exchange through the free boundary which separates both regions (the lubricated region and the cavitated region) and we consider $\partial p/\partial \mathbf{n} = 0$, with $\mathbf{n}$ the unitary normal vector to the free boundary. We then use the Reynolds cavitation model to describe this phenomenon, whose weak formulation is given by the following inequality:

$$\int_\Omega h^3 \nabla p \nabla(\phi - p) \mathrm{d}y\mathrm{d}x \geq \int_\Omega 6\mu h \mathbf{v} \nabla(\phi - p) \mathrm{d}y\mathrm{d}x \quad \forall \phi \in K, \tag{2.3.2}$$

with

$$K = \left\{ \phi \geq 0,\ \left(\int_\Omega (\nabla\phi)^2 \mathrm{d}y\mathrm{d}x \right)^{1/2} + \left(\int_\Omega \phi^2 \mathrm{d}y\mathrm{d}x \right)^{1/2} < \infty,\ \phi(y,0) = \phi(y,L) = p_\mathrm{a} \right\}, \tag{2.3.3}$$

p_a = atmospheric pressure.

In Eq. (2.3.2), μ stands for the fluid viscosity, h stands for the fluid film thickness and the velocity $\mathbf{v} = (U, V, W)$ makes reference to the shaft velocity vector. For steady-state bearing operation the shaft presents only one non-zero velocity component, $W = \omega R$, with ω the angular velocity. Then Eq. (2.3.2) becomes:

$$\int_\Omega h^3 \nabla p \nabla(\phi - p) \mathrm{d}y\mathrm{d}x \geq \int_\Omega 6\mu h W \frac{\partial(\phi - p)}{\partial y} \mathrm{d}y\mathrm{d}x, \quad \forall \phi \in K, \tag{2.3.4}$$

defined in Eq. (2.3.3).

We define the bilinear form a and the function f by:

$$\begin{aligned} a(u,v) &:= \int_\Omega h^3 \nabla u \nabla v \mathrm{d}y\mathrm{d}x, \\ f &:= -6\mu\nabla\cdot(h\mathbf{v}) \in H^{-1}(\Omega), \end{aligned}$$

and reformulate Eq. (2.3.4) as follows:

$$a(u, v-u) \quad \geq \quad < f, v-u > .$$

We express the problem as a minimization problem of the following convex functional,

$$J(v) \quad = \quad \frac{1}{2}a(v,v) - < f, v > \text{ on } K. \tag{2.3.5}$$

Taking the parameters of Eq. (2.3.4) and substituting them in Eq. (2.3.5) we obtain the dimensional functional to minimize:

$$J(\phi) \quad = \quad \frac{1}{2}\int_\Omega h^3 (\nabla\phi)^T \nabla\phi \mathrm{d}y\mathrm{d}x \; - \; \int_\Omega 6\mu h W \frac{\partial\phi}{\partial y}\mathrm{d}y\mathrm{d}x, \tag{2.3.6}$$

with h defined in Eq. (2.1.14).

2.3.1 The non-dimensional Reynolds cavitation model

To make our solution to suffice for a variety of different problems, we introduce the following non-dimensional variables in addition to the ones defined in Eq. (2.1.12) and Eq. (2.1.15):

$$\theta = \tfrac{y}{R}, \qquad \mathrm{d}y = R\mathrm{d}\theta, \qquad \mathrm{d}x = L\mathrm{d}\bar{x},$$

$$\bar{z} = \tfrac{z}{h}, \qquad \bar{\phi} = \tfrac{C^2}{\mu_0\omega R^2}\phi, \qquad \bar{p} = \tfrac{C^2}{\mu_0\omega R^2}p, \tag{2.3.7}$$

$$\bar{\mu} = \tfrac{\mu}{\mu_0}, \qquad \overline{W} = \tfrac{W}{\omega R}, \qquad \bar{\lambda} = \tfrac{\lambda}{C},$$

where μ_0 stands for the reference viscosity. Thus, we transform our domain into the dimensionless domain $\bar{\Omega} = [0, 2\pi] \times [0, 1]$ for the $(\theta, \bar{x})$ coordinates. Then, the dimensionless equation for the functional in Eq. (2.3.6) is:

$$J(\bar{\phi}) = \frac{1}{2} \int_{\bar{\Omega}} LR\bar{h}^3 (\nabla\bar{\phi})^T \nabla\bar{\phi} \mathrm{d}\theta \mathrm{d}\bar{x} \; - \; \int_{\bar{\Omega}} 6\bar{\mu}\bar{h}\overline{W} \frac{\mu_0 \omega L R^2}{C^2} \frac{\partial\bar{\phi}}{\partial\theta} \mathrm{d}\theta \mathrm{d}\bar{x}, \tag{2.3.8}$$

with $\bar{h}$ defined in Eq. (2.1.16):

2.4 Derivation of the Generalized Reynolds Equation

The derivation of the GRE is a well-known result that can be found in the literature; see (Dowson, 1962) for instance. However, we provide its derivation in the current section to make the thesis self-contained. The geometry and coordinate system are shown in the cross section of a journal bearing shown in Fig. 2.1. Suffixes 1 and 2 will be used to denote conditions on surfaces $z = 0$ and $z = h$ respectively. The following assumptions are used in the analysis as in (ibid.):

1. The radius of curvature of the bearing components is large compared with the film thickness.
2. The lubricant is a Newtonian fluid.
3. Inertia and body force terms are small compared with the viscous and pressure terms in the equations of motion.
4. Owing to the geometry of the fluid film the derivatives of u and v with respect to z are large compared with all other velocity gradients.
5. There is no slip between the fluid and boundary solids at common boundaries.

After applying an order of magnitude analysis to the Navier-Stokes equations for Newtonian fluids we obtain the following system of equations. See Section 2.2 for details:

$$\frac{\partial p}{\partial x} = \frac{\partial}{\partial z}\left(\mu \frac{\partial u}{\partial z}\right), \tag{2.4.1}$$

$$\frac{\partial p}{\partial y} = \frac{\partial}{\partial z}\left(\mu \frac{\partial v}{\partial z}\right), \tag{2.4.2}$$

$$\frac{\partial p}{\partial z} = 0. \tag{2.4.3}$$

The gradient of the velocity component u across the film can be found by integrating Eq. (2.4.1).

$$\begin{aligned} \int_0^z \frac{\partial}{\partial z}\left(\mu \frac{\partial u}{\partial z}\right) \mathrm{d}z &= \int_0^z \frac{\partial p}{\partial x} \mathrm{d}z, \\ \frac{\partial u}{\partial z} &= \frac{\partial p}{\partial x}\frac{z}{\mu} + \frac{B(x,y)}{\mu}. \end{aligned} \tag{2.4.4}$$

Integrating again, introducing the following boundary conditions

$$z = 0, \qquad u = U_1, \qquad v = V_1, \tag{2.4.5}$$

$$z = h, \qquad u = U_2, \qquad v = V_2, \tag{2.4.6}$$

we have:

$$\begin{aligned} \int_0^h \frac{\partial u}{\partial z} \mathrm{d}z &= \int_0^h \frac{\partial p}{\partial x}\frac{z}{\mu} \mathrm{d}z + \int_0^h \frac{B(x,y)}{\mu} \mathrm{d}z, \\ u\Big|_0^h &= \frac{\partial p}{\partial x} \int_0^h \frac{z}{\mu} \mathrm{d}z + B(x,y) \int_0^h \frac{1}{\mu} \mathrm{d}z, \\ B(x,y) &= \frac{U_2 - U_1}{\int_0^h \frac{1}{\mu} \mathrm{d}z} - \frac{\partial p}{\partial x} \frac{\int_0^h \frac{z}{\mu} \mathrm{d}z}{\int_0^h \frac{1}{\mu} \mathrm{d}z}. \end{aligned} \tag{2.4.7}$$

Defining

$$F_0 = \int_0^h \frac{1}{\mu} \mathrm{d}z, \qquad F_1 = \int_0^h \frac{z}{\mu} \mathrm{d}z, \tag{2.4.8}$$

we have:

$$B(x,y) = \frac{U_2 - U_1}{F_0} - \frac{\partial p}{\partial x}\frac{F_1}{F_0}. \tag{2.4.9}$$

The equation for the u component would be:

$$u(z) = u(0) + \frac{\partial p}{\partial x} \int_0^z \frac{z}{\mu} \mathrm{d}z + B(x,y) \int_0^z \frac{1}{\mu} \mathrm{d}z. \tag{2.4.10}$$

Substituting the proper boundary condition from Eq. (2.4.6) and Eq. (2.4.9) in Eq. (2.4.10) we have:

$$u(z) = U_1 + \frac{\partial p}{\partial x}\int_0^z \frac{z}{\mu}\mathrm{d}z + \left(\frac{U_2 - U_1}{F_0} - \frac{\partial p}{\partial x}\frac{F_1}{F_0}\right)\int_0^z \frac{1}{\mu}\mathrm{d}z. \tag{2.4.11}$$

Similarly, the equation for the v component after applying the proper boundary conditions is:

$$v(z) = V_1 + \frac{\partial p}{\partial y}\int_0^z \frac{z}{\mu}\mathrm{d}z + \left(\frac{V_2 - V_1}{F_0} - \frac{\partial p}{\partial y}\frac{F_1}{F_0}\right)\int_0^z \frac{1}{\mu}\mathrm{d}z. \tag{2.4.12}$$

We then return to the continuity equation and perform an integration with respect to z between the limits 0 and h:

$$\int_0^h \frac{\partial \varrho}{\partial t}\mathrm{d}z + \int_0^h \frac{\partial(\varrho u)}{\partial x}\mathrm{d}z + \int_0^h \frac{\partial(\varrho v)}{\partial y}\mathrm{d}z + \int_0^h \frac{\partial(\varrho w)}{\partial z}\mathrm{d}z = 0. \tag{2.4.13}$$

We then apply the Leibniz's integral rule:

$$\int_{h_1}^{h_2} \frac{\partial f(x,y,z)}{\partial x}\mathrm{d}z = \frac{\partial}{\partial x}\int_{h_1}^{h_2} f(x,y,z)\mathrm{d}z - f(x,y,h_2)\frac{\partial h_2}{\partial x} + f(x,y,h_1)\frac{\partial h_1}{\partial x},$$

which gives:

$$\int_0^h \frac{\partial \varrho}{\partial t}\mathrm{d}z + \frac{\partial}{\partial x}\int_0^h (\varrho u)\mathrm{d}z + \frac{\partial}{\partial y}\int_0^h (\varrho v)\mathrm{d}z - (\varrho U)_2\frac{\partial h}{\partial x} - (\varrho V)_2\frac{\partial h}{\partial y} + [\varrho w]_0^h = 0. \tag{2.4.14}$$

The integrals of (ϱu) and (ϱv) are evaluated by parts to give:

$$\begin{aligned}\int_0^h \frac{\partial \varrho}{\partial t}\mathrm{d}z &+ \frac{\partial}{\partial x}\left[(\varrho u z)\Big|_0^h - \int_0^h z\left(\frac{\partial \varrho}{\partial z}u + \frac{\partial u}{\partial z}\varrho\right)\mathrm{d}z\right] \\ &+ \frac{\partial}{\partial y}\left[(\varrho v z)\Big|_0^h - \int_0^h z\left(\frac{\partial \varrho}{\partial z}v + \frac{\partial v}{\partial z}\varrho\right)\mathrm{d}z\right] \\ &- (\varrho U)_2\frac{\partial h}{\partial x} - (\varrho V)_2\frac{\partial h}{\partial y} + [\varrho w]_0^h = 0.\end{aligned} \tag{2.4.15}$$

We then expand and simplify to obtain:

$$\int_0^h \frac{\partial \varrho}{\partial t}\mathrm{d}z + h\left[\frac{\partial(\varrho U)_2}{\partial x} + \frac{\partial(\varrho V)_2}{\partial y}\right] - \frac{\partial}{\partial x}\int_0^h \left(zu\frac{\partial \varrho}{\partial z} + z\varrho\frac{\partial u}{\partial z}\right)\mathrm{d}z$$

$$-\frac{\partial}{\partial y}\int_0^h \left(zv\frac{\partial \varrho}{\partial z} + z\varrho\frac{\partial v}{\partial z}\right)\mathrm{d}z + [\varrho w]_0^h = 0. \tag{2.4.16}$$

Substituting Eq. (2.4.4) and Eq. (2.4.11) in term $-\frac{\partial}{\partial x}\int_0^h \left(zu\frac{\partial \varrho}{\partial z} + z\varrho\frac{\partial u}{\partial z}\right)\mathrm{d}z$ of Eq. (2.4.16):

$$\begin{aligned}
&-\frac{\partial}{\partial x}\int_0^h z\frac{\partial \varrho}{\partial z}\left(U_1 + \frac{\partial p}{\partial x}\int_0^z \frac{z}{\varrho}\mathrm{d}z + \left(\frac{U_2-U_1}{F_0} - \frac{\partial p}{\partial x}\frac{F_1}{F_0}\right)\int_0^z \frac{1}{\mu}\mathrm{d}z\right)\mathrm{d}z \\
&-\frac{\partial}{\partial x}\int_0^h z\varrho\left(\frac{\partial p}{\partial x}\frac{z}{\mu} + \frac{1}{\mu}\left[\frac{U_2-U_1}{F_0} - \frac{\partial p}{\partial x}\frac{F_1}{F_0}\right]\right)\mathrm{d}z = 0.
\end{aligned}$$

We then expand to get:

$$\begin{aligned}
&-\frac{\partial}{\partial x}\int_0^h z\frac{\partial \varrho}{\partial z}U_1\mathrm{d}z - \frac{\partial}{\partial x}\int_0^h z\frac{\partial \varrho}{\partial z}\frac{\partial p}{\partial x}\mathrm{d}z\int_0^z \frac{z}{\varrho}\mathrm{d}z - \frac{\partial}{\partial x}\int_0^h z\frac{\partial \varrho}{\partial z}\left(\frac{U_2-U_1}{F_0}\right)\mathrm{d}z\int_0^z \frac{1}{\mu}\mathrm{d}z, \\
&+\frac{\partial}{\partial x}\int_0^h z\frac{\partial \varrho}{\partial z}\mathrm{d}z\int_0^z \frac{\partial p}{\partial x}\frac{F_1}{F_0}\frac{1}{\mu}\mathrm{d}z - \frac{\partial}{\partial x}\int_0^h \frac{z^2\varrho}{\mu}\frac{\partial p}{\partial x}\mathrm{d}z - \frac{\partial}{\partial x}\int_0^h \frac{z\varrho}{\mu}\frac{U_2-U_1}{F_0}\mathrm{d}z + \frac{\partial}{\partial x}\int_0^h \frac{z\varrho}{\mu}\frac{\partial p}{\partial x}\frac{F_1}{F_0}\mathrm{d}z = 0.
\end{aligned} \tag{2.4.17}$$

Grouping terms with $\frac{\partial p}{\partial x}$ and $\frac{U_2-U_1}{F_0}$ respectively in Eq. (2.4.17) we have:

$$\begin{aligned}
&-\frac{\partial}{\partial x}\int_0^h z\frac{\partial \varrho}{\partial z}\frac{\partial p}{\partial x}\mathrm{d}z\int_0^z \frac{z}{\varrho}\mathrm{d}z + \frac{\partial}{\partial x}\int_0^h z\frac{\partial \varrho}{\partial z}\mathrm{d}z\int_0^z \frac{\partial p}{\partial x}\frac{F_1}{F_0}\frac{1}{\mu}\mathrm{d}z - \frac{\partial}{\partial x}\int_0^h \frac{z^2\varrho}{\mu}\frac{\partial p}{\partial x}\mathrm{d}z + \frac{\partial}{\partial x}\int_0^h \frac{z\varrho}{\mu}\frac{\partial p}{\partial x}\frac{F_1}{F_0}\mathrm{d}z \\
&-\frac{\partial}{\partial x}\int_0^h z\frac{\partial \varrho}{\partial z}U_1\mathrm{d}z - \frac{\partial}{\partial x}\int_0^h z\frac{\partial \varrho}{\partial z}\left(\frac{U_2-U_1}{F_0}\right)\mathrm{d}z\int_0^z \frac{1}{\mu}\mathrm{d}z - \frac{\partial}{\partial x}\int_0^h \frac{z\varrho}{\mu}\frac{U_2-U_1}{F_0}\mathrm{d}z = 0.
\end{aligned}$$

We then apply a factorization:

$$\begin{aligned}
&-\frac{\partial}{\partial x}\left(\left[\int_0^h \frac{z\varrho}{\mu}\left(z - \frac{F_1}{F_0}\right)\mathrm{d}z + \int_0^h \left[z\frac{\partial \varrho}{\partial z}\left(\int_0^z \frac{z}{\mu}\mathrm{d}z - \frac{F_1}{F_0}\int_0^z \frac{\mathrm{d}z}{\mu}\right)\right]\mathrm{d}z\right]\frac{\partial p}{\partial x}\right) \\
&-\frac{\partial}{\partial x}\int_0^h z\frac{\partial \varrho}{\partial z}U_1\mathrm{d}z - \frac{\partial}{\partial x}\left[\left(\frac{U_2-U_1}{F_0}\right)\left(\int_0^h \left[z\frac{\partial \varrho}{\partial z}\int_0^z \frac{\mathrm{d}z}{\mu}\right]\mathrm{d}z + \int_0^h \frac{z\varrho}{\mu}\mathrm{d}z\right)\right] = 0.
\end{aligned} \tag{2.4.18}$$

Defining

$$\begin{aligned}
F_2 &= \int_0^h \frac{z\varrho}{\mu}\left(z - \frac{F_1}{F_0}\right)\mathrm{d}z, \\
F_3 &= \int_0^h \frac{z\varrho}{\mu}\mathrm{d}z,
\end{aligned}$$

$$
\begin{aligned}
G_1 &= \int_0^h \left[z\frac{\partial \varrho}{\partial z}\left(\int_0^z \frac{z}{\mu}\mathrm{d}z - \frac{F_1}{F_0}\int_0^z \frac{\mathrm{d}z}{\mu}\right)\right]\mathrm{d}z, \\
G_2 &= \int_0^h \left[z\frac{\partial \varrho}{\partial z}\int_0^z \frac{\mathrm{d}z}{\mu}\right]\mathrm{d}z, \\
G_3 &= \int_0^h z\frac{\partial \varrho}{\partial z}\mathrm{d}z,
\end{aligned}
$$

we have:

$$
-\frac{\partial}{\partial x}\left[(F_2 + G_1)\frac{\partial p}{\partial x}\right] - \frac{\partial}{\partial x}\left[\left(\frac{U_2 - U_1}{F_0}\right)(F_3 + G_2) + U_1 G_3\right] = 0. \tag{2.4.19}
$$

Similarly, we derive the expressions for $\frac{\partial v}{\partial z}$ and $\frac{\partial \varrho}{\partial z}$. Substituting them in term $-\frac{\partial}{\partial y}\int_0^h \left(zv\frac{\partial \varrho}{\partial z} + z\varrho\frac{\partial v}{\partial z}\right)\mathrm{d}z$ of Eq. (2.4.16) we yield:

$$
-\frac{\partial}{\partial y}\left[(F_2 + G_1)\frac{\partial p}{\partial y}\right] - \frac{\partial}{\partial y}\left[\left(\frac{V_2 - V_1}{F_0}\right)(F_3 + G_2) + V_1 G_3\right] = 0. \tag{2.4.20}
$$

Substituting Eq. (2.4.19) and Eq. (2.4.20) in Eq. (2.4.16) we have:

$$
\begin{aligned}
&\int_0^h \frac{\partial \varrho}{\partial t}\mathrm{d}z + h\left[\frac{\partial(\varrho U)_2}{\partial x} + \frac{\partial(\varrho V)_2}{\partial y}\right] - \frac{\partial}{\partial x}\left[(F_2 + G_1)\frac{\partial p}{\partial x}\right] - \frac{\partial}{\partial x}\left[\left(\frac{U_2 - U_1}{F_0}\right)(F_3 + G_2) + U_1 G_3\right] \\
&- \frac{\partial}{\partial y}\left[(F_2 + G_1)\frac{\partial p}{\partial y}\right] - \frac{\partial}{\partial y}\left[\left(\frac{V_2 - V_1}{F_0}\right)(F_3 + G_2) + V_1 G_3\right] + (\varrho W)_2 - (\varrho W)_1 = 0.
\end{aligned} \tag{2.4.21}
$$

Balancing both sides of Eq. (2.4.21) we found the GRE:

$$
\begin{aligned}
\frac{\partial}{\partial x}\left[(F_2 + G_1)\frac{\partial p}{\partial x}\right] + \frac{\partial}{\partial y}\left[(F_2 + G_1)\frac{\partial p}{\partial y}\right] =& h\left[\frac{\partial(\varrho U)_2}{\partial x} + \frac{\partial(\varrho V)_2}{\partial y}\right] - \frac{\partial}{\partial x}\left[\left(\frac{U_2 - U_1}{F_0}\right)(F_3 + G_2) + U_1 G_3\right] \\
&- \frac{\partial}{\partial y}\left[\left(\frac{V_2 - V_1}{F_0}\right)(F_3 + G_2) + V_1 G_3\right] \\
&+ \int_0^h \frac{\partial \varrho}{\partial t}\mathrm{d}z + (\varrho W)_2 - (\varrho W)_1 = 0,
\end{aligned} \tag{2.4.22}
$$

where

$$
F_0 = \int_0^h \frac{1}{\mu}\mathrm{d}z,
$$

$$
\begin{aligned}
F_1 &= \int_0^h \frac{z}{\mu} \mathrm{d}z, \\
F_2 &= \int_0^h \frac{z\varrho}{\mu} \left(z - \frac{F_1}{F_0} \right) \mathrm{d}z, \\
F_3 &= \int_0^h \frac{z\varrho}{\mu} \mathrm{d}z, \\
G_1 &= \int_0^h \left[z \frac{\partial \varrho}{\partial z} \left(\int_0^z \frac{z}{\mu} \mathrm{d}z - \frac{F_1}{F_0} \int_0^z \frac{\mathrm{d}z}{\mu} \right) \right] \mathrm{d}z, \\
G_2 &= \int_0^h \left[z \frac{\partial \varrho}{\partial z} \int_0^z \frac{\mathrm{d}z}{\mu} \right] \mathrm{d}z, \\
G_3 &= \int_0^h z \frac{\partial \varrho}{\partial z} \mathrm{d}z.
\end{aligned}
$$

2.5 Simplifications to the GRE for journal bearings

The following assumptions are used in the simplification. We consider in the left-hand side of Eq. (2.4.22) the components of the pressure-driven flow (Poiseuille flow) along both circumferential "y" and axial "x" directions. Similarly, we consider in the right-hand side of Eq. (2.4.22) the component of the drag-driven flow (Couette flow) which is only present along the circumferential direction. We also consider an incompressible fluid ($\varrho = const$) and a stationary bearing ($V_1 = 0$). In addition, there is no slip between the shaft and the fluid, so $U_2 = \omega R$. Under these assumptions the Eq. (2.4.22) reduces to:

$$
\frac{\partial}{\partial y} \left[F_2 \frac{\partial p}{\partial y} \right] + \frac{\partial}{\partial x} \left[F_2 \frac{\partial p}{\partial x} \right] = h\varrho \frac{\partial V_2}{\partial y} - \frac{\partial}{\partial y} \left[V_2 \frac{F_3}{F_0} \right] + \varrho (W_2 - W_1). \tag{2.5.1}
$$

Then, the fluid density vanishes and in consequence $F_3 = F_1$. Thus, the Eq. (2.5.1) becomes:

$$
\frac{\partial}{\partial y} \left[F_2 \frac{\partial p}{\partial y} \right] + \frac{\partial}{\partial x} \left[F_2 \frac{\partial p}{\partial x} \right] = \frac{\partial (hV_2)}{\partial y} - \frac{\partial}{\partial y} \left[V_2 \frac{F_1}{F_0} \right] - V_2 \frac{\partial h}{\partial y} + (W_2 - W_1). \tag{2.5.2}
$$

For journal bearings, generally $W_2 - W_1 = V_2 \frac{\partial h}{\partial y}$, see (Jang and Khonsari, 2004) for details. Then we obtain the simplified GRE for journal bearings:

$$
\frac{\partial}{\partial y} \left[F_2 \frac{\partial p}{\partial y} \right] + \frac{\partial}{\partial x} \left[F_2 \frac{\partial p}{\partial x} \right] = \frac{\partial}{\partial y} \left[V_2 \left(h - \frac{F_1}{F_0} \right) \right]. \tag{2.5.3}
$$

2.5.1 The non-dimensional GRE for journal bearings

To make Eq. (2.5.3) to suffice for a variety of different problems, we follow the non-dimensional variables defined in Eq. (2.1.12), Eq. (2.1.15) and Eq. (2.3.7). As in Sect. 2.3.1, we transform our domain into the dimensionless domain $\bar{\Omega} = [0, 2\pi]\times[0, 1]$ for the $(\theta, \bar{x})$ coordinates. Since we consider an isoviscous lubricant the non-dimensional viscosity integrals are defined as follows, see (Brito, 2009) for details.

$$\overline{F_0} = \int_0^1 \frac{1}{\bar{\mu}} \mathrm{d}\bar{z} = \frac{1}{\bar{\mu}}, \qquad \overline{F_1} = \int_0^1 \frac{\bar{z}}{\bar{\mu}} \mathrm{d}\bar{z} = \frac{1}{2\bar{\mu}}, \qquad \overline{F_2} = \int_0^1 \frac{\bar{z}}{\bar{\mu}} \left(\bar{z} - \frac{\overline{F_1}}{\overline{F_0}}\right) \mathrm{d}\bar{z} = \frac{2\overline{F_0} - 3\overline{F_1}}{6\bar{\mu}\overline{F_0}},$$

with

$$F_0 = \frac{\bar{h}C\overline{F_0}}{\mu_0}, \qquad F_1 = \frac{\bar{h}^2C^2\overline{F_1}}{\mu_0}, \qquad F_2 = \frac{\bar{h}^3C^3\overline{F_2}}{\mu_0}. \tag{2.5.4}$$

Then, by applying the chain rule, Eq. (2.5.3) is posed into the normalized reference domain:

$$\frac{\partial}{\partial\theta}\left[\frac{\bar{h}^3C^3\overline{F_2}}{\mu_0}\frac{\mu_0\omega R^2}{C^2}\frac{\partial\bar{p}}{\partial\theta}\frac{1}{R}\right]\frac{1}{R} + \frac{\partial}{\partial\bar{x}}\left[\frac{\bar{h}^3C^3\overline{F_2}}{\mu_0}\frac{\mu_0\omega R^2}{C^2}\frac{\partial\bar{p}}{\partial\bar{x}}\frac{1}{L}\right]\frac{1}{L} = \frac{\partial}{\partial\theta}\left[\omega R\left(\bar{h}C - \frac{\bar{h}^2C^2\overline{F_1}}{\frac{\mu_0\bar{h}C\overline{F_0}}{\mu_0}}\right)\right]\frac{1}{R}. \tag{2.5.5}$$

After simplifying we obtain the non-dimensional RE for journal bearings:

$$\frac{\partial}{\partial\theta}\left[\bar{h}^3\overline{F_2}\frac{\partial\bar{p}}{\partial\theta}\right] + \frac{R^2}{L^2}\frac{\partial}{\partial\bar{x}}\left[\bar{h}^3\overline{F_2}\frac{\partial\bar{p}}{\partial\bar{x}}\right] = \frac{\partial}{\partial\theta}\left[\bar{h}\left(1 - \frac{\overline{F_1}}{\overline{F_0}}\right)\right]. \tag{2.5.6}$$

We transform the domain into $\tilde{\Omega} = [0, 2\pi] \times [0, \frac{L}{R}]$ by introducing the new variable $\tilde{x} = \bar{x}\frac{L}{R}$. The Eq. (2.5.6) becomes:

$$\frac{\partial}{\partial\theta}\left[\tilde{h}^3\overline{F_2}\frac{\partial\bar{p}}{\partial\theta}\right] + \frac{\partial}{\partial\tilde{x}}\left[\tilde{h}^3\overline{F_2}\frac{\partial\bar{p}}{\partial\tilde{x}}\right] = \frac{\partial}{\partial\theta}\left[\tilde{h}\left(1 - \frac{\overline{F_1}}{\overline{F_0}}\right)\right]. \tag{2.5.7}$$

where:

$$\tilde{h} = 1 + \tilde{\lambda}\cos(\theta - \tilde{\gamma}), \tag{2.5.8}$$

with

$$\tilde{\lambda} = \frac{1}{C}\left[(\tilde{x}\tan\varphi + C\bar{\rho}\sin\alpha)^2 + (\tilde{x}\tan\beta + C\bar{\rho}\cos\alpha)^2\right]^{1/2} \tag{2.5.9}$$

and

$$\tilde{\gamma} = \arctan\frac{\tilde{x}\tan\varphi + C\bar{\rho}\sin\alpha}{\tilde{x}\tan\beta + C\bar{\rho}\cos\alpha}. \tag{2.5.10}$$

It is important to remark that, due to the domain transformation from $\bar{\Omega}$ to $\tilde{\Omega}$, the admissible range of the misalignment angle projections provided in Eq. (2.1.22) and Eq. (2.1.23) for prescribed values of $\bar{\rho}$ and α changes to:

$$-\frac{CR}{L}\left(1+\bar{\rho}\sin\alpha\right) < \tan\varphi < \frac{CR}{L}\left(1-\bar{\rho}\sin\alpha\right). \tag{2.5.11}$$

$$-\frac{R}{L}\left(\left[C^2-\left(\frac{L}{R}\tan\varphi+C\bar{\rho}\sin\alpha\right)^2\right]^{1/2}-C\bar{\rho}\cos\alpha\right) < \tan\beta < \frac{R}{L}\left(\left[C^2-\left(\frac{L}{R}\tan\varphi+C\bar{\rho}\sin\alpha\right)^2\right]^{1/2}-C\bar{\rho}\cos\alpha\right). \tag{2.5.12}$$

2.6 The Elrod–Adams cavitation model

An additional unknown is introduced to address the cavitation phenomenon in the Elrod–Adams model, the saturation ϑ that represents the lubricant concentration. As it was explained in Sect. 1.3, when cavitation occurs, the domain presents two regions. Thus, we split the domain $\tilde{\Omega}$ into two parts: the active zone Ω^+ where positive pressure values are present with the GRE governing the lubricant behaviour, and the Ω^0 where the pressure is zero and the conservation of mass equation needs to be changed. See the whole configuration of the normalized domain $\tilde{\Omega}$ including its boundary $\partial\tilde{\Omega}$ in Fig. 2.4, i.e.

$$\tilde{\Omega} = \Omega^+ \cup \Omega^0, \tag{2.6.1}$$

$$\partial\tilde{\Omega} = \Gamma_0 \cup \Gamma_1 \cup \Gamma_2. \tag{2.6.2}$$

The saturation ϑ takes the value 1 in the active zone Ω^+ and takes any other value in the range $[0,1]$ within the cavitated region Ω^0. Notice that Γ_0 is the zero width boundary where the lubricant is axially supplied through, with known concentration ($\vartheta = \vartheta_0$); Σ depicts the free boundary between the active zone and the cavitated one. The hydrodynamic problem is stated as follows. To find $(\bar{p}, \vartheta)$ such as the following conditions are verified:

$$\frac{\partial}{\partial\theta}\left[\tilde{h}^3\overline{F_2}\frac{\partial\bar{p}}{\partial\theta}\right]+\frac{\partial}{\partial\tilde{x}}\left[\tilde{h}^3\overline{F_2}\frac{\partial\bar{p}}{\partial\tilde{x}}\right]=\frac{\partial}{\partial\theta}\left[\tilde{h}\left(1-\frac{\overline{F_1}}{\overline{F_0}}\right)\right], \qquad \bar{p}>0 \text{ and } \vartheta=1 \text{ in } \Omega^+, \tag{2.6.3}$$

$$\frac{\partial}{\partial\theta}\left[\vartheta\tilde{h}\left(1-\frac{\overline{F_1}}{\overline{F_0}}\right)\right]=0, \qquad \bar{p}=0, \quad 0\le\vartheta\le 1 \text{ in } \Omega^0, \tag{2.6.4}$$

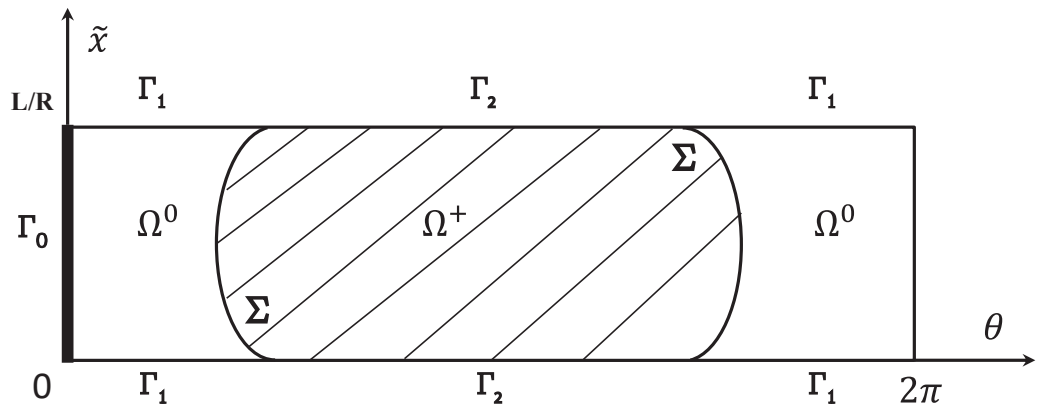

Figure 2.4. Configuration for the normalized hydrodynamic domain $\tilde{\Omega}$.

$$\tilde{h}^3\overline{F_2}\frac{\partial\bar{p}}{\partial\mathbf{n}} = (1-\vartheta)\tilde{h}\left(1-\frac{\overline{F_1}}{\overline{F_0}}\right)\cos(\mathbf{n},\mathbf{i}), \qquad \bar{p}=0 \text{ in } \Sigma, \tag{2.6.5}$$

$$\vartheta = \vartheta_0 \text{ in } \Gamma_0, \tag{2.6.6}$$

$$\bar{p} = \bar{p}_s \text{ in } \Gamma_0, \tag{2.6.7}$$

$$\bar{p} = 0 \text{ in } \partial\tilde{\Omega} - \Gamma_0, \tag{2.6.8}$$

$$\bar{p}_s = \text{normalized supply pressure}, \tag{2.6.9}$$

where $\mathbf{n}$ is the normal vector to Σ and $\mathbf{i}$ is the unitary vector in the θ direction. The Eq. (2.6.3) states that the pressure, in the active zone is governed by the GRE. The Eq. (2.6.4) states that in the cavitated zone, the mass conservation law must be satisfied in the θ direction. The Eq. (2.6.5) is the flow continuity condition through the free boundary between the active and the cavitated zone. Eqs. (2.6.6-2.6.9) correspond to the boundary conditions related to the concentration and pressure at the supply groove, and the pressure at the front and back boundaries of the device respectively.

2.6.1 Deduction of the flow continuity condition through the free boundary

The amount of flux in a fluid element is the difference between the amount of incoming and outcoming fluxes. Mathematically it is:

$$\int_{\tilde{\Omega}} \nabla\cdot(\tilde{h}^3\overline{F_2}\nabla\bar{p})\mathrm{d}\tilde{\Omega} = \int_{\partial\tilde{\Omega}} \tilde{h}^3\overline{F_2}\frac{\partial\bar{p}}{\partial\mathbf{n}}\mathrm{d}s. \tag{2.6.10}$$

It is important to remark that the flux has two components: the pressure-driven flow (Poiseuille flow) along both circumferential "y" and axial "x" directions and the drag-driven flow (Couette flow) which is only present along the circumferential direction. The flux in Ω^+ is:

$$\tilde{h}^3\overline{F_2}\nabla\bar{p} - \tilde{h}\left(1 - \frac{\overline{F_1}}{\overline{F_0}}\right)\mathbf{i}, \tag{2.6.11}$$

where $\mathbf{i}$ is the standard basis vector $\mathbf{i} = (1, 0)$, pointing to the θ direction in this case. At the boundary of Ω^+ the flux comprises the normal and the tangential components. Since a mass interchange occurs along the normal direction, we have:

$$\tilde{h}^3\overline{F_2}\frac{\partial\bar{p}}{\partial\mathbf{n}} - \tilde{h}\left(1 - \frac{\overline{F_1}}{\overline{F_0}}\right)\mathbf{i}\cdot\mathbf{n}. \tag{2.6.12}$$

In the same way, the amount of outcoming mass from Ω^0 through the boundary Σ is:

$$\vartheta\tilde{h}\left(1 - \frac{\overline{F_1}}{\overline{F_0}}\right)\mathbf{i}\cdot\mathbf{n}. \tag{2.6.13}$$

Then, there must be a balance, so:

$$\tilde{h}^3\overline{F_2}\frac{\partial\bar{p}}{\partial\mathbf{n}} = \tilde{h}\left(1 - \frac{\overline{F_1}}{\overline{F_0}}\right)\mathbf{i}\cdot\mathbf{n} - \vartheta\tilde{h}\left(1 - \frac{\overline{F_1}}{\overline{F_0}}\right)\mathbf{i}\cdot\mathbf{n}, \tag{2.6.14}$$

i.e.

$$\tilde{h}^3\overline{F_2}\frac{\partial\bar{p}}{\partial\mathbf{n}} = (1 - \vartheta)\tilde{h}\left(1 - \frac{\overline{F_1}}{\overline{F_0}}\right)\cos(\mathbf{i}, \mathbf{n}). \tag{2.6.15}$$

□

2.7 Weak formulation of the Elrod–Adams cavitation model

The starting point of this derivation is the strong form of the Elrod-Adams model provided by Eqs. (2.6.3-2.6.7). We first multiply by $\bar{\phi}$ such as $\bar{\phi}_{|\Gamma_1\cup\Gamma_2} = 0$,

$$\bar{\phi}\nabla\cdot(\tilde{h}^3\overline{F_2}\nabla\bar{p}) = \bar{\phi}\nabla\cdot\left[\tilde{h}\left(1-\frac{\overline{F_1}}{\overline{F_0}}\right),0\right] \qquad \bar{p}>0, \quad \vartheta = 1 \text{ in } \Omega^+. \tag{2.7.1}$$

The boundary of Ω^+ denoted by $\partial\Omega^+$ is split into two parts Γ_2 and Σ, i.e.

$$\partial\Omega^+ = \Gamma_2 \cup \Sigma. \tag{2.7.2}$$

So, we apply Green's formula on the left-hand side and we have:

$$\int_{\Gamma_2}\tilde{h}^3\overline{F_2}\frac{\partial\bar{p}}{\partial\mathbf{n}}\,\bar{\phi}\,\mathrm{d}\Gamma_2 + \int_{\Sigma}\tilde{h}^3\overline{F_2}\frac{\partial\bar{p}}{\partial\mathbf{n}}\,\bar{\phi}\,\mathrm{d}\Sigma - \int_{\Omega^+}(\tilde{h}^3\overline{F_2}\nabla\bar{p})\,\nabla\bar{\phi}\mathrm{d}\Omega^+ = \int_{\Omega^+}\nabla\cdot\left[\tilde{h}\left(1-\frac{\overline{F_1}}{\overline{F_0}}\right),0\right]\bar{\phi}. \tag{2.7.3}$$

Similarly, we apply Green's formula on the right-hand side of Eq. (2.7.3) to have:

$$\begin{aligned}\int_{\Gamma_2}\tilde{h}^3\overline{F_2}\frac{\partial\bar{p}}{\partial\mathbf{n}}\,\bar{\phi}\,\mathrm{d}\Gamma_2 + \int_{\Sigma}\tilde{h}^3\overline{F_2}\frac{\partial\bar{p}}{\partial\mathbf{n}}\,\bar{\phi}\,\mathrm{d}\Sigma - \int_{\Omega^+}(\tilde{h}^3\overline{F_2}\nabla\bar{p})\,\nabla\bar{\phi}\mathrm{d}\Omega^+ &= \int_{\Gamma_2}\left[\tilde{h}\left(1-\frac{\overline{F_1}}{\overline{F_0}}\right),0\right]\mathbf{n}\,\bar{\phi}\,\mathrm{d}\Gamma_2 \\ &+ \int_{\Sigma}\left[\tilde{h}\left(1-\frac{\overline{F_1}}{\overline{F_0}}\right),0\right]\mathbf{n}\,\bar{\phi}\,\mathrm{d}\Sigma - \int_{\Omega^+}\left[\tilde{h}\left(1-\frac{\overline{F_1}}{\overline{F_0}}\right),0\right]\nabla\bar{\phi}\mathrm{d}\Omega^+.\end{aligned} \tag{2.7.4}$$

Since the function $\bar{\phi}$ is chosen such as $\bar{\phi}_{|\Gamma_2} = 0$ we have:

$$\int_{\Sigma}\tilde{h}^3\overline{F_2}\frac{\partial\bar{p}}{\partial\mathbf{n}}\,\bar{\phi}\,\mathrm{d}\Sigma - \int_{\Omega^+}(\tilde{h}^3\overline{F_2}\nabla\bar{p})\,\nabla\bar{\phi}\mathrm{d}\Omega^+ = \int_{\Sigma}\left[\tilde{h}\left(1-\frac{\overline{F_1}}{\overline{F_0}}\right),0\right]\mathbf{n}\,\bar{\phi}\,\mathrm{d}\Sigma - \int_{\Omega^+}\left[\tilde{h}\left(1-\frac{\overline{F_1}}{\overline{F_0}}\right),0\right]\nabla\bar{\phi}\mathrm{d}\Omega^+. \tag{2.7.5}$$

We now multiply by the function $\bar{\phi}$ the Eq. (2.6.4). Since $\partial\Omega^0 = \Gamma_0\cup\Gamma_1\cup\Sigma$ and $\vartheta = \vartheta_0$ in Γ_0 we have after applying Green's formula:

$$\begin{aligned}\int_{\Gamma_0}\vartheta_0\left[\tilde{h}\left(1-\frac{\overline{F_1}}{\overline{F_0}}\right),0\right]\mathbf{n}\,\bar{\phi}\,\mathrm{d}\Gamma_0 + \int_{\Gamma_1}\vartheta_0\left[\tilde{h}\left(1-\frac{\overline{F_1}}{\overline{F_0}}\right),0\right]\mathbf{n}\,\bar{\phi}\,\mathrm{d}\Gamma_1 \\ + \int_{\Sigma}\vartheta_0\left[\tilde{h}\left(1-\frac{\overline{F_1}}{\overline{F_0}}\right),0\right]\mathbf{n}\,\bar{\phi}\,\mathrm{d}\Sigma - \int_{\Omega^0}\vartheta\left[\tilde{h}\left(1-\frac{\overline{F_1}}{\overline{F_0}}\right),0\right]\nabla\bar{\phi}\mathrm{d}\Omega^0 = 0.\end{aligned} \tag{2.7.6}$$

Since the function $\bar{\phi}$ is chosen such as $\bar{\phi}_{|\Gamma_1} = 0$ we have:

$$\int_{\Gamma_0} \vartheta_0 \left[\tilde{h}\left(1 - \frac{\overline{F_1}}{\overline{F_0}}\right), 0\right] \mathbf{n}\, \bar{\phi}\, \mathrm{d}\Gamma_0 + \int_{\Sigma} \vartheta_0 \left[\tilde{h}\left(1 - \frac{\overline{F_1}}{\overline{F_0}}\right), 0\right] \mathbf{n}\, \bar{\phi}\, \mathrm{d}\Sigma - \int_{\Omega^0} \vartheta \left[\tilde{h}\left(1 - \frac{\overline{F_1}}{\overline{F_0}}\right), 0\right] \nabla\bar{\phi} \mathrm{d}\Omega^0 = 0, \tag{2.7.7}$$

i.e.

$$\int_{\Gamma_0} \vartheta_0 \tilde{h}\left(1 - \frac{\overline{F_1}}{\overline{F_0}}\right) \cos(\mathbf{n}, \mathbf{i})\, \bar{\phi}\, \mathrm{d}\Gamma_0 + \int_{\Sigma} \vartheta \tilde{h}\left(1 - \frac{\overline{F_1}}{\overline{F_0}}\right) \cos(\mathbf{n}, \mathbf{i})\, \bar{\phi}\, \mathrm{d}\Sigma - \int_{\Omega^0} \vartheta \tilde{h}\left(1 - \frac{\overline{F_1}}{\overline{F_0}}\right) \frac{\partial\bar{\phi}}{\partial\theta} \mathrm{d}\Omega^0 = 0. \tag{2.7.8}$$

We then substitute Eq. (2.6.5) in Eq. (2.7.5) and obtain:

$$\begin{aligned}\int_{\Sigma} (1 - \vartheta)\tilde{h}\left(1 - \frac{\overline{F_1}}{\overline{F_0}}\right) \cos(\mathbf{n}, \mathbf{i})\, \bar{\phi}\, \mathrm{d}\Sigma - \int_{\Omega^+} (\tilde{h}^3 \overline{F_2} \nabla\bar{p})\, \nabla\bar{\phi} \mathrm{d}\Omega^+ = \int_{\Sigma} \tilde{h}\left(1 - \frac{\overline{F_1}}{\overline{F_0}}\right) \cos(\mathbf{n}, \mathbf{i})\, \bar{\phi}\, \mathrm{d}\Sigma \\ - \int_{\Omega^+} \tilde{h}\left(1 - \frac{\overline{F_1}}{\overline{F_0}}\right) \frac{\partial\bar{\phi}}{\partial\theta} \mathrm{d}\Omega^+.\end{aligned} \tag{2.7.9}$$

Reducing like terms we have:

$$- \int_{\Sigma} \vartheta \tilde{h}\left(1 - \frac{\overline{F_1}}{\overline{F_0}}\right) \cos(\mathbf{n}, \mathbf{i})\, \bar{\phi}\, \mathrm{d}\Sigma - \int_{\Omega^+} (\tilde{h}^3 \overline{F_2} \nabla\bar{p})\, \nabla\bar{\phi} \mathrm{d}\Omega^+ = - \int_{\Omega^+} \tilde{h}\left(1 - \frac{\overline{F_1}}{\overline{F_0}}\right) \frac{\partial\bar{\phi}}{\partial\theta} \mathrm{d}\Omega^+. \tag{2.7.10}$$

Then, adding up Eq. (2.7.8) and Eq. (2.7.10) and reducing like terms we obtain:

$$\begin{aligned}- \int_{\Omega^+} (\tilde{h}^3 \overline{F_2} \nabla\bar{p})\, \nabla\bar{\phi} \mathrm{d}\Omega^+ = - \int_{\Omega^+} \tilde{h}\left(1 - \frac{\overline{F_1}}{\overline{F_0}}\right) \frac{\partial\bar{\phi}}{\partial\theta} \mathrm{d}\Omega^+ + \int_{\Omega^0} \vartheta \tilde{h}\left(1 - \frac{\overline{F_1}}{\overline{F_0}}\right) \frac{\partial\bar{\phi}}{\partial\theta} \mathrm{d}\Omega^0 \\ - \int_{\Gamma_0} \vartheta_0 \tilde{h}\left(1 - \frac{\overline{F_1}}{\overline{F_0}}\right) \cos(\mathbf{n}, \mathbf{i})\, \bar{\phi}\, \mathrm{d}\Gamma_0.\end{aligned} \tag{2.7.11}$$

Taking into account that $\tilde{\Omega} = \Omega^+ \cup \Omega^0$, $\vartheta = 1$ in Ω^+ and $\bar{p} = 0$ in Ω^0 we have:

$$- \int_{\tilde{\Omega}} (\tilde{h}^3 \overline{F_2} \nabla\bar{p})\, \nabla\bar{\phi} \mathrm{d}\tilde{\Omega} = - \int_{\tilde{\Omega}} \vartheta \tilde{h}\left(1 - \frac{\overline{F_1}}{\overline{F_0}}\right) \frac{\partial\bar{\phi}}{\partial\theta} \mathrm{d}\tilde{\Omega} - \int_{\Gamma_0} \vartheta_0 \tilde{h}\left(1 - \frac{\overline{F_1}}{\overline{F_0}}\right) \cos(\mathbf{n}, \mathbf{i})\, \bar{\phi}\, \mathrm{d}\Gamma_0, \tag{2.7.12}$$

$$\vartheta \in H(\bar{p}) = \begin{cases} 1, & \text{if } \bar{p} > 0, \\ [0,1], & \text{if } \bar{p} = 0, \\ 0, & \text{if } \bar{p} < 0, \end{cases} \tag{2.7.13}$$

where the space of test functions is given by:

$$\mathcal{K} = \left\{ \bar{\phi} \in H^1(\tilde{\Omega}) : \bar{\phi}_{|\partial\tilde{\Omega}-\Gamma_0} = 0 \right\}. \tag{2.7.14}$$

By using integration by parts we rewrite Eq. (2.7.12) as follows:

$$-\int_{\tilde{\Omega}} (\tilde{h}^3 \overline{F_2} \nabla \bar{p}) \nabla \bar{\phi} \mathrm{d}\tilde{\Omega} = \int_{\tilde{\Omega}} \frac{\partial}{\partial \theta} \left(\vartheta \tilde{h} \left(1 - \frac{\overline{F_1}}{\overline{F_0}} \right) \right) \bar{\phi} \, \mathrm{d}\tilde{\Omega}, \quad \forall \bar{\phi} \in \mathcal{K}, \quad \vartheta = \vartheta_0 \quad \text{in} \quad \Gamma_0. \tag{2.7.15}$$

2.8 Shaft stationary model

The shaft stationary model is based on the balance of force and torque components involved in the device. For that, the hydrodynamic RE is coupled to Newton's second law. It is well-known that the pressure p is a physical magnitude that measures the force projection in a perpendicular direction to the surface per unit area. Then, the resultant dimensional fluid film force components, acting on the bearing and accordingly to Fig. 2.2 are:

$$\int_{\Omega} p(\theta, x) \sin\theta \mathrm{d}\theta \mathrm{d}x = F_{\mathrm{y}},$$
$$\int_{\Omega} p(\theta, x) \cos\theta \mathrm{d}\theta \mathrm{d}x = F_{\mathrm{z}},$$

where $\sin\theta$ and $\cos\theta$ stand for the unitary normal vector components to the bearing surface.

Moreover, to determine the resultant torque generated by the fluid force on the shaft, we start finding the torque in an arbitrary position vector $\mathbf{q}$ located on the bearing surface with coordinates $\mathbf{q} = (x, R_b \sin\theta, R_b \cos\theta)$ with R_b the bearing radius. The coordinate system corresponds to the one in Fig. 2.2. Let p be, the pressure

at the position vector $\mathbf{q}$. The force $\mathbf{F}_{\mathrm{q}}$ exerted by the fluid pressure at that point will be:

$$\mathbf{F}_{\mathrm{q}} = (0, p\sin\theta, p\cos\theta),$$

Mathematically the torque $\boldsymbol{\tau}$ is defined as a cross product of two vectors, which produces rotation:

$$\boldsymbol{\tau} = \mathbf{r} \times \mathbf{F}_{\mathrm{q}},$$

where $\mathbf{r}$ represents the displacement vector from the rotation axis to the point where $\mathbf{F}_{\mathrm{q}}$ is applied. Thus, the torque generated at the position vector $\mathbf{q}$ is:

$$\begin{aligned}
\boldsymbol{\tau} &= \mathbf{q} \times \mathbf{F}_{\mathrm{q}}, \\
&= (x, R_b\sin\theta, R_b\cos\theta) \times (0, p\sin\theta, p\cos\theta), \\
&= (0, -xp\cos\theta, xp\sin\theta).
\end{aligned}$$

Then, the resultant dimensional torque components acting on the bearing are:

$$\begin{aligned}
-\int_{\Omega} xp(\theta, x)\cos\theta \mathrm{d}\theta\mathrm{d}x &= \tau_{\mathrm{y}}, \\
\int_{\Omega} xp(\theta, x)\sin\theta \mathrm{d}\theta\mathrm{d}x &= \tau_{\mathrm{z}}.
\end{aligned}$$

Notice that the equilibrium of the external torque $\boldsymbol{\tau}$ and the one exerted by the fluid film is taken also with respect to the origin O. Accordingly to Eq. (2.3.7), we obtain the following dimensionless expressions for the equilibrium of force components:

$$\begin{aligned}
\frac{1}{|\mathbf{F}|}\int_{\bar{\Omega}} \frac{\mu_0\omega L R^3}{C^2}\bar{p}\sin\theta \mathrm{d}\theta\mathrm{d}\bar{x} = \bar{F}_{\mathrm{y}}, \\
\frac{1}{|\mathbf{F}|}\int_{\bar{\Omega}} \frac{\mu_0\omega L R^3}{C^2}\bar{p}\cos\theta \mathrm{d}\theta\mathrm{d}\bar{x} = \bar{F}_{\mathrm{z}},
\end{aligned}$$

where $|\mathbf{F}|$ denotes the modulus of the external load $\mathbf{F}$, used for scaling. The right-hand side terms $\bar{F}_{\mathrm{y}}$ and $\bar{F}_{\mathrm{z}}$

stand for the normalized components of $\mathbf{F}$. Similarly, the dimensionless expressions for the torque are:

$$-\frac{1}{|\boldsymbol{\tau}|}\int_{\bar{\Omega}}\frac{\mu_0\omega L^2R^3}{C^2}\bar{x}\bar{p}\cos\theta\mathrm{d}\theta\mathrm{d}\bar{x}=\bar{\tau}_{\mathrm{y}},$$
$$\frac{1}{|\boldsymbol{\tau}|}\int_{\bar{\Omega}}\frac{\mu_0\omega L^2R^3}{C^2}\bar{x}\bar{p}\sin\theta\mathrm{d}\theta\mathrm{d}\bar{x}=\bar{\tau}_{\mathrm{z}},$$

where $|\boldsymbol{\tau}|$ denotes the modulus of the external torque $\boldsymbol{\tau}$, used for scaling. The right-hand side terms $\bar{\tau}_{\mathrm{y}}$ and $\bar{\tau}_{\mathrm{z}}$ stand for the normalized components of $\boldsymbol{\tau}$.

CHAPTER 3

Prediction of contact with the Reynolds cavitation model

In this chapter we consider a finite element discretization and accomplish the minimization stage by a PCG, modified with both projection and restarting strategies to account for cavitation. We also explain the resolution of the inverse problem by an interior, trust-region algorithm subject to bounds. Numerical experiments and discussion are also included.

3.1 Finite load capacity for the point contact case

It is important to remark that the limit case of a shaft-bearing contact presents two particular situations: a line contact and a point contact. The line-contact case has been studied before in (Ciuperca, Jai, and Tello, 2009), where the authors show the infinite load capacity of the system and the unboundedness of the pressure. For the point contact case, it is possible to analytically obtain a finite load capacity of the system. We prove in Theorem 3.1.1 that the force exerted by the pressure is indeed finite. A similar proof on sliders can be found in (Ciuperca, Hafidi, and Jai, 2006).

Theorem 3.1.1. *Let* $\bar{h}(\bar{x},\alpha,\theta,\beta) = 1 + \frac{\bar{x}}{C}\tan\beta\cos(\theta-\alpha)$ *be the fluid film thickness for* $\bar{x} \in [0,1]$*, such that* $\min\{\bar{h}\} = 0$ *with a contact point at* $\bar{x} = 1$ *if* $\tan\beta = C$*,* $\bar{\rho} = 0$ *and* $\theta - \alpha = \pi$*. Then, we have that:* $\lim_{\tan\beta\to C}\int_{\bar{\Omega}}\bar{\phi}\mathrm{d}\bar{x}\mathrm{d}\theta < k(\beta,C,\bar{\rho},\alpha)$.

Proof. We first prove that the term

$$\int_{\bar{\Omega}} \bar{h}^3 |\nabla \bar{\phi}|^2 \mathrm{d}\bar{x}\mathrm{d}\theta \tag{3.1.1}$$

is uniformly bounded. The proof is obtained from the inequality

$$\begin{aligned}\int_{\bar{\Omega}} \bar{h}^3 |\nabla \bar{\phi}|^2 \mathrm{d}\bar{x}\mathrm{d}\theta = \Lambda \int_{\bar{\Omega}} \bar{h} \frac{\partial \bar{\phi}}{\partial \theta} \mathrm{d}\bar{x}\mathrm{d}\theta, \\ \leq \frac{1}{2} \int_{\bar{\Omega}} \bar{h}^3 |\nabla \bar{\phi}|^2 \mathrm{d}\bar{x}\mathrm{d}\theta + \frac{\Lambda^2}{2} \int_{\bar{\Omega}} \bar{h}^{-1} \mathrm{d}\bar{x}\mathrm{d}\theta,\end{aligned}$$

providing

$$\int_{\bar{\Omega}} \bar{h}^{-1} \mathrm{d}\bar{x}\mathrm{d}\theta \leq k < \infty,$$

and in consequence the boundedness of Eq. (3.1.1). Since

$$\begin{aligned}\int_{\alpha+\frac{5\pi}{6}}^{\alpha+\frac{7\pi}{6}} \int_0^1 \bar{h}^{-1} \mathrm{d}\bar{x}\mathrm{d}\theta \leq \int_{\alpha+\frac{5\pi}{6}}^{\alpha+\frac{7\pi}{6}} C\left[\frac{\ln(C+\tan\beta\cos(\theta-\alpha))}{\tan\beta\cos(\theta-\alpha)} - \frac{\ln(C)}{\tan\beta\cos(\theta-\alpha)}\right]\mathrm{d}\theta, \\ \leq \frac{C}{\tan\beta}\left[\int_{\alpha+\frac{5\pi}{6}}^{\alpha+\frac{7\pi}{6}} \frac{\ln(C+\tan\beta\cos(\theta-\alpha))}{\cos(\theta-\alpha)}\mathrm{d}\theta - k_0\right] < \infty,\end{aligned}$$

we have that

$$\lim_{\tan\beta\to C} \int_{\bar{\Omega}} \bar{h}^3 |\nabla \bar{\phi}|^2 \mathrm{d}\bar{x}\mathrm{d}\theta \leq k < \infty,$$

and therefore

$$\int_{\bar{\Omega}} \bar{h}^3 |\nabla \bar{\phi}|^2 \mathrm{d}\bar{x}\mathrm{d}\theta \leq k < \infty, \qquad \forall \beta < \arctan C. \tag{3.1.2}$$

Let $\Omega_1 = \left\{(\bar{x},\theta) \in (0,1)\times(\alpha-\frac{5\pi}{6}, \alpha+\frac{5\pi}{6})\right\}$, i.e. a region where no over-pressures nor contacts occur. Thanks to (3.1.2) we have

$$\int_{\Omega_1} \bar{h}^3 |\nabla \bar{\phi}|^2 \mathrm{d}\bar{x}\mathrm{d}\theta \leq k < \infty.$$

So,

$$\int_{\Omega_1} |\nabla \bar{\phi}|^2 \mathrm{d}\bar{x}\mathrm{d}\theta \leq \frac{k}{\min\limits_{(\bar{x},\theta)\in\Omega_1} \bar{h}^3}, \qquad \forall \beta < \arctan C,$$

and in consequence, $\bar{\phi} \in L^p(\Omega_1),\ \forall p < \infty$, in particular

$$\int_{\Omega_1} |\bar{\phi}| \mathrm{d}\bar{x}\mathrm{d}\theta \leq k. \tag{3.1.3}$$

To compute the L^1-norm of $\bar{\phi}$ in $\bar{\Omega}$ we consider

$$\begin{aligned}
\left| \int_{\bar{\Omega}} \bar{\phi} \cos(\theta - \alpha) \mathrm{d}\bar{x}\mathrm{d}\theta \right| &= \left| \int_{\bar{\Omega}} \bar{\phi} \frac{\partial}{\partial \bar{x}} \bar{x} \cos(\theta - \alpha) \mathrm{d}\bar{x}\mathrm{d}\theta \right|, \\
&= \left| k_0 \int_{\bar{\Omega}} \bar{\phi} \frac{\partial \bar{h}}{\partial \bar{x}} \mathrm{d}\bar{x}\mathrm{d}\theta \right|, \\
&= \left| k_0 \int_{\bar{\Omega}} \bar{h} \frac{\partial \bar{\phi}}{\partial \bar{x}} \mathrm{d}\bar{x}\mathrm{d}\theta \right|, \\
&\leq \left| k_0 \left(\frac{1}{2} \int_{\bar{\Omega}} \bar{h}^3 |\nabla \bar{\phi}|^2 \mathrm{d}\bar{x}\mathrm{d}\theta + \frac{\Lambda^2}{2} \int_{\bar{\Omega}} \bar{h}^{-1} \mathrm{d}\bar{x}\mathrm{d}\theta \right) \right|.
\end{aligned}$$

Since $\lim_{\tan\beta \to C} \int_{\bar{\Omega}} \bar{\phi} \cos(\theta - \alpha) \mathrm{d}\bar{x}\mathrm{d}\theta < \infty$, in view of (3.1.3), we have that

$$\lim_{\tan\beta \to C} \int_{\alpha + \frac{5\pi}{6}}^{\alpha + \frac{7\pi}{6}} \int_0^1 \bar{\phi} \mathrm{d}\bar{x}\mathrm{d}\theta < \infty. \tag{3.1.4}$$

Then, thanks to (3.1.3) and (3.1.4) we obtain

$$\lim_{\tan\beta \to C} \int_{\bar{\Omega}} \bar{\phi} \mathrm{d}\bar{x}\mathrm{d}\theta < \infty. \tag{3.1.5}$$

□

Nevertheless, Boedo and Booker (2004) suggest that misaligned bearings have infinite load and moment capacity as the end-plane minimum film thickness approaches zero under transient journal squeeze motion and under steady load and speed conditions. Those results differ markedly from this proof and from finite capacity trends reported in previous numerical and experimental studies.

Corollary 1. *As a consequence of the previous theorem we have that*

$$\int_{\bar{\Omega}} \bar{\phi} \sin(\theta - \alpha) \mathrm{d}\bar{x}\mathrm{d}\theta, \quad \int_{\bar{\Omega}} \bar{\phi} \cos(\theta - \alpha) \mathrm{d}\bar{x}\mathrm{d}\theta,$$

$$\int_{\bar{\Omega}} \bar{x}\bar{\phi}\sin(\theta-\alpha)\mathrm{d}\bar{x}\mathrm{d}\theta, \qquad \int_{\bar{\Omega}} \bar{x}\bar{\phi}\cos(\theta-\alpha)\mathrm{d}\bar{x}\mathrm{d}\theta,$$

are uniformly bounded at the contact point limit and therefore for $|\mathbf{F}|$ *or* $|\boldsymbol{\tau}|$ *large enough we do not have a solution for the problem.*

Nevertheless, the inequality (3.1.5) does not guarantee the uniform boundedness of the pressure. See in Fig. 3.13 the pressure behaviour as $\tan\beta \to C$.

Remark 3.1.1. *The study in (Boedo and Booker, 2004), for the stationary case, is accomplished for*

$$h = C - e^x\cos\theta - e^y\sin\theta - z\phi^y\cos\theta + z\phi^x\sin\theta, \tag{3.1.6}$$

where e^x, e^y *are components of mid-plane journal eccentricity, and* ϕ^x, ϕ^y *are components of journal axial misalignment angle. It is possible to reproduce the proof of Theorem 3.1.1 using Eq. (3.1.6) by assuming* $e^x = e^y = \phi^y = 0$ *and substituting* ϕ^x *by* $\tan\phi^x$.

3.2 Direct problem resolution

We first consider the direct problem, where the position of the inner cylinder is known, i.e. h is a given datum determined by α, ρ, φ and β. Taking advantage of the region under study we perform the spatial approximation by piecewise quadrangular Lagrange Q_1 finite elements; see (Zienkiewicz and R. L. Taylor, 2000) for details. Let n be the total number of nodes for the mesh discretization. Then, $\bar{\phi}$ is approximated as follows:

$$\bar{\phi} \approx \bar{\phi}_{\mathrm{f}} = \sum_{j=1}^{n} N_j\phi_j,$$

where N_j stands for the shape function evaluated at node j and parameter ϕ_j stands for the discrete pressure value also evaluated at node j. Subscript f stands for the finite element approximation.

The mesh topology used in this work is shown in Fig. 3.1. As in (Boedo and Booker, 2004), we use a uniform mesh density along the circumferential direction, whereas in the axial direction the mesh density becomes finer when moving from the bearing mid-plane to the bearing ends. An attenuation factor δ is used for this purpose. When considering misalignment, this mesh topology provides better results towards the

contact. In addition, the singularity appears to the bearing ends when $\delta = 0$ and for that reason a finer mesh at these places is particularly convenient. In the axial direction, given L and the division number m, the

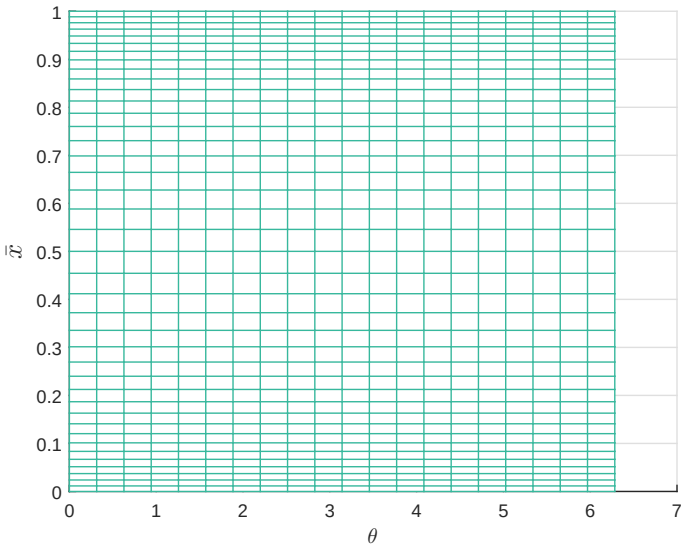

Figure 3.1. The mesh topology used in this work (dimensionless).

coordinates $\bar{x}_i$ are generated from a bearing end to its mid-plane, by Eq. (3.2.1):

$$\begin{aligned} \bar{x}_{i+1} &= \bar{x}_i + \frac{\Delta}{\delta^i}, \\ \bar{x}_0 &= 0, \end{aligned} \tag{3.2.1}$$

where

$$\Delta = \frac{L}{2} \Big/ \sum_{j=0}^{\frac{m}{2}-1} \delta^{j-\frac{m}{2}+1}.$$

The generated mesh, as in (ibid.), is then reflected about the bearing mid-plane, ($\bar{x} = 1/2$) in this work. On the other hand, the discretized form of the dimensionless functional in Eq. (2.3.8) is:

$$\begin{aligned} J(\bar{\phi}_{\mathrm{f}}) = \frac{1}{2} \sum_{j=1}^{n} \sum_{k=1}^{n} \int_{\bar{\Omega}} LR\bar{h}^3 \left[\nabla(N_j\phi_j)\right]^T \nabla(N_k\phi_k) \mathrm{d}\theta \mathrm{d}\bar{x} \\ - \sum_{j=1}^{n} \int_{\bar{\Omega}} 6\bar{\mu}\bar{h}\overline{W} \frac{\mu_0 \omega L R^2}{C^2} \frac{\partial(N_j\phi_j)}{\partial\theta} \mathrm{d}\theta \mathrm{d}\bar{x}, \end{aligned}$$

i.e.

$$J(\bar{\phi}_{\mathrm{f}}) = \frac{1}{2}\sum_{j=1}^{n}\sum_{k=1}^{n}\phi_j\Big(\int_{\bar{\Omega}} LR\bar{h}^3(\nabla N_j)^T(\nabla N_k)\mathrm{d}\theta\mathrm{d}\bar{x}\Big)\phi_k - \sum_{j=1}^{n}\phi_j\int_{\bar{\Omega}} 6\bar{\mu}\bar{h}\overline{W},\frac{\mu_0\omega LR^2}{C^2}\frac{\partial N_j}{\partial\theta}\mathrm{d}\theta\mathrm{d}\bar{x}. \tag{3.2.2}$$

It can be easily verified this functional is in the form of $\frac{1}{2}\phi^T A\phi - \phi^T b$.

Therefore, for the resolution of the direct problem we propose a PCG, with some variations to account for cavitation. Starting at any $\phi_1 \in \mathbb{R}^n$ the basic approach of conjugate gradient methods is to generate a sequence of iterates ϕ_j according to:

$$\phi_{j+1} = \phi_j + \varepsilon_j d_j, \qquad \varepsilon_j = \frac{< r_j, r_j >}{< d_j, Ad_j >}, \tag{3.2.3}$$

where d_j stands for the search direction, ε_j is the step length that minimizes the functional along d_j from the point ϕ_j, and $r_j = b - A\phi_j$ stands for the residual. Notation $<,>$ stands for the inner product of both n-dimensional vectors. Subsequent computations of terms r_j and d_j obey the following equations that guarantee vectors $\{d_j\}$ to be A-orthogonal (Luenberger and Ye, 2008):

$$r_{j+1} = r_j - \varepsilon_j Ad_j, \tag{3.2.4}$$

$$d_{j+1} = r_{j+1} + \xi_j d_j, \tag{3.2.5}$$

$$\xi_j^{FR} = \frac{< r_{j+1}, r_{j+1} >}{< r_j, r_j >}, \tag{3.2.6}$$

where term ξ_j^{FR} stands for the deflection parameter that characterizes a concrete conjugate gradient implementation, the Fletcher-Reeves approach in our case; see (Bazaraa, Sherali, and Shetty, 2006) for details. Although for quadratic functions all approaches coincide, we select the Fletcher-Reeves' taking advantage of the inner product $< r_j, r_j >$, which is known from the previous iteration. We define $d_1 = r_1 = b - A\phi_1$ for the initial iteration.

Moreover, it has been demonstrated that the performance of the conjugate gradient method can be really enhanced by accomplishing a restart, following a proper criterion. Suppose that we decide to reset at some

iteration j, having found ϕ_{j+1} following Eq. (3.2.3). Let $\varsigma = j$ be this restart iteration. For the next one, we find the search direction as usual:

$$d_{\varsigma+1} = r_{\varsigma+1} + \xi_\varsigma d_\varsigma.$$

Then, we store the direction $d_{\varsigma+1}$ at some variable, say d_1, we set $j = 1$ and the algorithm returns to the first step to execute the next loop of iterations. However, instead of always employing Eq. (3.2.5) we use:

$$d_2 = r_2 + \xi_1 d_1, \text{ for } j = 1,$$

but

$$d_{j+1} = r_{j+1} + \xi_j d_j + \zeta_j d_1 \quad \text{for } j \geq 2, \tag{3.2.7}$$

where

$$\zeta_j = \frac{< -r_{j+1}, Ad_1 >}{< d_1, Ad_1 >},$$

and ξ_j is computed as usually, following Eq. (3.2.6). This schema ensures d_1 and d_2 to be A-orthogonal when the function is quadratic. Nevertheless, if the function is quadratic with a positive definite Hessian A, and d_1 is chosen arbitrarily, when $j = 2$ the usual choice of ξ_2 would guarantee d_3 and d_2 to be A-orthogonal but a correction parameter will be needed to make d_3 and d_1 A-orthogonal. This is ensured by the third term $\zeta_j d_1$ in Eq. (3.2.7). The procedure was suggested by Beale in 1970, with the motivation that whenever a restart is done using $d_1 = r_1$ instead of $d_1 = d_{\varsigma+1}$ we lose important second order information inherent in d_ς. More on this can be viewed in (ibid.). Furthermore, the conjugate gradient method is usually extended to include preconditioning as follows:

$$\phi_{j+1} = \phi_j + \varepsilon_j d_j, \qquad \varepsilon_j = \frac{< r_j, s_j >}{< d_j, Ad_j >},$$

$$r_{j+1} = r_j - \varepsilon_j A d_j, \qquad s_{j+1} = M^{-1} r_{j+1},$$

$$d_{j+1} = s_{j+1} + \xi_j d_j, \qquad \xi_j^{FR} = \frac{< r_{j+1}, s_{j+1} >}{< r_j, s_j >},$$

$$M = \Psi \Psi^T,$$

where $r_1 = b - A\phi_1$ and $d_1 = s_1 = M^{-1}r_1$ for the initial iteration. Unfortunately, we cannot perform the minimization of the functional in Eq. (3.2.2) by using straightforwardly the PCG depicted above. With that regular approach, it is possible to get a solution out of the convex set defined in Eq. (2.3.3), for configurations that provoke cavitation. Those solutions would mean negative pressure values that have no physical meaning. So, we need to specify that the pressure is never negative in order to get physically correct results. Thus, we modified the PCG with a projection technique to account for cavitation, and performing a restarting process whenever a projection occurs. This approach corrects at each iteration j the pressure value components ϕ^i_j and takes up the necessary zero gradients automatically, whenever the first one is detected out of the convex set. We use the projection technique $\max(\phi^i_j, 0)$, also proposed in (Calvo, Durany, and Vázquez, 1997).

We determined the following expressions to properly compute the new descent directions after a restarting procedure when considering preconditioning. These expressions, that guarantee the search directions $\{d_j\}$ to be A-orthogonal, are in fact our contribution to ensure that the modified PCG holds its convergence properties. In what follows, the terms applied to the restarting process for the PCG will all be marked by˜ as in (Knabner and Angermann, 2003), except ξ_j and ζ_j. Thus, for the direction $\tilde{d}_{j+1}$ with $j \geq 2$ we have:

$$\tilde{d}_{j+1} = \tilde{r}_{j+1} + \xi_j \tilde{d}_j + \zeta_j \tilde{d}_1.$$

Due to back transformation

$$\phi = \Psi^{-T}\tilde{\phi},$$

the algorithm has the search direction

$$d_j = \Psi^{-T}\tilde{d}_j,$$

for the transformed iterate

$$\phi_j = \Psi^{-T}\tilde{\phi}_j. \tag{3.2.8}$$

The residual r_j in ϕ_j is given by:

$$r_j = b - A\phi_j = \Psi(c - B\tilde{\phi}_j) = \Psi\tilde{r}_j,$$

where $B = \Psi^{-1}A\Psi^{-T}$ and $c = \Psi^{-1}b$ are the system matrix and the right-hand side term respectively after

applying a split preconditioning process. Then:

$$\begin{aligned}
\tilde{d}_{j+1} &= \Psi^{-1} r_{j+1} + \xi_j \tilde{d}_j + \zeta_j \tilde{d}_1, \\
\Psi^{-T} \tilde{d}_{j+1} &= \Psi^{-T} \Psi^{-1} r_{j+1} + \xi_j \Psi^{-T} \tilde{d}_j + \zeta_j \Psi^{-T} \tilde{d}_1, \\
d_{j+1} &= \Psi^{-T} \Psi^{-1} r_{j+1} + \xi_j d_j + \zeta_j d_1, \\
d_{j+1} &= M^{-1} r_{j+1} + \xi_j d_j + \zeta_j d_1,
\end{aligned}$$

with

$$\begin{aligned}
\zeta_j &= \frac{< -\tilde{r}_{j+1}, B\tilde{d}_1 >}{< \tilde{d}_1, B\tilde{d}_1 >}, \\
&= \frac{< -\Psi^{-1} r_{j+1}, \Psi^{-1} A \Psi^{-T} \Psi^T d_1 >}{< \Psi^T d_1, \Psi^{-1} A \Psi^{-T} \Psi^T d_1 >}, \\
&= \frac{< -\Psi^{-1} r_{j+1}, \Psi^{-1} A d_1 >}{< \Psi^T d_1, \Psi^{-1} A d_1 >}.
\end{aligned}$$

Taking the inner product:

$$\begin{aligned}
\zeta_j &= \frac{(-\Psi^{-1} r_{j+1})^T \Psi^{-1} A d_1}{(\Psi^T d_1)^T \Psi^{-1} A d_1}, \\
&= \frac{-r_{j+1}^T \Psi^{-T} \Psi^{-1} A d_1}{d_1^T \Psi \Psi^{-1} A d_1}, \\
&= \frac{-r_{j+1}^T M^{-1} A d_1}{d_1^T A d_1}.
\end{aligned}$$

If we denote $\sigma_1 = A d_1$ we have:

$$\zeta_j = \frac{-r_{j+1}^T M^{-1} \sigma_1}{d_1^T \sigma_1}.$$

Notice that we need additionally to solve the system of equation $M s_\sigma = \sigma_1$, but only when a restarting procedure occurs. The solution is carried out by easily solving two triangular systems with coefficient matrices Ψ and Ψ^T. Finally, we have:

$$\zeta_j = \frac{< -r_{j+1}, s_\sigma >}{< d_1, \sigma_1 >}.$$

A flow chart for the proposed PCG algorithm considering cavitation with the restarting technique in-

cluded is presented in Fig. 3.2. As a summary, in the regular iteration when there is no cavitation nor

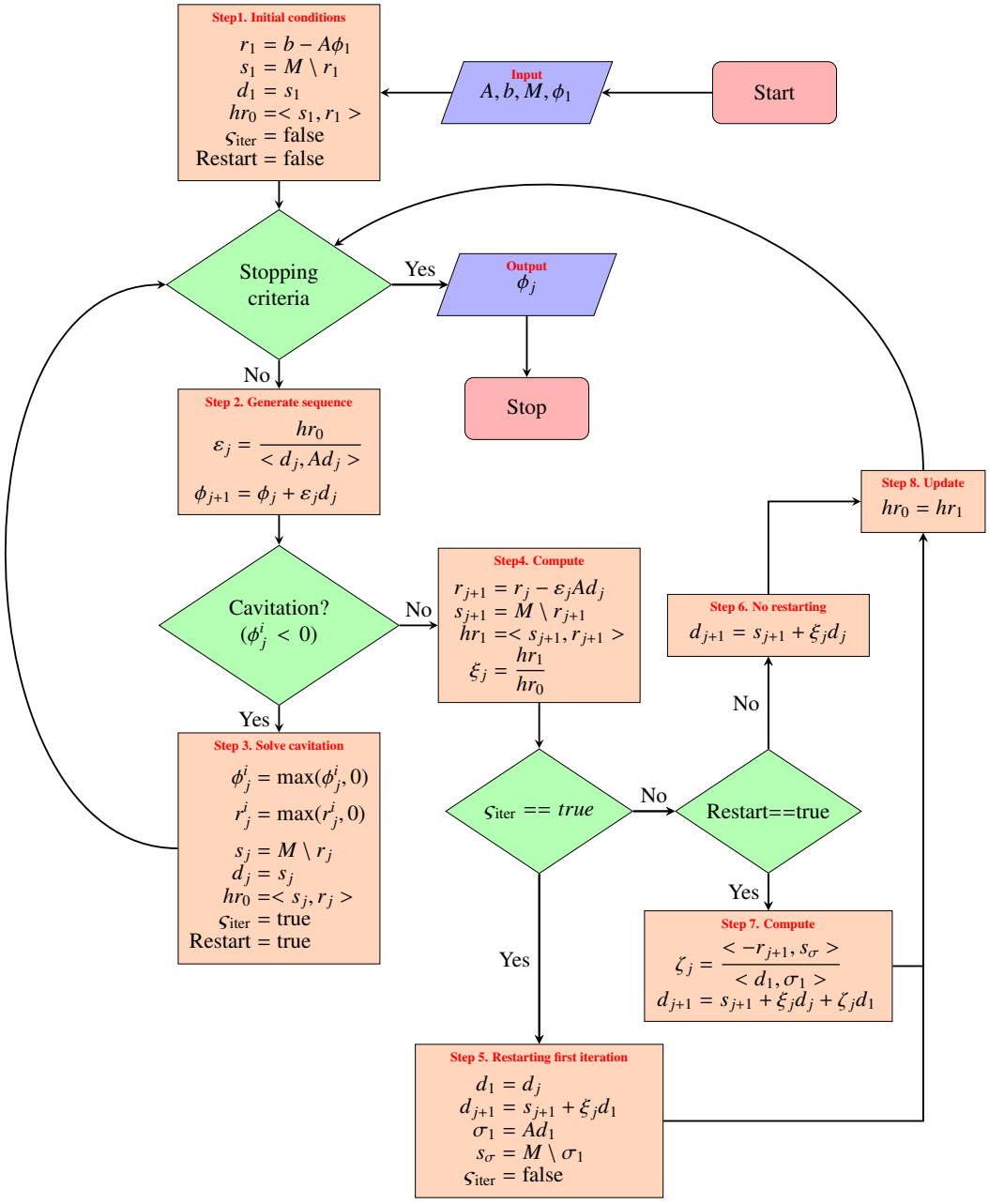

Figure 3.2. Flow chart for the PCG considering cavitation and the restarting technique.

restarting (steps 2, 4, 6, 8), we have the following expressions:

$$\phi_{j+1} = \phi_j + \varepsilon_j d_j, \qquad \varepsilon_j = \frac{< r_j, s_j >}{< d_j, Ad_j >},$$

$$r_{j+1} = r_j - \varepsilon_j A d_j, \qquad s_{j+1} = M^{-1} r_{j+1}, \tag{3.2.9}$$
$$d_{j+1} = s_{j+1} + \xi_j d_j, \qquad \xi_j^{FR} = \frac{< r_{j+1}, s_{j+1} >}{< r_j, s_j >}.$$

Whenever we detect cavitation ($\phi_j^i < 0$), we set the negative pressure and residual components to zero. We solve s_j in Eq. (3.2.9), but using the updated residual value r_j. We prepare the restarting procedure by setting $d_j = s_j$, computing the product $< s_j, r_j >$ and defining two flags (step 3). Then, in the first iteration of the restarting (when ς_{iter} == true) we set and compute (step 5):

$$\begin{aligned} d_1 &= d_j, && \text{same value as } s_j, \\ d_{j+1} &= s_{j+1} + \xi_j d_1, && \text{for j = 1}, \\ s_\sigma &= M \setminus \sigma_1, && \text{computed just once per restarting}, \\ \sigma_1 &= A d_1. \end{aligned}$$

Subsequent iterations (when Restart == true) consider the search direction computed as follows (step 7):

$$d_{j+1} = s_{j+1} + \xi_j d_j + \zeta_j d_1, \qquad \text{for } j \geq 2,$$
$$\zeta_j = \frac{< -r_{j+1}, s_\sigma >}{< d_1, \sigma_1 >}.$$

This way we performed the minimization stage of our functional getting the pressure values at each discretization node. Since we deal with a quadratic functional and our proposal guarantees the search directions $\{d_j\}$ to be A-orthogonal, by Theorem 8.8.3 in (Bazaraa, Sherali, and Shetty, 2006, p. 405), the Conjugate Gradient Method (CG) produces an optimal solution after one complete application of the main step, that is, after at most n line searches[1] have been performed. Due to the deduction of the PCG, see (Knabner and Angermann, 2003) for instance, and the identity

$$\|\phi_j - \phi\|_A = \|\tilde{\phi}_j - \tilde{\phi}\|_B, \tag{3.2.10}$$

which results from Eq. (3.2.8), the approximation properties for the CG also hold for the PCG method

[1] using exact arithmetic

if the condition number $\kappa(A)$ is replaced by $\kappa(B) = \kappa(M^{-1}A)$. Notice that, since $\Psi^{-T}B\Psi^{T} = M^{-1}A$ and $\Psi B\Psi^{-1} = AM^{-1}$, B, $M^{-1}A$ and AM^{-1} have the same eigenvalues, and hence the same condition number κ. Therefore, the error $(\phi_j - \phi)$ at the j^{th} step in the energy norm $\|.\|_A$ is:

$$\|\phi_j - \phi\|_A \leq 2\left(\frac{\kappa^{1/2}-1}{\kappa^{1/2}+1}\right)^{j} \|\phi_0 - \phi\|_A, \tag{3.2.11}$$

with $\kappa = \kappa(M^{-1}A)$. The algorithm stops when either the maximum iteration number is reached or $\|r\| \leq tol\|b\|$, with tol the chosen tolerance.

3.3 Inverse problem resolution

For solving the dimensionless inverse problem we first consider the balance of force and torque components involved. Thus, the hydrodynamic RE is coupled to Newton's second law (see Sect. 2.8). According to the domain $\bar{\Omega}$ we define the residual E as follows:

$$E(x_k) = \begin{bmatrix} \bar{F}_{\text{y}} & - & \frac{1}{|\mathbf{F}|}\int_{\bar{\Omega}} \frac{\mu_0\omega L R^3}{C^2}\bar{\phi}_k \sin\theta \mathrm{d}\theta\mathrm{d}\bar{x} \\ \bar{F}_{\text{z}} & - & \frac{1}{|\mathbf{F}|}\int_{\bar{\Omega}} \frac{\mu_0\omega L R^3}{C^2}\bar{\phi}_k \cos\theta \mathrm{d}\theta\mathrm{d}\bar{x} \\ \bar{\tau}_{\text{y}} & + & \frac{1}{|\boldsymbol{\tau}|}\int_{\bar{\Omega}} \frac{\mu_0\omega L^2 R^3}{C^2}\bar{x}\bar{\phi}_k \cos\theta \mathrm{d}\theta\mathrm{d}\bar{x} \\ \bar{\tau}_{\text{z}} & - & \frac{1}{|\boldsymbol{\tau}|}\int_{\bar{\Omega}} \frac{\mu_0\omega L^2 R^3}{C^2}\bar{x}\bar{\phi}_k \sin\theta \mathrm{d}\theta\mathrm{d}\bar{x} \end{bmatrix} : \mathbb{R}^4 \mapsto \mathbb{R}. \tag{3.3.1}$$

where $\bar{\phi}_k$ is the k$^{\text{th}}$ solution to the hydrodynamic problem in Eq. (2.3.8), whose coefficient depends on $x_k = \{\bar{\rho}_k, \alpha_k, \varphi_k, \beta_k\}$, such that $E(x_0) \geq E(x_1) \geq \cdots \geq E(x_n)$ for n solutions with the following constraints:

$$\bar{\rho}_k \in [0, 1), \tag{3.3.2}$$

$$\alpha_k \in [0, 2\pi], \tag{3.3.3}$$

$$\varphi_k \in \left[\arctan\left(-C(1+\bar{\rho}_k\sin\alpha_k)\right), \arctan\left(C(1-\bar{\rho}_k\sin\alpha_k)\right)\right], \tag{3.3.4}$$

$$\beta_k \in \left[\arctan\left(-\left[C^2 - (\tan\varphi_k + C\bar{\rho}_k\sin\alpha_k)^2\right]^{1/2} - C\bar{\rho}_k\cos\alpha_k\right), \arctan\left(\left[C^2 - (\tan\varphi_k + C\bar{\rho}_k\sin\alpha_k)^2\right]^{1/2} - C\bar{\rho}_k\cos\alpha_k\right)\right]. \tag{3.3.5}$$

Thus, the numerical approach is to minimize in least squares sense the L^2-norm of the residual E, defined in Eq. (3.3.1), i.e.

$$\min_{x_k \in \mathbb{R}^4} \|E(x_k)\|_2^2, \tag{3.3.6}$$

subject to the constraints defined in Eqs. (3.3.2-3.3.5). To obtain the dimensionless pressure minimizer $\bar{\phi}^*$, four unknown parameters are needed $(\bar{\rho}^*, \alpha^*, \varphi^*, \beta^*)$, which determine the shaft position and misalignment of the system. Starting from an initial guess vector $x_0 = \{\bar{\rho}_0, \alpha_0, \varphi_0, \beta_0\}$, we use an iterative method, in the set of admissible positions of the parameters, that generates a sequence of ever improving solutions x_1, x_2,..., x_n that minimize $\|E\|_2^2$. At the minimum, where the equilibrium between the imposed and hydrodynamic loads is attained, we are predicting the final position of the shaft and the final pressure distribution.

For the optimization routine we propose a trust-region algorithmic strategy (Nocedal and Wright, 2006). Following the idea behind a trust-region method, the information gathered about E is used to construct an approximation m_k, usually defined to be a quadratic function of the form:

$$m_k(x_k + s_k) = E(x_k) + s_k^T \nabla E(x_k) + \frac{1}{2} s_k^T \nabla^2 E(x_k) s_k,$$

whose behaviour in a neighbourhood (the trust region) of the current point x_k is similar to that of the function E. Usually, the trust-region is a ball defined by $\|s_k\|_2 \leq \Delta_k$, where the scalar $\Delta_k > 0$ is called the trust-region radius (ibid.). To solve the problem we find the step $s_k = x_{k+1} - x_k$ by approximately solving the following subproblem:

$$\min_{s_k \in \mathbb{R}^4} m_k(x_k + s_k), \quad \text{where} \quad x_k + s_k \quad \text{lies inside the trust region.} \tag{3.3.7}$$

If the candidate solution does not decrease enough the value of E, we shrink the trust-region and resolve Eq. (3.3.7). Let He and G be defined by:

$$He(x_k) := \nabla^2 E(x_k), \qquad G(x_k) := \nabla E(x_k).$$

We proceed as in (Coleman and Li, 1996) to deal with the constraints. Let l and u be the lower and upper bounds of x_k. A solution $x_k \in \mathbb{R}^4$ is a feasible solution if and only if x_k^i, which represents the value of x_k in

the coordinate $i \in \{1, 2, 3, 4\}$, satisfies its corresponding constraint. Let l_i and u_i be the lower and upper limit values respectively of the i coordinate. The following holds: $l_1 \leq x_k^1 < u_1$, $l_2 \leq x_k^2 \leq u_2$ and $l_i < x_k^i < u_i$, for $i \in \{3, 4\}$. We define a vector function $r(x_k) : \mathbb{R}^n \to \mathbb{R}^n$ as follows:

Definition 3.3.1. *The vector $r(x_k) \in \mathbb{R}^n$ is defined:*

(i) if $G(x_k^i) < 0$ and $u_i < \infty$, then $r_i = (x_k^i) - u_i$,

(ii) if $G(x_k^i) \geq 0$ and $l_i > -\infty$, then $r_i = (x_k^i) - l_i$.

For any $a \in \mathbb{R}^n$, $diag(a)$ denotes an n-by-n diagonal matrix with the vector a defining the diagonal entries in their natural order. So, we define:

$$D(x_k) = diag(|r(x_k)|^{-1/2}).$$

In this manner and because we are facing a determined non-linear system of equations and a bounded admissible set of parameters, we propose the following scaled trust-region subproblem as in (Coleman and Li, 1996):

$$\min_{s_k \in \mathbb{R}^4} m_k(s) = s_k^T G(x_k) + \frac{1}{2} s_k^T M(x_k) s_k, \tag{3.3.8}$$

where

$$\begin{aligned} J^r(x_k) &= diag(sgn(G(x_k))), \\ C(x_k) &= D(x_k) diag(G(x_k)) J^r(x_k) D(x_k), \\ M(x_k) &= B(x_k) + C(x_k), \end{aligned}$$

where $B(x_k)$ is the discretization of $H\!e$. As the notation indicates, m_k and E are in agreement to first order at the current iterate x_k. The matrix $M(x_k)$ and the diagonal matrix $D(x_k)$ are chosen this way such that there is no need to handle constraints explicitly. Since the quadratic model m_k in Eq. (3.3.8) is defined to include the constraint information, a natural extension to the classical definition of the ratio η_k also takes place, see (Nocedal and Wright, 2006), and it is given by:

$$\eta_k = \frac{E(x_k + s_k) - E(x_k) + \frac{1}{2} s_k^T C(x_k) s_k}{m_k(s_k)}.$$

See (Coleman and Li, 1996) for a wide explanation on this selection. With this approach, it is possible to obtain an approximate trust-region solution which can guarantee second-order convergence by simply solving an unconstrained trust-region subproblem. A detailed study on the convergence of this method is found in (ibid., p. 11). Each iteration involves the approximate solution of the system using the classical PCG. When the squared 2-norm of E is small enough in correspondence with the tolerance chosen the algorithm finishes. An implementation of the routine used for the inverse problem can be found in MATLAB (e.g. `lsqnonlin`).

It is important to remark that the numerical approach returns the equilibrium position, which could be in contact with the bearing geometry or outside the region of admissible positions. If any of them occurs, verified with Eq. (2.1.22) and Eq. (2.1.23), we say the solution is the contact. We have considered three cases in which the algorithm for the inverse problem stops:

1. The equilibrium position is found within the region of admissible positions (no contact).
2. The equilibrium position is found, in contact with the bearing geometry.
3. There is a contact but the equilibrium position is not found. Before it occurs, the modified PCG, running inside the trust-region algorithm, warns the system matrix is not longer positive definite for the current iteration of the forward problem. In addition, it shows the candidate solution of the inverse problem places the shaft too far from the geometry boundary and, therefore, the mathematical model is not valid. After several attempts, trying to find a solution for the inverse problem in a smaller trust region, the algorithm throws an exception. We catch and handle the exception and say that surfaces are in contact.

3.4 Numerical results and discussion

We consider the Reynolds cavitation model for a journal bearing system when the position of the inner cylinder is unknown and allowed to be misaligned. The unknowns of the problem are the pressure of the lubricant and the shaft position, which is obtained when the equilibrium of force and torque components is attained. The forces acting on the system are the force exerted by the lubricant pressure and the exterior force applied to the system. We also consider their corresponding torques. To deal with the problem we first

consider the direct problem, which is solved numerically by minimizing a convex functional. For this, we use a PCG modified with both projection and restarting strategies to account for cavitation. The numerical approach to solve the inverse problem is based on an interior, trust-region algorithm subject to bounds, through which we transform the constrained optimization problem into an unconstrained one.

By solving this problem we provide engineers, under the assumptions made in this thesis, with an approach to predict cavitation and contact for a journal bearing allowed to be misaligned with an imposed radial loading. It is well-known that manufacturing defects in assembly may introduce problems during running, specifically misalignment. The destructive effects of this running problem have justified the development of numerical models for predicting the bearing operating characteristics under steady-state conditions (Pierre, France, et al., 2004). The algorithm provided, would help engineers in preventing damages to these devices that usually bring together serious economic implications. Cavitation, for instance, is well-known for provoking, along with the metal-to-metal contact, adhesive wear, erosive wear, and abrasive wear. They are all serious damages to a machine. Normally, technical problems on those devices entail stopping a productive machine, a disassembly process to substitute parts, with the corresponding waste of time and economic resources. In addition, we provide to engineers the Eq. (2.1.22) and Eq. (2.1.23) which can be useful for the assembly process since they define the admissible range of the misalignment angle projections φ and β to ensure no contact for prescribed values of $\bar{\rho}$ and α.

In this section, we also present numerical tests to verify the different numerical approaches involved. The dimensionless domain $\bar{\Omega} = [0, 2\pi] \times [0, 1]$ is discretized using a 400×160 finite elements mesh (64000 four-noded quadrangles) and an attenuation factor $\delta = 0.93$. Unless other values are specified, the geometrical and physical constants, taken from an experimental analysis accomplished in (Bouyer and Fillon, 2002), and numerical constants used during the experiments are those in Table 3.1.

Although the problem is solved in a dimensionless domain, most of the results are back transformed and presented in their real scales and units when it does not affect the visualization purpose. From now on, the terms front and rear ends of the bearing will be used in place of the left and right end-planes respectively.

In Fig. 3.3 we show the equilibrium position and the resulting pressure map wrapped around the bearing, when applying an external force of 3000 N in the "z" direction and a torque of 70 N m in the "y" direction.

This is equivalent to applying the force at 23.3 mm from the origin. That force is represented by the

Table 3.1. Geometrical, physical and numerical constants.

Parameter	Symbol	Value
Shaft angular velocity	ω [rpm]	1500
Journal bearing length	L [mm]	80
Radial clearance	C [μm]	117.5
Shaft radius	R [mm]	49.89
Fluid viscosity	μ [Pa s]	0.023
Reference viscosity	μ_0 [Pa s]	0.0813
Atmospheric pressure	p_a [MPa]	0.101325
Initial pressure	p_0 [MPa]	1
Initial $\bar{\rho}$	$\bar{\rho}_0$ [dimensionless]	0.5
Initial α	α_0 [rad]	$\frac{\pi}{6}$
Initial φ	φ_0 [rad]	1.745e-5
Initial β	β_0 [rad]	1.745e-5

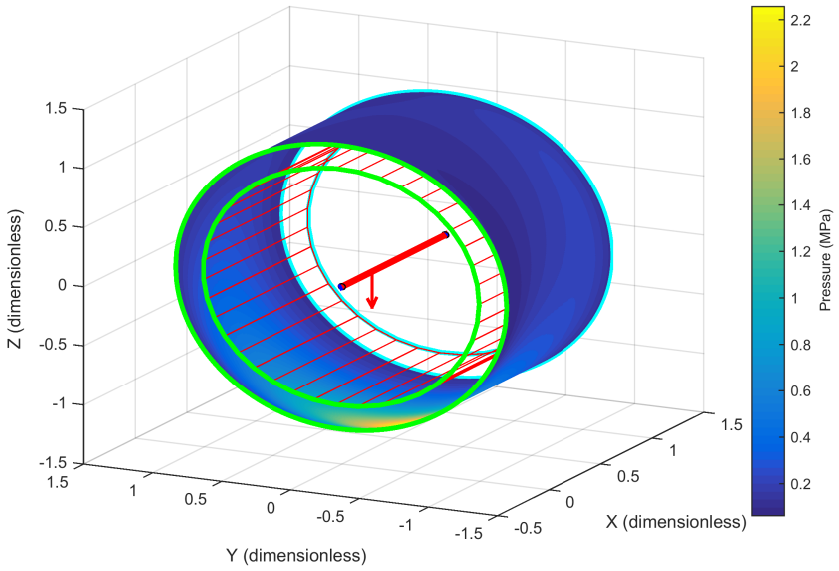

Figure 3.3. Solution to the inverse problem for $\mathbf{F} = (0, 0, 3000\ \text{N})$ and $\boldsymbol{\tau} = (0, 70\ \text{N m}, 0)$. The equilibrium position is found at $\bar{\rho} = 108.57$ μm, $\alpha = 3.775367$ rad, $\varphi = -0.000075$ rad and $\beta = -0.000140$ rad.

vertical arrow in this figure. As expected, the peak pressure map is located accordingly to the force position and shaft displacement, and tends to move towards the bearing front in this case, representing the reality. The equilibrium position is found at $\bar{\rho} = 108.57$ μm, $\alpha = 3.775367$ rad, $\varphi = -0.000075$ rad and $\beta = -0.000140$ rad. Notice that the colour bar presents real pressure values and the corresponding unit, but a normalized journal bearing has been used in favour of visualization. With this solution, attained with our numerical approach, we verify our hypothesis on how to predict the final position of the shaft and the final

pressure distribution in a misaligned journal bearing with the Reynolds cavitation model.

A contour map for the pressure is presented in Fig. 3.4 and also a perspective view in Fig. 3.5. Both

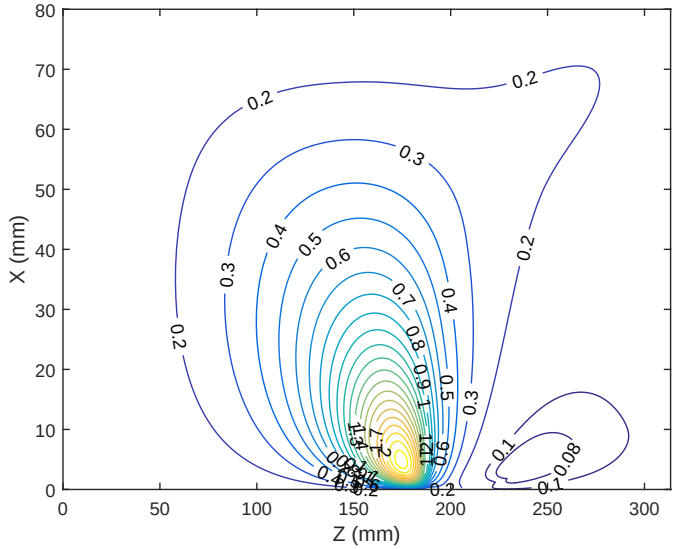

Figure 3.4. Contour map for the pressure obtained when solving the inverse problem for $\mathbf{F} = (0, 0, 3000\ \text{N})$ and $\boldsymbol{\tau} = (0, 70\ \text{N m}, 0)$.

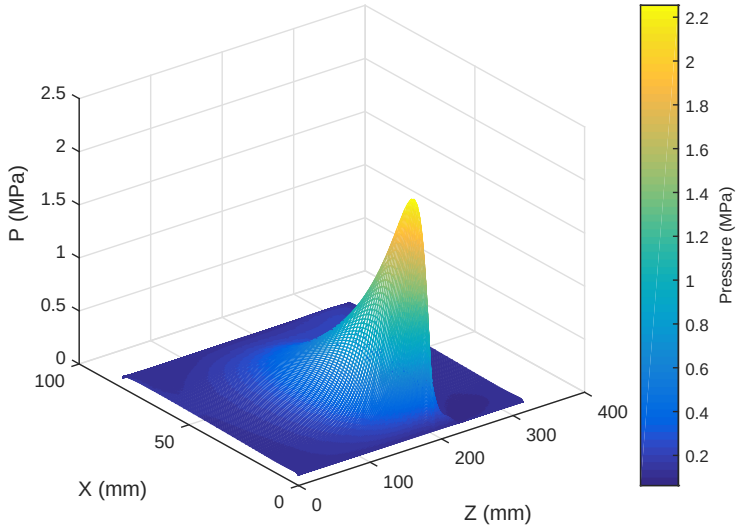

Figure 3.5. Perspective view for the pressure obtained when solving the inverse problem for $\mathbf{F} = (0, 0, 3000\ \text{N})$ and $\boldsymbol{\tau} = (0, 70\ \text{N m}, 0)$.

verify the peak pressure behaviour. The latter also shows the cavitated region when the pressure takes the

zero value, most on the divergent zone. In Fig. 3.6 we show the behaviour of the fluid film thickness h at the equilibrium position of the inverse problem for $\mathbf{F} = (0, 0, 3000\ \text{N})$ and $\boldsymbol{\tau} = (0, 70\ \text{N m}, 0)$. The minimum value is 8.93 μm, represented in the figure by a circular marker. It is located at $x = 0$ mm, $\theta = 3.7699$ rad ($\theta R = 188.0808$ mm). Figures 3.7a and 3.7b present the misalignment of the axes on the

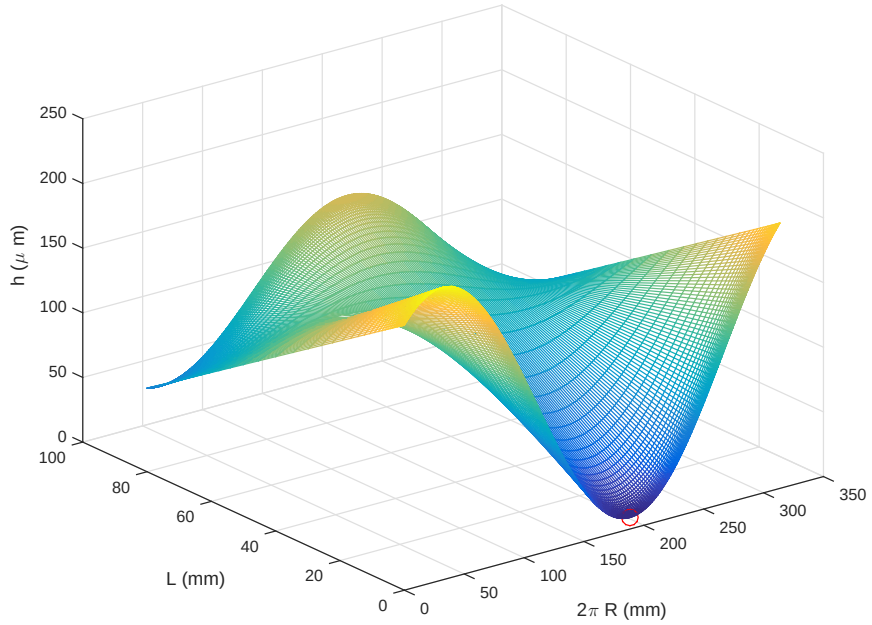

Figure 3.6. The fluid film thickness behaviour at the equilibrium position of the inverse problem for $\mathbf{F} = (0, 0, 3000\ \text{N})$ and $\boldsymbol{\tau} = (0, 70\ \text{N m}, 0)$. The minimum value is 8.93 μm, represented in the figure by a circular marker. It is located at $x = 0$ mm, $\theta = 3.7699$ rad ($\theta R = 188.0808$ mm).

xz-plane and xy-plane respectively. Accordingly to the force applying position, the centre at the front end, as expected, approaches more towards the contact in both figures. In Fig. 3.8 we present the behaviour of the minimum film thickness function $hMin$ related to the force applying position, in both front and rear ends of the device. This case has been conducted using different forces of 1000 N, 2000 N and 3000 N for an angular velocity of 1500 rpm. The force position, as a way of generating different torques, has been applied every 2 mm from the bearing mid-plane to its rear end (21 points in total).

In Fig. 3.8a the behaviour at the rear end is presented. Notice that, when the position of the application of the force increases, the minimum film thickness monotonically decreases, reaching even some contact point detected by the algorithm and shown as a black square marker. This result proves numerically, that the device is unable to generate a force that can balance a large imposed load under that operating conditions.

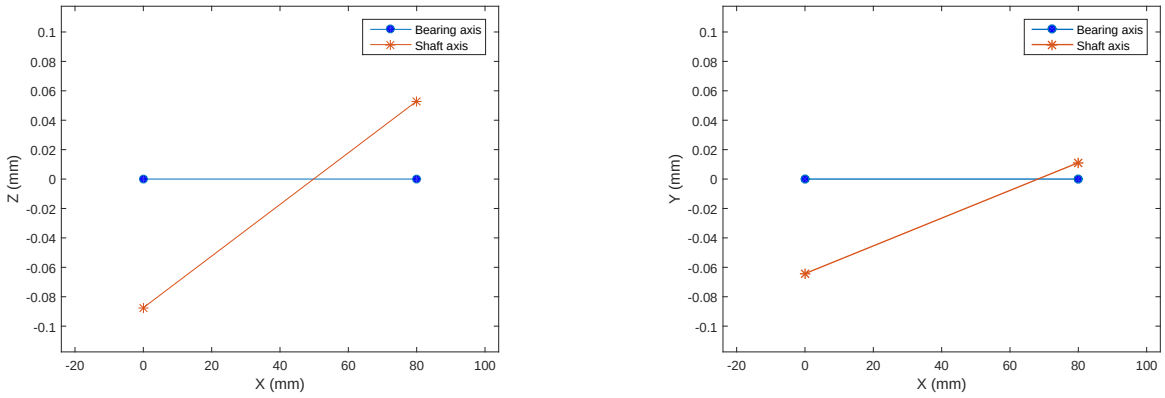

(a) Misalignment in the *xz*-plane.

(b) Misalignment in the *xy*-plane.

Figure 3.7. View of the misalignment in both *xz*-plane and *xy*-plane when solving the inverse problem for $\mathbf{F} = (0, 0, 3000\ \text{N})$ and $\boldsymbol{\tau} = (0, 70\ \text{N m}, 0)$.

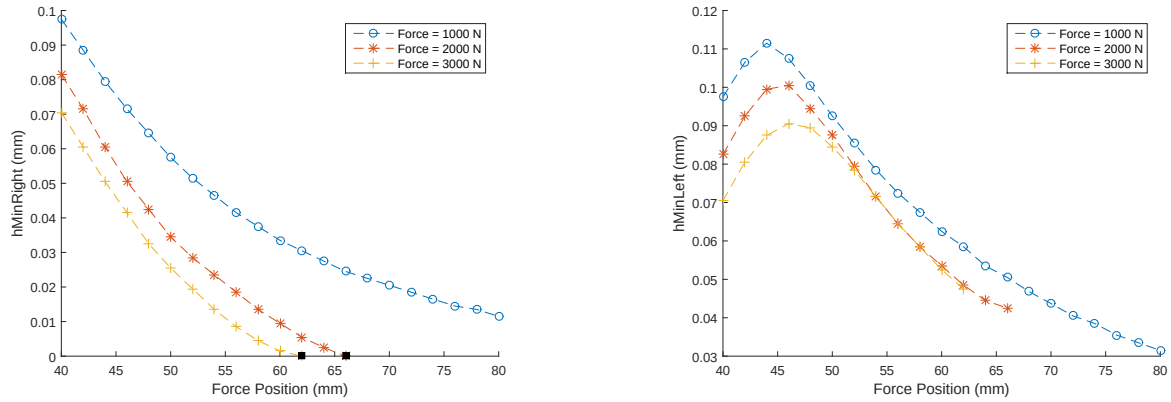

(a) Rear end behaviour.

(b) Front end behaviour.

Figure 3.8. Behaviour of the minimum gaps at the end-planes, related to the force applying position. Collisions are found for $|\mathbf{F}| = 3000$ N and $|\mathbf{F}| = 2000$ N at 62 mm and 66 mm respectively, at the rear end of the device.

Thus, we found finite load capacity as stated in (Asanabe, Akakoski, and Asai, 1971; Gómez-Mancilla and Nosov, 2002; Pinkus and Bupara, 1979; Vijayaraghavan and Keith, 1990). Also, notice that for higher force values the same pattern get repeated, but the contact is reached faster.

In Fig. 3.8b we present the same study at the front end. The behaviour is no longer strictly monotone. This obeys the fact that at the beginning, when the force is applied at the mid-plane (centre of mass), there is not misalignment and both end-planes centres decrease their positions in the same way. Nevertheless, when the distance between the centre of mass and the application point of the force increases, the centre of the front end goes up due to the torque, and the film thickness at that end-plane increases as well. At some point,

the centre of the front end crosses the closest point to the bearing axis (where the film thickness is maximum) and subsequent movements decrease the film thickness again, since the shaft is now approaching towards the bearing top at this end. As expected, we should see two crossing lines when inspecting the axes of a journal bearing subjected to this experiment. See for instance Fig. 3.7a to verify this effect. We show in Fig. 3.9 the paths of both end-planes centres for the case conducted with **F**=(0, 0, 3000 N) in Fig. 3.8. Similarly, if some

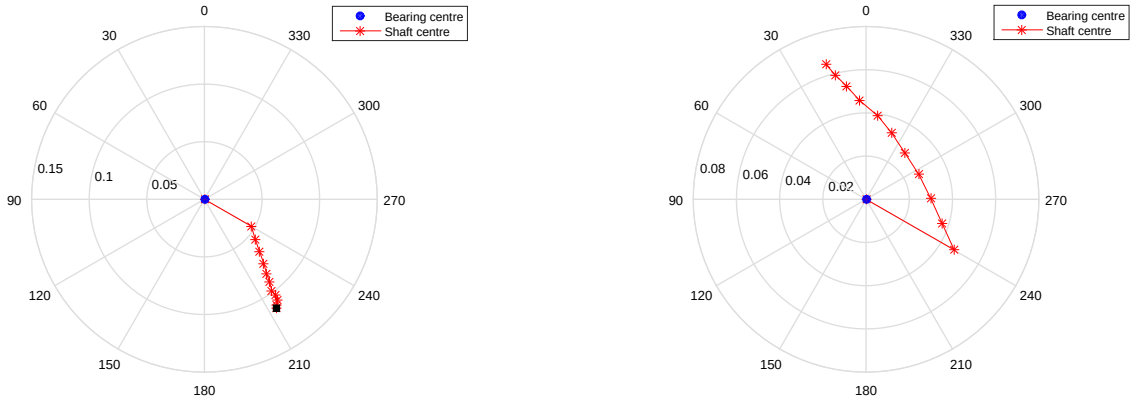

(a) Centre path at the rear end of the bearing.

(b) Centre path at the front end of the bearing.

Figure 3.9. Paths of both centres at their end-planes for $|\mathbf{F}| = 3000$ N. Both views are seen from the front end of the bearing.

contact point is found, the position where the centre is located is shown as a black square marker. Notice that both views are seen from the front end of the bearing. The behaviour of both centres can be easily confirmed, as described above.

We show in Fig. 3.10 the behaviour of the eccentricity λ related to the misalignment angle $\psi = (\beta^2+\varphi^2)^{\frac{1}{2}}$. Every marker on the dashed line corresponds to a solution of an inverse problem conducted with a force of 3000 N. As the experiment in Fig. 3.8, the force was applied from the bearing mid-plane to the bearing end until finding collision. A misalignment angle ψ was measured for each inverse problem at its equilibrium position. Notice how the eccentricity changes as the misalignment angle increases. We present in Fig. 3.10a the combined effect of eccentricity and the misalignment angle at the rear end-plane. According to the depicted experiment, the eccentricity – as expected – increases all the time. In Fig. 3.10b we present the behaviour at the front end-plane where a change of monotonicity also appears. Both show coherence with previous experiments.

On the other hand, Fig. 3.11 presents a similar experiment as in Fig. 3.8, but increasing the angular

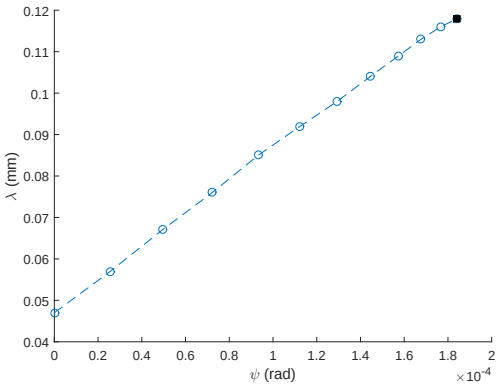

(a) Eccentricity behaviour vs the misalignment angle ψ in the bearing rear end-plane.

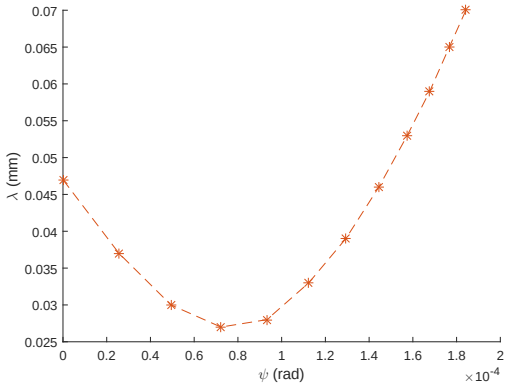

(b) Eccentricity behaviour vs the misalignment angle ψ in the bearing front end-plane.

Figure 3.10. Eccentricity vs the misalignment angle ψ at both bearing end-planes when solving the set of inverse problems for $\mathbf{F} = (0, 0, 3000\ \text{N})$ depicted in Fig. 3.8.

velocity to 3000 rpm. As expected the carrying capacity increases, and in consequence the contact points disappear. This demonstrates the influence of the velocity and also the consistence of our proposal.

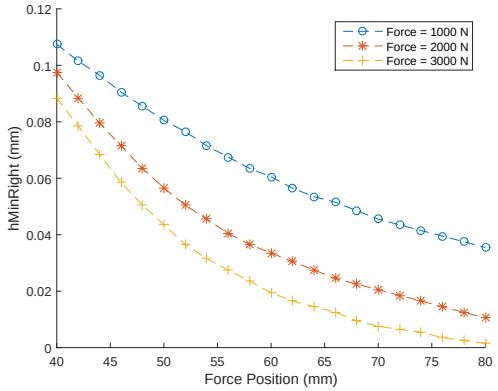

(a) Rear end-plane behaviour.

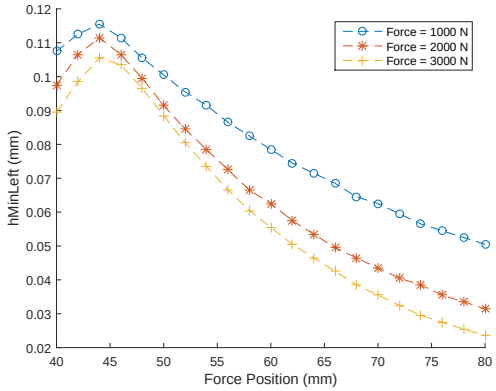

(b) Front end-plane behaviour.

Figure 3.11. Behaviour of the minimum gaps at the end-planes, related to the force applying position for an angular velocity of 3000 rpm.

Additionally, Fig. 3.12 shows the effect on the force exerted by the pressure when the slenderness ratio (L/D) changes. In the experiment the bearing length varies from 10 mm to 160 mm, with a step of 10 mm. The force was always computed for $\alpha = 3.752458$ rad, $\rho = 82.25$ µm, $\varphi = -0.000047$ rad, and $\beta = -0.000067$ rad. We notice, as stated in the literature, how the carrying capacity of the journal bearing is compromised as the slenderness ratio is much less than about $1/4$; see (Williams, 2005) for instance.

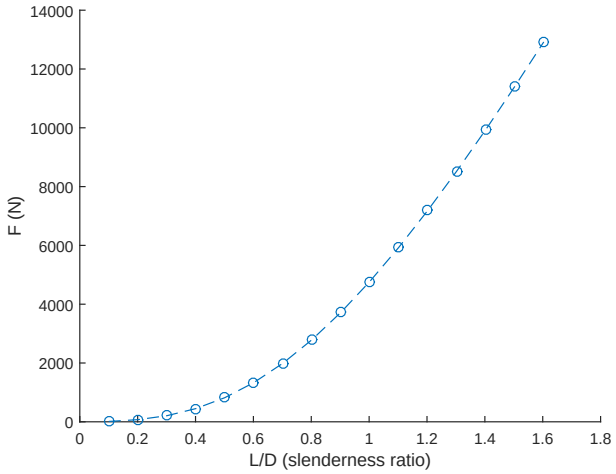

Figure 3.12. The effect on the force exerted by the pressure when the slenderness ratio (L/D) changes. The force was computed for $\alpha = 3.752458$ rad, $\rho = 82.25$ µm, $\beta = -0.000067$ rad and $\varphi = -0.000047$ rad.

Finally, we show the pressure behaviour as $\tan\beta \to C$. In Fig. 3.13 a numerical simulation with a high pressure value for a minimum of $(\tan\beta)/C = 0.999991$ is presented. It was computed in a grid of 400×400 elements. It numerically states that the uniform boundedness of the pressure is not guaranteed.

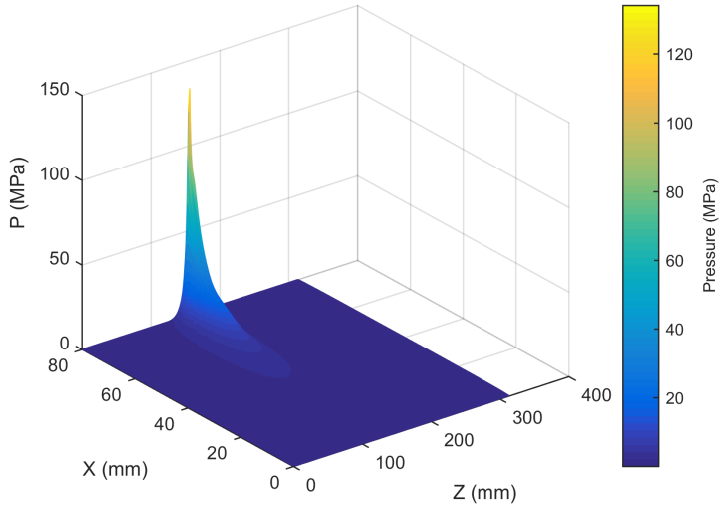

Figure 3.13. The peak pressure for a minimum of $(\tan\beta)/C = 0.999991$ considering $\bar{h}(\bar{x}, \theta, \beta) = 1 + \frac{\bar{x}}{C}\tan\beta\cos(\theta - \alpha)$ as in Sect. 3.1.

3.4.1 Grid convergence study

In this section we conduct a convergence study for verification of calculations, as suggested in (Roache, 1994; Roache, 2002). Since the exact solution for the force exerted by the lubricant pressure is unknown we perform three computations of forces, on a different grid each. We then calculate two Grid Convergence Indexes (GCIs) from fine grid to intermediate (GCI_{12}) and from intermediate to coarse grid (GCI_{23}). The GCI indicates how much the computed force will change with an additional refinement of the grid (Roache, 1998). A small value is preferable, since it suggests the force is within the asymptotic range. The grid information for the convergence study is provided in Table 3.2. It includes, for each experiment, the corresponding force value for the direct problem, computed for $\alpha = 3.665192$ rad, $\rho = 58.75$ µm, $\varphi = 0.000017$ rad and $\beta = 0.000017$ rad. Notice also that every grid has twice the number of elements as the previous grid on each direction. The geometrical and physical constants used are those in Table 3.1.

Table 3.2. Grid information for the convergence study.

No	Grid elements	Force ID	Force value (N)
1	800×320	F_1	7.335851×10^3
2	400×160	F_2	7.353513×10^3
3	200×80	F_3	7.390402×10^3

We determine the order of convergence c_s according to the force values. As we use in the convergence study a constant refinement ratio $r_t = 2$, we can perform a direct evaluation of c_s by Eq. (3.4.1); see (Roache, 1994) for details:

$$c_s = \ln\left(\frac{F_3 - F_2}{F_2 - F_1}\right) / \ln r_t, \tag{3.4.1}$$

$$c_s = \ln\left(\frac{7.390402 \times 10^3 \text{ N} - 7.353513 \times 10^3 \text{ N}}{7.353513 \times 10^3 \text{ N} - 7.335851 \times 10^3 \text{ N}}\right) / \ln 2,$$

$$c_s = 1.0625.$$

The GCI for the fine grid solution is then computed. It is defined as:

$$GCI_{jk} = \frac{f_s}{(r_t{}^{c_s} - 1)} \left|\frac{F_j - F_k}{F_j}\right|,$$

where f_s is a factor of safety, recommended to be $f_s = 1.25$ for comparisons of three grids; see (Roache, 1998) for details. The GCI for grids 1 and 2 is:

$$GCI_{12} = \frac{1.25}{(2^{1.0625} - 1)} \left| \frac{7.335851 \times 10^3 \text{ N} - 7.353513 \times 10^3 \text{ N}}{7.335851 \times 10^3 \text{ N}} \right|,$$
$$GCI_{12} = 0.0028.$$

Similarly, the GCI for grids 2 and 3 is:

$$GCI_{23} = \frac{1.25}{(2^{1.0625} - 1)} \left| \frac{7.353513 \times 10^3 \text{ N} - 7.390402 \times 10^3 \text{ N}}{7.353513 \times 10^3 \text{ N}} \right|,$$
$$GCI_{23} = 0.0058.$$

We then check that these solutions are within the asymptotic range of convergence by Eq. (3.4.2):

$$GCI_{23} = {r_t}^{c_s} GCI_{12}, \tag{3.4.2}$$
$$\frac{0.0058}{2^{1.0625}\, 0.0028} = 0.997598,$$

which is approximately 1 and indicates that the test succeeded. Based on this study we can also estimate the exact solution F_e by the Richardson extrapolation, using Eq. (3.4.3); see (Roache, 1994) for details:

$$F_e \cong F_1 + \frac{F_1 - F_2}{{r_t}^{c_s} - 1}, \tag{3.4.3}$$
$$F_e \cong 7.335851 \times 10^3 \text{ N} + \frac{7.335851 \times 10^3 \text{ N} - 7.353513 \times 10^3 \text{ N}}{2^{1.0625} - 1},$$
$$F_e \cong 7.319626 \times 10^3 \text{ N}.$$

Finally, we could say that the force exerted by the lubricant pressure, for the direct problem depicted, is estimated to be 7.319626×10^3 N with an error band of 0.0028.

3.4.2 Validation

To validate the whole numerical approach, we compare the predicted pressure values, in the bearing mid-plane, to published experimental data. For that, the work of Pierre, France, et al. (2004) was used, where the same geometrical and physical constants of the journal bearing were considered. Two experiments, one showing the maximum pressure and the other one showing the pressure field, both for different misalignment torques, are presented. For both simulations the pressure values in the bearing mid-plane were collected at the equilibrium position, after solving the corresponding inverse problem for each different misalignment torque. As in (ibid.) we performed the simulation for an angular velocity of 4000 rpm and a radial load of 9000 N. The misalignment torques, taken with respect to the bearing mid-plane, vary from 0 N m (aligned case) to 70 N m.

In Fig. 3.14 we show the maximum pressure in the bearing mid-plane computed by the algorithm and the experimental data, as shown in (ibid., p. 599). Comparisons between the experimental and the numerical

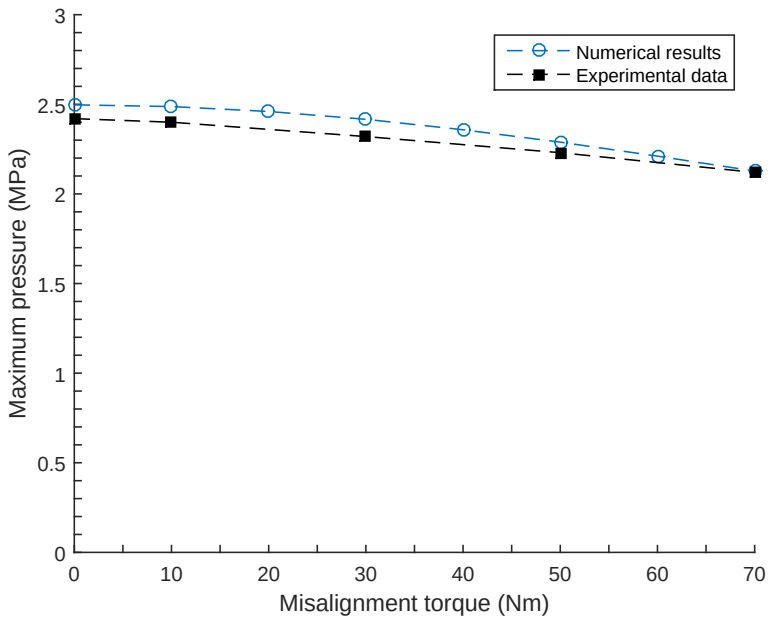

Figure 3.14. Maximum pressure obtained in the bearing mid-plane for different misalignment torques (ω = 4000 rpm and $\mathbf{F} = (0, 0, 9000\ \text{N})$).

results show small discrepancies for all the misalignment torques. In Fig. 3.15 we present the pressure field obtained in the bearing mid-plane for both the experiment and the numerical approach.

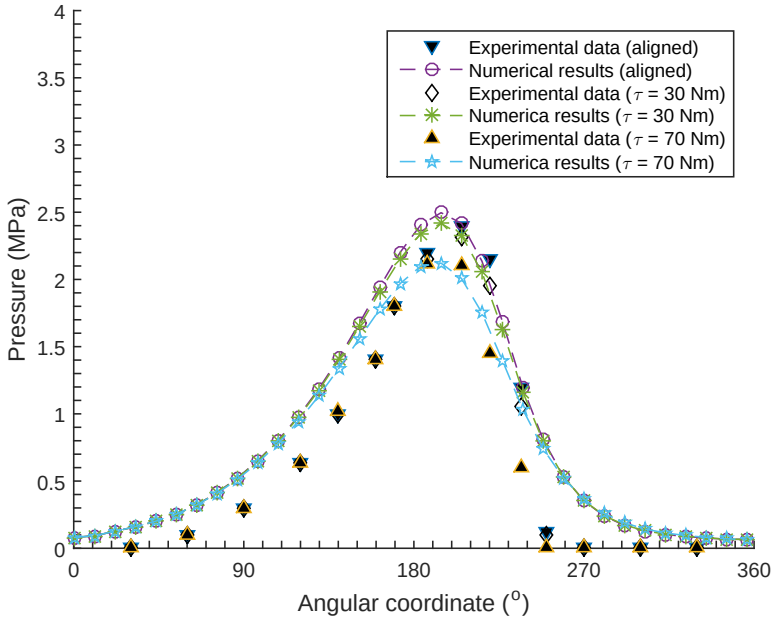

Figure 3.15. Pressure field in the bearing mid-plane for different misalignment torques (ω = 4000 rpm and $\mathbf{F}$ = (0, 0, 9000 N)).

The differences can be related to the fact that not all the surrounding phenomena (as temperature) are considered in our numerical model. Nevertheless, both experiments show an acceptable agreement between the output of our model and the experimental data. Such differences do not influence the determination of the maximum pressure, which is an essential factor when designing a journal bearing. The discrepancy was less than 0.0963 MPa, a value below the atmospheric pressure (0.101325 MPa). Thus, it makes us think that the algorithm can be used as a first prediction of the final position of a journal bearing under an imposed radial loading, considering misalignment and the cavitation phenomenon. In addition, it could be verified that misalignment tends to decrease the maximum pressure in the bearing mid-plane, as stated in the literature; see (Bouyer and Fillon, 2002) for instance.

CHAPTER 4

Prediction of contact with the Elrod-Adams cavitation model

In this chapter we state and solve the inverse problem for a misaligned journal bearing considering the Elrod–Adams cavitation model. We provide the approximation of the Heaviside function and propose a functional whose minimum is the solution to the direct problem. We consider a finite element discretization and accomplish the minimization stage by the algorithm Limited-Memory Broyden Fletcher Goldfarb Shanno (L-BFGS). The resolution of the inverse problem, based on $ACO_{\mathbb{R}}$, is also explained. Numerical experiments and discussion are also included.

4.1 Direct problem resolution

We define a parameter $\Lambda = \frac{1}{\overline{F_2}}\left(1 - \frac{\overline{F_1}}{\overline{F_0}}\right)$ and we rewrite Eq. (2.7.15) as:

$$\int_{\tilde{\Omega}} \tilde{h}^3 \nabla \bar{p} \nabla \bar{\phi} \mathrm{d}\tilde{\Omega} = -\int_{\tilde{\Omega}} \frac{\partial}{\partial \theta}\left(\vartheta \tilde{h} \Lambda\right) \bar{\phi}\, \mathrm{d}\tilde{\Omega}, \quad \forall \bar{\phi} \in \mathcal{K}, \quad \vartheta = \vartheta_0 \quad \text{in} \quad \Gamma_0, \tag{4.1.1}$$

with $\mathcal{K}$ defined in Eq. (2.7.14). For the numerical solution of Eq. (4.1.1), several techniques have been proposed. Mainly, the existing literature combines the MC with the FEM. To introduce the MC to the problem in the stationary case, we have adopted the technique based on introducing an artificial dependence

on time, already proposed in (Calvo, Durany, and Vázquez, 1997). In this manner, we define:

$$\hat{\bar{\phi}}(\theta, \tilde{x}, t) = \bar{\phi}(\theta, \tilde{x}),$$

$$\hat{\bar{p}}(\theta, \tilde{x}, t) = \bar{p}(\theta, \tilde{x}),$$

$$\hat{\tilde{h}}(\bar{\rho}, \alpha, \varphi, \beta, \theta, \tilde{x}, t) = \tilde{h}(\bar{\rho}, \alpha, \varphi, \beta, \theta, \tilde{x}),$$

$$\hat{\vartheta}(\theta, \tilde{x}, t) = \vartheta(\theta, \tilde{x}).$$

Thus, we can write the right-hand side of Eq. (4.1.1) in terms of the total derivative, assuming an artificial velocity $\boldsymbol{v} = 1$. So,

$$\frac{D}{Dt} = \frac{\partial}{\partial t} + \boldsymbol{v}\frac{\partial}{\partial \theta} = \frac{\partial}{\partial t} + \frac{\partial}{\partial \theta},$$

then, in the case of a stationary regime we have:

$$\frac{D}{Dt} = \frac{\partial}{\partial \theta}.$$

For simplicity in the notation we drop the superscripts $\hat{}$ of variables from now on. Thus, the problem in Eq. (4.1.1) is formulated as the stationary state of the following transient problem:

$$\int_{\tilde{\Omega}} \tilde{h}^3 \nabla \bar{p} \nabla \bar{\phi} \mathrm{d}\tilde{\Omega} = -\int_{\tilde{\Omega}} \frac{D}{Dt}\left(\vartheta \tilde{h} \Lambda\right) \bar{\phi} \mathrm{d}\tilde{\Omega}, \qquad \forall \bar{\phi} \in \mathcal{K}, \qquad \vartheta = \vartheta_0 \quad \text{in} \quad \Gamma_0, \tag{4.1.2}$$

with $\mathcal{K}$ defined in Eq. (2.7.14). The next step is to discretize the total derivative following the velocity field $\boldsymbol{v}$. For this purpose, an upwind schema of characteristics is used.

4.1.1 The Method of Characteristics

Let $\chi(\theta, t; \tau)$ denotes the position at time τ of a particle of fluid moving according to the velocity field $\boldsymbol{v} = (1, 0)$, and placed at the point θ at the reference time t. That is, χ is the solution to the final value problem:

$$\frac{\partial}{\partial \tau}\left(\chi(\theta, t; \tau)\right) = \boldsymbol{v}(\chi(\theta, t; \tau)),$$

$$\chi(\theta, t; t) = \theta.$$

So, the approximation of the total derivative is accomplished by using an upwind schema which follows the trajectory (or characteristics) of particles being analysed. We introduce the following notation:

- $\triangle t$ is the time step.
- $t^n = n\triangle t$.
- $\chi^n(\theta) = \chi(\theta, t^{n+1}; t^n)$ denotes the position at time t^n of a particle placed at the point θ at time t^{n+1}, when it moves according to the artificial velocity field $\boldsymbol{v}$.
- $g^{n+1}(\theta) = g(\theta, (n+1)\triangle t)$.

With the above notation we consider:

$$\frac{D}{Dt} g(\theta, t^{n+1}) \approx \frac{g^{n+1}(\theta) - g^n(\chi^n(\theta))}{\triangle t}. \tag{4.1.3}$$

As in fact the time dependence is fictitious, functions $g^{n+1}(\theta)$ and $g^n(\theta)$ are the same, and thereby we can recast Eq. (4.1.3) as:

$$\frac{D}{Dt} g(\theta) \approx \frac{g(\theta) - g(\chi^k(\theta))}{k}, \tag{4.1.4}$$

where k plays the role of the artificial time step and $\chi^k(\theta)$ denotes the position at time $t-k$ of a particle placed at the point θ at time t.

Then, substituting Eq. (4.1.4) into Eq. (4.1.2) yields a k-dependent family of equations, that approximates the original problem in Eq. (4.1.2) as:

$$\int_{\tilde{\Omega}} \tilde{h}^3 \nabla \bar{p} \nabla \bar{\phi} \mathrm{d}\tilde{\Omega} + \frac{1}{k} \int_{\tilde{\Omega}} \left(\vartheta \tilde{h} \Lambda\right) \bar{\phi} \mathrm{d}\tilde{\Omega} = \frac{1}{k} \int_{\tilde{\Omega}} \left(\vartheta \tilde{h} \Lambda\right) \circ \chi^k \bar{\phi} \mathrm{d}\tilde{\Omega}, \qquad \forall \bar{\phi} \in \mathcal{K}, \qquad \vartheta \in H(\bar{p}), \tag{4.1.5}$$

where symbol $\circ$ stands for the composition operator. At this point we proposed a fixed-point algorithm to define $\bar{p}^{n+1}$ as the solution of the following problem:

$$\int_{\tilde{\Omega}} \tilde{h}^3 \nabla \bar{p}^{n+1} \nabla \bar{\phi} \mathrm{d}\tilde{\Omega} + \frac{1}{k} \int_{\tilde{\Omega}} \vartheta^{n+1} \tilde{h} \Lambda \bar{\phi} \mathrm{d}\tilde{\Omega} = \frac{1}{k} \int_{\tilde{\Omega}} \left(\vartheta^n \tilde{h} \Lambda\right) \circ \chi^k \bar{\phi} \mathrm{d}\tilde{\Omega}, \quad \forall \bar{\phi} \in \mathcal{K}, \quad \vartheta^{n+1} \in H(\bar{p}^{n+1}), \tag{4.1.6}$$

which in fact is similar to the strategy of making time tends to infinity until reaching the stationary state.

4.1.2 The regularization approach for the Heaviside function

The problem under study is non-linear at each time step, due to the Heaviside function $H(\bar{p})$. A particular regularization technique has been widely used for dealing with the Heaviside function discontinuity, namely in (Calvo, Durany, and Vázquez, 1997; Durany, Pereira, and Varas, 2010) among others. They adopted a duality type method consisting in applying an algorithm proposed by Bermúdez and Moreno (1981) with a Yosida regularization for the Heaviside operator.

We propose a regularization approach by a cubic interpolating Hermite polynomial for the Heaviside function, which is derived following a divided-difference schema (Conte and De Boor, 1980; Quarteroni, Sacco, and Saleri, 2007). It is a recursive division process widely used, but not only, to calculate the coefficients of the interpolation polynomial in the Newton form. It is defined as:

$$\begin{aligned} f[x_i] &:= f(x_i), \\ f[x_i, x_{i+1}] &:= \frac{f[x_{i+1}] - f[x_i]}{x_{i+1} - x_i}, \\ f[x_i, x_{i+1}, x_{i+2}] &:= \frac{f[x_{i+1}, x_{i+2}] - f[x_i, x_{i+1}]}{x_{i+2} - x_i}, \\ &\vdots \\ f[x_i, x_{i+1}, \ldots, x_{i+k}] &:= \frac{f[x_{i+1}, x_{i+2}, \ldots, x_{i+k}] - f[x_i, x_{i+1}, \ldots, x_{i+k-1}]}{x_{i+k} - x_i}. \end{aligned} \tag{4.1.7}$$

It is important to remark the case when $x_0 = x_1 = \cdots = x_i$. In this case, $f(x)$ must have at least i continuous derivatives. Then, the leading coefficient is:

$$f[x_0, \ldots, x_i] = \frac{f^{(i)}(x_0)}{i!}, \qquad \text{if} \quad x_0 = x_1 = \cdots = x_i. \tag{4.1.8}$$

In the regularization approach we define a penalty parameter ϵ, which is used to construct the full set of points needed to derive an approximation for Eq. (2.7.13). So, we have two points $\{0, \epsilon\}$ with one derivative each $\{0, 0\}$, required to guarantee the approximation to be C^1. Thus, the points set is $\{x_i\} = \{0, 0, \epsilon, \epsilon\}$. The

whole procedure of computing the divided differences is shown in Table 4.1.

Table 4.1. Divided-difference table of the cubic interpolating Hermite polynomial for the Heaviside function.

	$i=0$	$i=1$	$i=2$	$i=3$
x_0	$f[0]=0$			
		$f[0,0]=0$		
x_1	$f[0]=0$		$f[0,0,\epsilon]=\frac{1}{\epsilon^2}$	
		$f[0,\epsilon]=\frac{1}{\epsilon}$		$f[0,0,\epsilon,\epsilon]=-\frac{2}{\epsilon^3}$
x_2	$f[\epsilon]=1$		$f[0,\epsilon,\epsilon]=-\frac{1}{\epsilon^2}$	
		$f[\epsilon,\epsilon]=0$		
x_3	$f[\epsilon]=1$			

The top entries in the columns inform about the leading coefficients needed to compute the interpolating polynomial following the Eq. (4.1.9):

$$p_n(x) = \sum_{i=0}^{n} f[x_0,\ldots,x_i] \prod_{j=0}^{i-1}(x - x_j). \tag{4.1.9}$$

Thus,

$$\begin{aligned} H_\epsilon(x) &= f[0] + f[0,0]x + f[0,0,\epsilon]x^2 + f[0,0,\epsilon,\epsilon]x^2(x-\epsilon), \\ H_\epsilon(x) &= \frac{1}{\epsilon^2}x^2 - \frac{2}{\epsilon^3}x^2(x-\epsilon), \\ H_\epsilon(x) &= \frac{1}{\epsilon^3}\left(3\epsilon x^2 - 2x^3\right). \end{aligned} \tag{4.1.10}$$

With that selection we may express the solution as a minimum of a convex functional at each time iteration. On the contrary, if the Yosida regularization is used, we need a different iterative procedure to deal with, since the convexity of the functional could not be guaranteed in the same way; see (Durany, Pereira, and Varas, 2008; Durany, Pereira, and Varas, 2010) for instance. In this manner, we define the approximation

function H_ϵ for the Heaviside's as follows:

$$H_\epsilon(x) = \begin{cases} 1, & \text{if } x > \epsilon, \\ \frac{1}{\epsilon^3}(3\epsilon x^2 - 2x^3), & \text{if } 0 \leq x \leq \epsilon, \\ 0, & \text{if } x < 0. \end{cases} \tag{4.1.11}$$

So, from now on, $\vartheta_\epsilon = H_\epsilon(\bar{p})$.

4.1.3 The associated functional

In this section we propose a functional whose minimum is the solution to Eq. (4.1.6).

Lemma 1. *Let J_ϵ be the following functional:*

$$J_\epsilon(\bar{p}) = \frac{1}{2}\int_{\tilde{\Omega}} \tilde{h}^3 |\nabla \bar{p}|^2 \mathrm{d}\tilde{\Omega} + \frac{1}{k}\int_{\tilde{\Omega}} \tilde{h}\Lambda\Phi_\epsilon(\bar{p})\mathrm{d}\tilde{\Omega} - \frac{1}{k}\int_{\tilde{\Omega}} \left(\vartheta\tilde{h}\Lambda\right) \circ \chi^k \bar{p}\mathrm{d}\tilde{\Omega}, \tag{4.1.12}$$

where function $\Phi_\epsilon(\bar{p})$ is defined as:

$$\Phi_\epsilon(\bar{p}) = \begin{cases} \bar{p} - \frac{1}{2}\epsilon, & \text{if } \bar{p} > \epsilon, \\ \frac{1}{\epsilon^3}(\epsilon\bar{p}^3 - \frac{1}{2}\bar{p}^4), & \text{if } 0 \leq \bar{p} \leq \epsilon, \\ 0, & \text{if } \bar{p} < 0. \end{cases} \tag{4.1.13}$$

Then, J_ϵ is convex, l.s.c and $\lim_{\bar{p}\to\infty} J_\epsilon(\bar{p}) = \infty$ for any $\epsilon > 0$.

Proof. Notice that Φ_ϵ is C^2, its second derivative is non-negative and the rest of the terms in J_ϵ are convex and l.s.c. Then, we have that J_ϵ is l.s.c and convex. A standard argument proves that $\lim_{\bar{p}\to\infty} J_\epsilon(\bar{p}) = \infty$. Thanks to Corollary III.20 in (Brézis, 1984, p. 45), $\bar{p}_\epsilon$ (the minimum of J_ϵ) is the unique solution to the penalized problem:

$$\int_{\tilde{\Omega}} \tilde{h}^3 \nabla \bar{p}_\epsilon \nabla \bar{\phi} \mathrm{d}\tilde{\Omega} + \frac{1}{k}\int_{\tilde{\Omega}} \left(\vartheta\tilde{h}\Lambda\right)\bar{\phi}\mathrm{d}\tilde{\Omega} = \frac{1}{k}\int_{\tilde{\Omega}} \left(\vartheta_\epsilon\tilde{h}\Lambda\right) \circ \chi^k \bar{\phi}\mathrm{d}\tilde{\Omega}, \quad \forall \bar{\phi} \in \mathcal{K}, \tag{4.1.14}$$
$$\vartheta_\epsilon \in H_\epsilon(\bar{p}_\epsilon).$$

Since $H_\epsilon \leq 1$, we have that $\bar{p}_\epsilon$ is uniformly bounded in $H^1(\tilde{\Omega})$. So, there exists a subsequence $\bar{p}_{\epsilon i}$ which converges weakly to $\bar{p}_*$ which satisfies Eq. (4.1.5). Since the solution to Eq. (4.1.5) is unique, see (Álvarez and Oujja, 2003; Martin, 2005), we have that any other subsequence $\bar{p}_{\epsilon j}$ converges to $\bar{p}_*$. □

On the other hand, and taking advantage of the region under study we perform the spatial approximation by piecewise quadrangular Lagrange Q_1 finite elements. That is, $\bar{p}$, $\bar{\phi}$ and ϑ are approximated as follows:

$$\bar{p} \approx \bar{p}_{\mathrm{f}} = \sum_{j=1}^{n} N_j p_j, \tag{4.1.15}$$

$$\bar{\phi} \approx \bar{\phi}_{\mathrm{f}} = \sum_{j=1}^{n} N_j \phi_j, \tag{4.1.16}$$

$$\vartheta \approx \vartheta_{\mathrm{f}} = \sum_{j=1}^{n} N_j \vartheta_j, \tag{4.1.17}$$

where N_j stands for the shape function evaluated at node j and parameter ϕ_j stands for the discrete pressure value also evaluated at node j. Subscript f stands for the finite element approximation. Now, we solve by a fixed-point iteration the discretized problem:

$$\begin{aligned} \int_{\tilde{\Omega}} \tilde{h}^3 \nabla \bar{p}_{\mathrm{f}}^{n+1} \nabla \bar{\phi}_{\mathrm{f}} \mathrm{d}\tilde{\Omega} + \frac{1}{k} \int_{\tilde{\Omega}} \vartheta_{\mathrm{f}}^{n+1} \tilde{h} \Lambda \bar{\phi}_{\mathrm{f}} \mathrm{d}\tilde{\Omega} &= \frac{1}{k} \int_{\tilde{\Omega}} \left(\vartheta_{\mathrm{f}}^{n} \tilde{h} \Lambda \right) \circ \chi^k \bar{\phi}_{\mathrm{f}} \mathrm{d}\tilde{\Omega}, \\ \vartheta_{\mathrm{f}}^{n+1} &= H_\epsilon(\bar{p}_{\mathrm{f}}^{n+1}), \end{aligned} \tag{4.1.18}$$

which must minimize at each iteration the following functional:

$$J(\bar{p}_{\mathrm{f}}^{n+1}) = \frac{1}{2} \int_{\tilde{\Omega}} \tilde{h}^3 |\nabla \bar{p}_{\mathrm{f}}^{n+1}|^2 \mathrm{d}\tilde{\Omega} + \frac{1}{k} \int_{\tilde{\Omega}} \tilde{h} \Lambda \Phi_\epsilon(\bar{p}_{\mathrm{f}}^{n+1}) \mathrm{d}\tilde{\Omega} - \frac{1}{k} \int_{\tilde{\Omega}} \left(\vartheta_{\mathrm{f}}^{n} \tilde{h} \Lambda \right) \circ \chi^k \bar{p}_{\mathrm{f}}^{n+1} \mathrm{d}\tilde{\Omega}. \tag{4.1.19}$$

We use the algorithm L-BFGS to perform the minimization stage (Nocedal and Wright, 2006), with the line search approach widely depicted in (Moré and Thuente, 1994). The L-BFGS algorithm is useful in this case as we are dealing with a large scale problem whose Hessian matrix cannot be computed at a reasonable cost. In fact, the main idea of this algorithm is to use curvature information from only the most recent iterations to construct the Hessian approximation (Nocedal and Wright, 2006). The gradient needed for the algorithm is presented in Eq. (4.1.20):

$$\nabla J(\bar{p}_{\mathrm{f}}^{n+1}) = \int_{\tilde{\Omega}} \tilde{h}^3 |\nabla \bar{p}_{\mathrm{f}}^{n+1}| \mathrm{d}\tilde{\Omega} + \frac{1}{k} \int_{\tilde{\Omega}} \tilde{h} \Lambda H_{\epsilon}(\bar{p}_{\mathrm{f}}^{n+1}) \mathrm{d}\tilde{\Omega} - \frac{1}{k} \int_{\tilde{\Omega}} \left(\vartheta_{\mathrm{f}}^{n} \tilde{h} \Lambda \right) \circ \chi^{k} \mathrm{d}\tilde{\Omega}. \tag{4.1.20}$$

4.2 Inverse problem resolution

As in Chapter 3, we consider the balance of force and torque components involved, (see Sect. 2.8). According to the domain $\tilde{\Omega}$, introduced in Sect. 2.6, we define the residual E as follows:

$$E(x_k) = \begin{bmatrix} \bar{F}_{\mathrm{y}} & - & \frac{1}{|\mathbf{F}|} \int_{\tilde{\Omega}} \frac{\mu_0 \omega R^4}{C^2} \bar{\phi}_k \sin\theta \mathrm{d}\theta \mathrm{d}\tilde{x} \\ \bar{F}_{\mathrm{z}} & - & \frac{1}{|\mathbf{F}|} \int_{\tilde{\Omega}} \frac{\mu_0 \omega R^4}{C^2} \bar{\phi}_k \cos\theta \mathrm{d}\theta \mathrm{d}\tilde{x} \\ \bar{\tau}_{\mathrm{y}} & + & \frac{1}{|\tau|} \int_{\tilde{\Omega}} \frac{\mu_0 \omega R^5}{C^2} \tilde{x} \bar{\phi}_k \cos\theta \mathrm{d}\theta \mathrm{d}\tilde{x} \\ \bar{\tau}_{\mathrm{z}} & - & \frac{1}{|\tau|} \int_{\tilde{\Omega}} \frac{\mu_0 \omega R^5}{C^2} \tilde{x} \bar{\phi}_k \sin\theta \mathrm{d}\theta \mathrm{d}\tilde{x} \end{bmatrix} : \mathbb{R}^4 \mapsto \mathbb{R}. \tag{4.2.1}$$

where $\bar{\phi}_k$ is the k$^{\mathrm{th}}$ solution to the hydrodynamic problem in Eq. (4.1.19), whose coefficient depends on $x_k = \{\bar{\rho}_k, \alpha_k, \varphi_k, \beta_k\}$, such that $E(x_0) \geq E(x_1) \geq \cdots \geq E(x_r)$ for r solutions with the following constraints:

$$\bar{\rho}_k \in [0, 1), \tag{4.2.2}$$

$$\alpha_k \in [0, 2\pi], \tag{4.2.3}$$

$$\varphi_k \in \left[\arctan\left(-\frac{CR}{L}(1 + \bar{\rho}_k \sin\alpha_k) \right), \arctan\left(\frac{CR}{L}(1 - \bar{\rho}_k \sin\alpha_k) \right) \right], \tag{4.2.4}$$

$$\begin{aligned} \beta_k \in \Bigg[& \arctan\left(-\frac{R}{L} \left(\left[C^2 - \left(\frac{L}{R} \tan\varphi_k + C\bar{\rho}_k \sin\alpha_k \right)^2 \right]^{1/2} - C\bar{\rho}_k \cos\alpha_k \right) \right), \\ & \arctan\left(\frac{R}{L} \left(\left[C^2 - \left(\frac{L}{R} \tan\varphi_k + C\bar{\rho}_k \sin\alpha_k \right)^2 \right]^{1/2} - C\bar{\rho}_k \cos\alpha_k \right) \right) \Bigg]. \end{aligned} \tag{4.2.5}$$

Thus, the objective is to minimize the L^2-norm of the residual E defined in Eq. (4.2.1), in least squares sense, i.e.

$$\min_{x_k \in \mathbb{R}^4} \|E(x_k)\|_2^2, \tag{4.2.6}$$

subject to the constraints defined in Eqs. (4.2.2-4.2.5).

However, for the numerical resolution, the strategy is to minimize the residual E through an extension of the metaheuristic ACO, applied to continuous domains (Socha and M. Dorigo, 2008). Specifically, we

propose to use $\text{ACO}_{\mathbb{R}}$ for the minimization stage, with continuous domains defined by intervals for each dimension.

The gradient based algorithms, like the one used in Chapter 3, require the optimized function to be continuous and differentiable, making them limited for this reason. The $\text{ACO}_{\mathbb{R}}$, as well as all other algorithms for continuous optimization mentioned earlier, do not have such limitations, which makes them much more general and preferable for the present inverse problem with the Elrod–Adams cavitation model.

To obtain the dimensionless pressure minimizer $\bar{\phi}^*$, four unknown parameters $(\bar{\rho}^*, \alpha^*, \varphi^*, \beta^*)$ are needed, which determine the shaft position and misalignment of the system. As other minimization algorithms, $\text{ACO}_{\mathbb{R}}$ is an iterative minimization procedure that, starting from an initial guess vector $x_0 = \{\bar{\rho}_0, \alpha_0, \varphi_0, \beta_0\}$, generates in the set of admissible positions of the parameters, a sequence of ever improving solutions x_1, $x_2, \ldots, x_r$ that minimize $\|E\|_2^2$. At the minimum, where the equilibrium between the imposed and hydrodynamic loads is attained, we are also predicting the final position of the shaft and the final pressure distribution, this time for the Elrod–Adams cavitation model.

A solution $x_k \in \mathbb{R}^4$ is a feasible solution if and only if x_k^i, which represents the value of x_k in the coordinate $i \in \{1, 2, 3, 4\}$, satisfies its corresponding constraint. Let l_i and u_i be the lower and upper limit values respectively of the i coordinate. The following holds: $l_1 \leq x_k^1 < u_1$, $\quad l_2 \leq x_k^2 \leq u_2$ and $l_i < x_k^i < u_i$, for $i \in \{3, 4\}$.

It is well-known that an ACO algorithm tries to solve an optimization problem by iterating over the following two stages:

1. Construction of candidate solutions in a probabilistic way over the search space, using a probability distribution.
2. Candidate solutions are used to change the probability distribution in a way that predispose future sampling towards high quality solutions.

The central component of ACO algorithms is the pheromone model, which is used to probabilistically sample the search space (ibid.). Concerning $\text{ACO}_{\mathbb{R}}$, it works with a solution archive A_n which represents its pheromone model (Liao, Montes de Oca, et al., 2011). It starts filling the solution archive A_n with n_a solutions generated uniformly at random, in a way that each component of a solution satisfies its constraint, see Alg. 1.4. The archive keeps solutions sorted according to the value of their objective functions. Next, at each

iteration a new set of n_s solutions are probabilistically generated and added to A_n, see Alg. 1 from line 25 to line 32. The algorithm sorts the $n_a + n_s$ available solutions according to their quality (from best to worst) and keeps only the best n_a solutions, see Alg. 1, lines 33 and 34. This process guides the search towards the best found solutions (Blum, Cardoso, and Herrera, 2009).

The solution construction procedure is based on a probabilistic density function (PDF) called a Gaussian kernel G^i, which is defined as a weighted sum of several Gaussian functions g_k^i, where k is a solution index and i is a coordinate index. The Gaussian kernel for coordinate i is:

$$G^i(x) = \sum_{k=1}^{n} w_k g_k^i(x) = \sum_{k=1}^{n} w_k \frac{1}{\sigma_k^i \sqrt{2\pi}} \exp\left(-\frac{(x-\mu_k^i)^2}{2(\sigma_k^i)^2}\right), \tag{4.2.7}$$

where parameters w_k, μ_k^i, σ_k^i stand for the weight, mean and standard deviation respectively of the Gaussian function $g_k^i(x)$. Notice that, the Gaussian kernel G^i is constructed using only the i^{th} coordinates of all n_a solutions of the archive.

The Gaussian function g_k corresponds to the solution x_k of archive A_n. In our problem, for the construction of the new solution x_k, an artificial ant performs 4 steps. At the i^{th} step, an ant chooses a value for the i dimension of x_k. This is accomplished by sampling G^i using the n_a solutions of the archive. Firstly, the weight is calculated using a Gaussian function as:

$$w_k = \frac{1}{qn_a \sqrt{2\pi}} \exp\left(\frac{-(rank(k)-1)^2}{2(qn_a)^2}\right), \tag{4.2.8}$$

where $rank(k)$ is the rank of solution x_k in A_n, and q is a parameter of the algorithm representing the locality of the search process. The weight w_k is defined as the value for the Gauss function with argument k, mean 1 and a standard deviation qn_a. This means that the smaller is k, the greater is the weight of g_k. In other words, Gaussian kernels that correspond to the best solutions have greater weights than remaining solutions. In addition, when q is small, better solutions are preferred and if it is large, the weight distribution becomes more uniform (ibid.). The influence of parameter q in $ACO_{\mathbb{R}}$ is similar to adjusting the balance of the pheromone updating methods used in the ACO algorithm for the combinatorial optimization between "best iteration" vs. "best so far" (Stützle and Hoos, 2000).

The sampling of G^i is performed in two stages. The first one is to choose probabilistically one of the

Gaussian functions corresponding to the Gaussian kernel PDF, see Alg. 1.27. The probability $\mathcal{P}_k$ of choosing the k$^{\text{th}}$ Gaussian function is given by:

$$\mathcal{P}_k = \frac{w_k}{\sum_{j=1}^{n_a} w_j}. \tag{4.2.9}$$

Stage two consists of sampling the chosen Gaussian function (i.e., at coordinate i the function g_k^i). This can be done, using a random number generator that is able to generate random numbers according to a parametrized normal distribution (ibid.), see Alg. 1.28. This sampling of two stages is equivalent to the sampling process of the Gaussian kernel G^i, defined in Eq. (4.2.7). According to the domain intervals it might be possible that values from the sampling process are not valid. Regular implementations of $\text{ACO}_{\mathbb{R}}$ reject such values and perform a new sampling.

Parameters μ_k^i and σ_k^i must be defined in advance to sampling g_k^i. At each step $\mu_k^i = x_k^i$ and σ_k^i is calculated as the average distance from x_k^i to the values of dimension i in the remaining solutions of the archive, see Alg. 1 from line 16 to line 23. We multiply the result by the parameter $\xi > 0$, which is the same for all the dimensions and influences the way the long term memory is used in the $\text{ACO}_{\mathbb{R}}$.

$$\sigma_k^i = \xi \sum_{j=1}^{n_a} \frac{\|x_k^i - x_j^i\|}{n_a - 1}. \tag{4.2.10}$$

Actually, its effect is similar to that of the pheromone evaporation rate in ACO. It influences the convergence speed of the algorithm. It is well-known that every algorithm must use some strategy to diversify the search, for not getting stuck in a local minimum, but still converging in the global optimum. These are two contradictory goals (Socha, 2008) since an algorithm is expected to converge quickly, but not to converge entirely to a local minimum. The algorithm must decide to focus on diversification (higher robustness), or intensification (higher convergence speed–higher efficiency). In this sense, $\text{ACO}_{\mathbb{R}}$ uses three parameters in order to define the balance between diversification and intensification. Parameters such as the learning rate and the number of ants are those that most influence the robustness of the algorithm. In the case of $\text{ACO}_{\mathbb{R}}$, the slower the learning rate (higher values of ξ) and the larger the solution archive size, the more robust is the algorithm. However, the convergence speed will be slower. In $\text{ACO}_{\mathbb{R}}$, there is another parameter to control the diversification of the search process, q. When q approaches 0, it means that only the Gaussian function associated with the best solution found so far is used for generating further solutions by the ants. When us-

ing larger q, the algorithm samples the search space based on a larger number of reasonably good solutions, rather than only on the best one found so far. The search is more diversified and the algorithm performs more robustly. Unfortunately, higher robustness usually means lower efficiency and slower convergence speed; see (Socha, 2008; Socha and M. Dorigo, 2008).

Moreover, we note that at step i, the standard deviation needs only to be known for the single Gaussian function g_k^i, chosen in stage one.

The proposed $ACO_{\mathbb{R}}$ is presented in Alg. 1. Considering that we deal with a large scale direct problem and motivated by the inherent parallelism of the $ACO_{\mathbb{R}}$ and possible computation speed up we propose an implementation of the algorithm with parallel regions for time-consuming tasks, using OpenMP; see Alg. 1 at lines 3 and 24. To ensure that same components of σ_k or μ_k are not calculated many times by different ants we calculate the whole vectors σ_k and μ_k in advance.

4.3 Numerical results and discussion

In this chapter we addressed the mathematical formulation and numerical solution of a misaligned journal bearing with an axial supply groove and subjected to radial loading. The unknowns of the problem were the pressure of the lubricant, the concentration of the lubricant and the shaft position, which was obtained coupling the hydrodynamic model to Newton's second law. The forces acting on the system were the force exerted by the pressure of the lubricant and the exterior force applied to the system. We also considered their corresponding torques. We addressed the cavitation phenomenon by the Elrod–Adams model, which includes a non-linear term given by the Heaviside function. We performed a regularization of this function by a cubic interpolating Hermite polynomial, which allowed us to find a suitable convex functional to minimize, whose minimum is the solution to the penalized direct problem Eq. (4.1.19). The minimization stage was performed via the algorithm L-BFGS with the line search approach by (Moré and Thuente, 1994). The numerical approach to solve the associated inverse problem was based on the metaheuristic $ACO_{\mathbb{R}}$, an approach inspired by the ants' foraging behaviour and successfully applied to continuous optimization. To speed up the solution of the inverse problem, several instances of the direct problem (a large scale problem) are solved in parallel using OpenMP. By solving the inverse problem in a misaligned journal bearing with the Elrod–Adams cavitation model, we provide to engineers, with the benefits of this model, an approach to

Algorithm 1 The $ACO_{\mathbb{R}}$ algorithm implemented with parallel regions.

procedure ACOR(E)
  input: objective function E
  #pragma omp parallel for
  for $k \leftarrow 1, n_a$ **do**
    $A_n^k \leftarrow x_k$, generated uniformly at random such that every x_k^i is within its corresponding interval.
    {compute each value of the objective function for x_t, i.e. $E(x_k)$ } ▷ Time-consuming task!
  end for
  $A_n \leftarrow$ sort A_n according to the value of the objective functions $E(x_k)$
  for $k \leftarrow 1, n_a$ **do**
    $w_k \leftarrow$ compute each solution weight according to Eq. (4.2.8)
  end for
  for $k \leftarrow 1, n_a$ **do**
    $\mathcal{P}_k \leftarrow$ compute the probability of choosing the k$^{\text{th}}$ Gaussian function according to Eq. (4.2.9)
  end for
  while stop conditions not met **do** ▷ Main loop of $ACO_{\mathbb{R}}$
    for $k \leftarrow 1, n_a$ **do**
      $\mu_k \leftarrow x_k$
    end for
    for $k \leftarrow 1, n_a$ **do**
      for $j \leftarrow 1, n_a$ **do**
        $\sigma_k^i \leftarrow$ compute the standard deviation at each dimension i according to Eq. (4.2.10)
      end for
    end for
    #pragma omp parallel for
    for $t \leftarrow 1, n_s$ **do** ▷ The construction of candidate solutions
      for $i \leftarrow 1, 4$ **do**
        $g \leftarrow$ choose by roulette choice an individual Gaussian function with probability $\mathcal{P}$
        $x_t^i \leftarrow \mu_g^i + \sigma_g^i \times randn()$: every x_t^i must be within its corresponding interval
      end for
      {compute each value of the objective function for x_t, i.e. $E(x_t)$ } ▷ Time-consuming task!
    end for
    $A_n \leftarrow x_t : t \in \{1, \ldots, n_s\}$ ▷ The archive A_n is augmented with new n_s solutions
    $A_n \leftarrow$ sort the augmented A_n according to the value of the objective functions E
    $A_n \leftarrow$ shrink A_n to the initial size n_a
    $bestAnt \leftarrow A_n^0$
  end while
  output: bestAnt
end procedure

predict cavitation and contact in such devices subjected to radial loading. The algorithm provided, showed another way of solution to the present problem, in particular for the inverse problem which we solved by the metaheuristic $ACO_{\mathbb{R}}$. In addition, we provided to engineers the Eq. (2.5.11) and Eq. (2.5.12), which

Table 4.2. Geometrical, physical and numerical constants.

Parameter	Symbol	Value
Shaft angular velocity	ω [rpm]	1500
Journal bearing length	L [mm]	80
Radial clearance	C [μm]	117.5
Shaft radius	R [mm]	49.89
Fluid viscosity	μ [Pa s]	0.023
Reference viscosity	μ_0 [Pa s]	0.0813
Supply pressure	p_s [MPa]	0.08
Penalty parameter in the Heaviside approximation	ϵ [dimensionless]	5e-12
Number of ants in the solution archive	n_a [ants]	70
Number of new ants	n_s [ants]	50
Locality of the search process in the $ACO_{\mathbb{R}}$	q [dimensionless]	0.0103
Speed of convergence in the $ACO_{\mathbb{R}}$	ξ [dimensionless]	0.8257
Initial pressure	p_0 [MPa]	1
Initial $\bar{\rho}$	$\bar{\rho}_0$ [dimensionless]	0.5
Initial α	α_0 [rad]	$\frac{\pi}{6}$
Initial φ	φ_0 [rad]	1.745e-5
Initial β	β_0 [rad]	1.745e-5

define the correct range of admissible misalignment angle projections, computed for the specific domain of the mathematical formulation of this problem.

In this section, we also present numerical tests which try to verify the performance and coupling of the different numerical approaches involved. The dimensionless domain $\tilde{\Omega} = [0, 2\pi] \times [0, \frac{L}{R}]$ is discretized using a 200×80 finite elements mesh (16000 four-noded quadrangles) and an attenuation factor $\delta = 0.93$. Unless other values are specified for the experiments, the geometrical and physical constants, taken from (Bouyer and Fillon, 2002) and the $ACO_{\mathbb{R}}$ numerical constants, taken from (Leguizamón and Coello, 2010b), are those in Table 4.2.

Again, the problem is solved in a dimensionless domain, but most of the results are back transformed and presented in their real scales and units when it does not affect the visualization purpose.

In Fig. 4.1 we show the equilibrium position and the resulting pressure map wrapped around the bearing, when applying an external force of 3000 N in the "z" direction and a torque of 70 N m in the "y" direction. This is equivalent to applying the force at 23.3 mm from the origin. That force is represented by the vertical arrow in this figure. As expected, the peak pressure map is located accordingly to the force position and shaft displacement, and tends to move towards the bearing front in this case, representing the reality. Notice

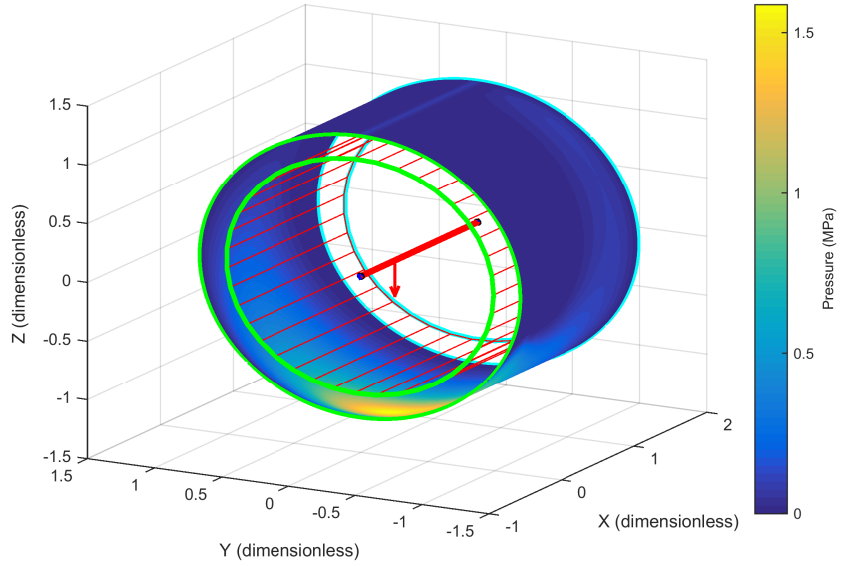

Figure 4.1. Solution to the inverse problem for $\mathbf{F} = (0, 0, 3000\ \mathrm{N})$ and $\boldsymbol{\tau} = (0, 70\ \mathrm{N\,m}, 0)$. The equilibrium position is found at $\bar{\rho} = 108.73\ \mu\mathrm{m}$, $\alpha = 3.704084$ rad, $\varphi = -0.000045$ rad and $\beta = -0.000094$ rad.

that a normalized journal bearing has been used in favour of visualization. The equilibrium position is found at $\bar{\rho} = 108.73\ \mu\mathrm{m}$, $\alpha = 3.704084$ rad, $\varphi = -0.000045$ rad and $\beta = -0.000094$ rad. Despite we are using a different cavitation model, this solution for the inverse problem is very close to the one obtained in Sect. 3.4, which is in accordance with the literature. Note also that the colour bar presents real pressure values and the corresponding unit. In addition, with this solution, attained with our numerical approach, we verify our hypothesis on how to predict the final position of the shaft and the final pressure distribution in a misaligned journal bearing with the Elrod–Adams cavitation model.

A perspective view for the pressure is presented at the equilibrium position in Fig. 4.2 and a contour map in Fig. 4.3. Both verify the peak pressure behaviour.

In Fig. 4.4 we show the concentration contour map at the equilibrium position of the inverse problem under study. Cavitation regions, within isolines with $\vartheta = 1$, should be noticed. They appear at zones with zero pressure values of Fig. 4.3, as it was expected. In Fig. 4.5 we zoom in the cavitated region at the bottom right corner of Fig. 4.4, the divergent zone accordingly to the shaft movement. The hypothesis of the Elrod–Adams cavitation model, the fluid-air mixture, is verified with different lubricant concentrations that represent the saturation of fluid in the mixture.

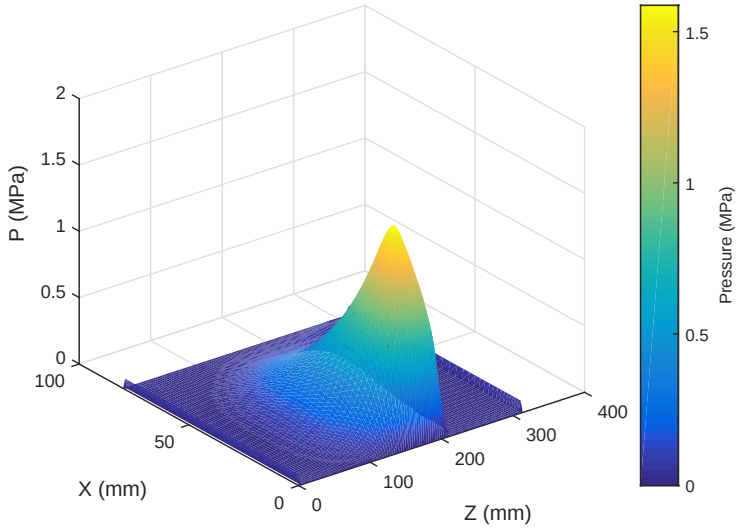

Figure 4.2. Perspective view of the pressure when solving the inverse problem with the Elrod–Adams model for $\mathbf{F} = (0, 0, 3000\ \text{N})$ and $\boldsymbol{\tau} = (0, 70\ \text{N m}, 0)$.

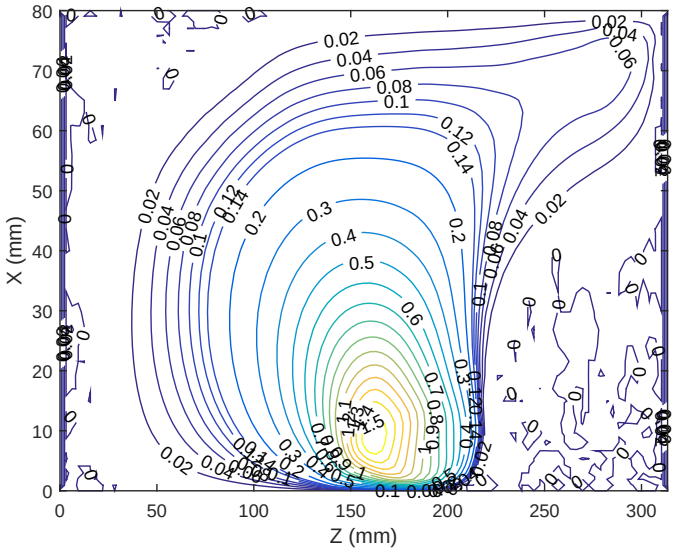

Figure 4.3. Contour map of the pressure when solving the inverse problem with the Elrod–Adams model for $\mathbf{F} = (0, 0, 3000\ \text{N})$ and $\boldsymbol{\tau} = (0, 70\ \text{N m}, 0)$.

In Fig. 4.6 we show the behaviour of the fluid film thickness h at the equilibrium position with the Elrod–Adams model, when solving the inverse problem for $\mathbf{F} = (0, 0, 3000\ \text{N})$ and $\boldsymbol{\tau} = (0, 70\ \text{N m}, 0)$. The minimum value is 8.71 µm, represented in the figure by a circular marker. It is located at $x = 0$ mm, $\theta = 3.7699$ rad ($\theta R = 188.0808$ mm). Accordingly to the solution obtained for the inverse problem it is also

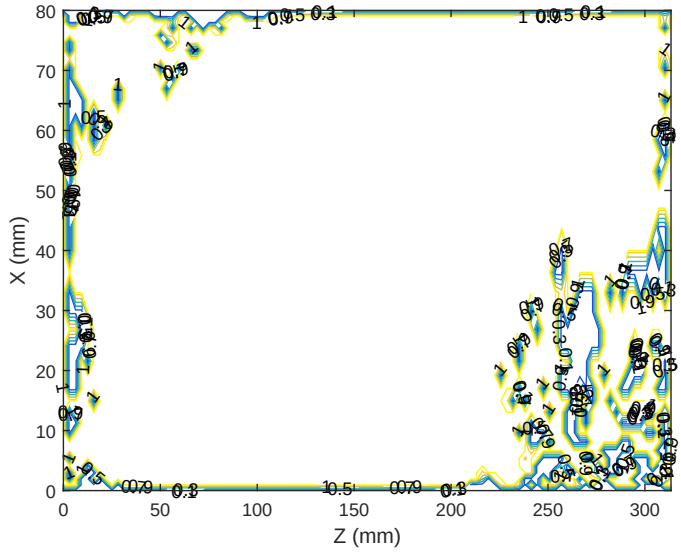

Figure 4.4. Concentration contour map at the equilibrium position of the inverse problem for $\mathbf{F} = (0, 0, 3000\ \text{N})$ and $\boldsymbol{\tau} = (0, 70\ \text{N m}, 0)$.

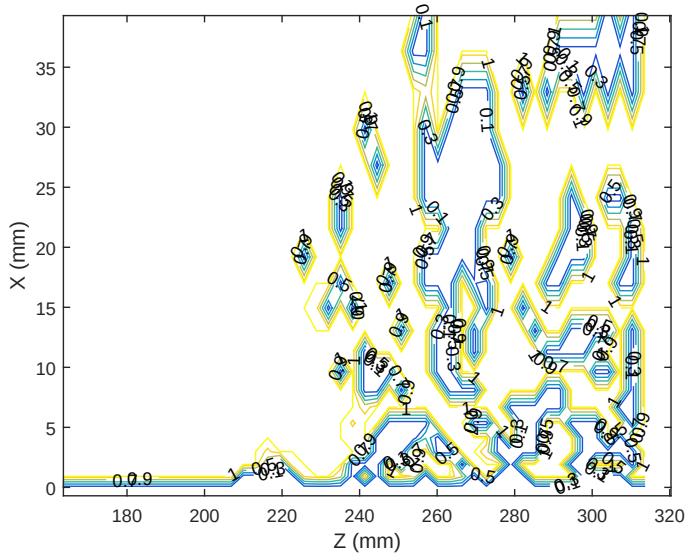

Figure 4.5. A zoom for the concentration contour map at the bottom right corner of Fig. 4.4.

expected this result be similar to the minimum attained in Fig. 3.6.

Figures 4.7a and 4.7b present the misalignment of the axes on the *xz*-plane and *xy*-plane respectively at the equilibrium position. Accordingly to the force applying position, the centre at the front end, as expected, approaches more towards the contact in both figures.

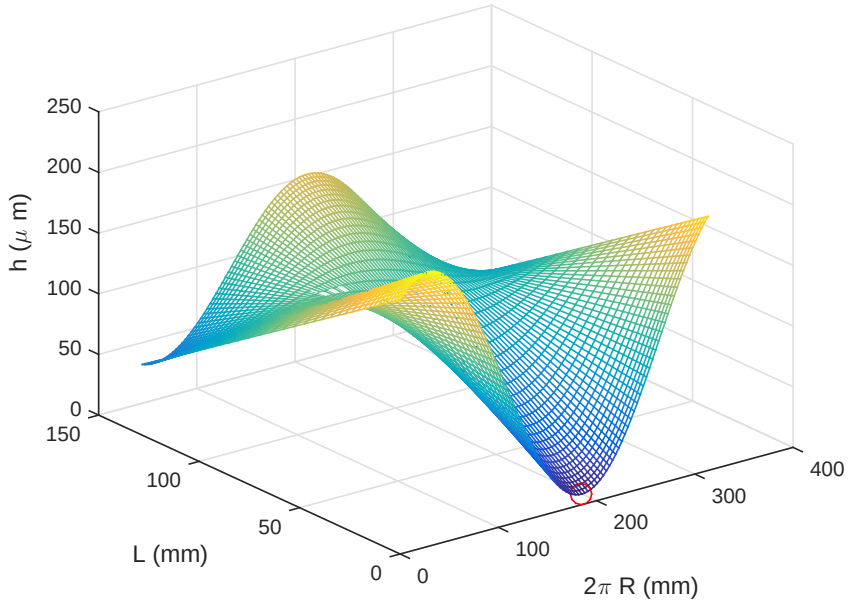

Figure 4.6. The fluid film thickness behaviour at the equilibrium position of the inverse problem for $\mathbf{F} = (0, 0, 3000\ \text{N})$ and $\boldsymbol{\tau} = (0, 70\ \text{N m}, 0)$. The minimum value is 8.77 µm, represented in the figure by a circular marker. It is located at $x = 0$ mm, $\theta = 3.7070$ rad ($\theta R = 184.9462$ mm).

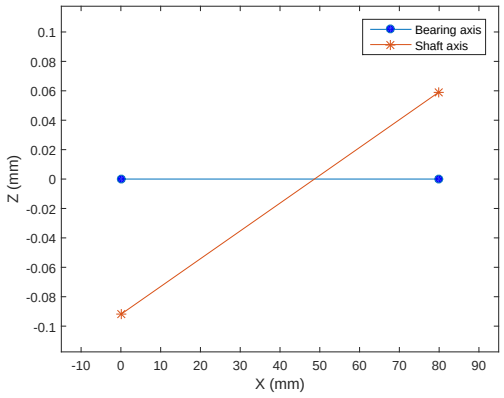

(a) Misalignment in the *xz*-plane with the Elrod–Adams cavitation model.

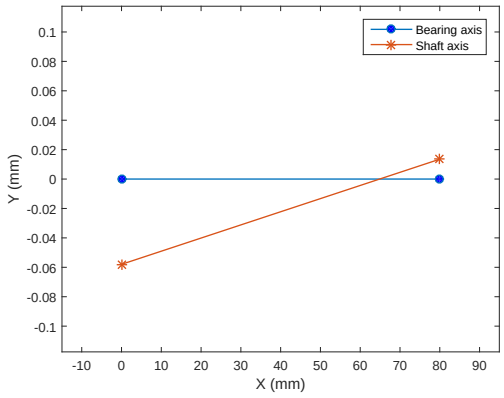

(b) Misalignment in the *xy*-plane with the Elrod–Adams cavitation model.

Figure 4.7. View of the misalignment in both *xz*-plane and *xy*-plane when solving the inverse problem with the Elrod–Adams cavitation model for $\mathbf{F} = (0, 0, 3000\ \text{N})$ and $\boldsymbol{\tau} = (0, 70\ \text{N m}, 0)$.

In Fig. 4.8 different pressure contour maps are presented. They show the behaviour of the solution of the direct problem (for $\bar{\rho} = 0.5$, $\alpha = 215°$, $\varphi = 0.001°$, $\beta = 0.001°$) with respect to the penalization parameter ϵ, when it tends to zero. The values chosen for the experiment are: ϵ = 5e-9, ϵ = 5e-10, ϵ = 5e-11, ϵ = 5e-12. The stability of the pressure contour map pattern should be noticed when ϵ decreases up to three orders of

magnitude. However, cavitation regions appear at different locations, as expected, since they are directly governed by the ϵ parameter.

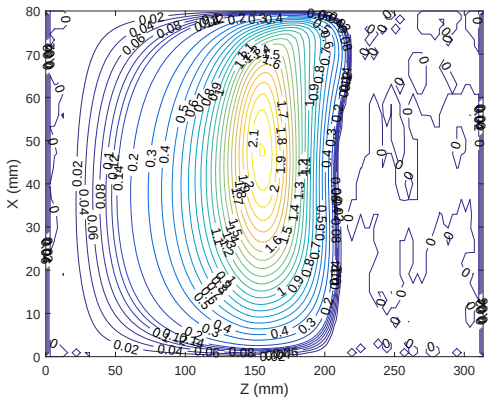

(a) Pressure contour map for ϵ = 5e-9.

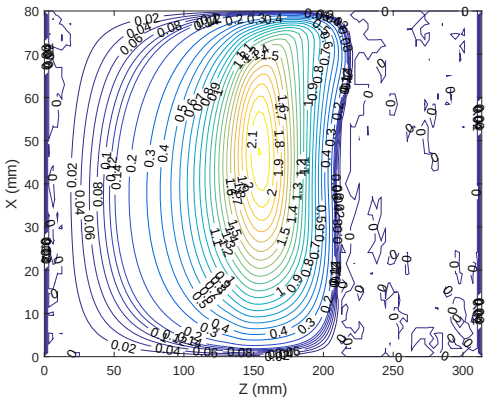

(b) Pressure contour map for ϵ = 5e-10.

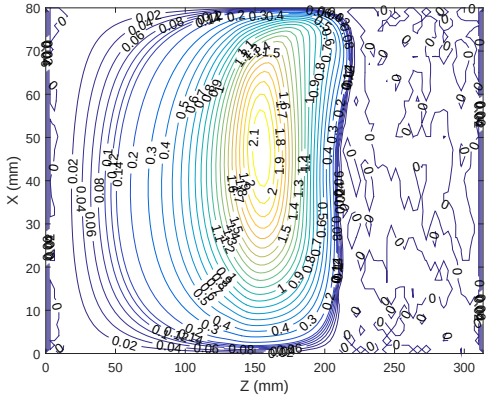

(c) Pressure contour map for ϵ = 5e-11.

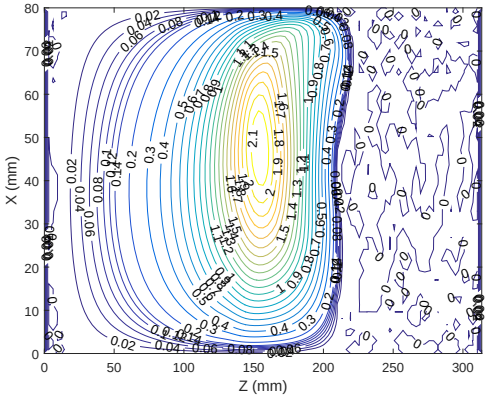

(d) Pressure contour map for ϵ = 5e-12.

Figure 4.8. Pressure contour maps for different values of the penalization parameter ϵ.

Finally, in Fig. 4.9 we show the behaviour of the force exerted by the lubricant pressure $|\mathbf{F}_{\mathrm{L}}|$ with respect to the shaft angular velocity ω. The experiment was accomplished for $\bar{\rho} = 0.5$, $\alpha = 215°$, $\varphi = 0.001°$, $\beta = 0.001°$ and different ω values: $\{1000, 1500, 2000, 2500, 3000, 3500, 4000\}$ rpm. It proves the continuous dependence of the $|\mathbf{F}_{\mathrm{L}}|$ generated by the lubricant on the shaft angular velocity.

It is important to remark that, a comparison between the proposed metaheuristic with other classical optimization algorithms used by other authors is a difficult task when it comes to choose a proper criterion to compare. At first glance, one may think it must be done based on CPU time. This choice makes the comparison of different algorithms complicated, as the CPU time depends significantly on the programming

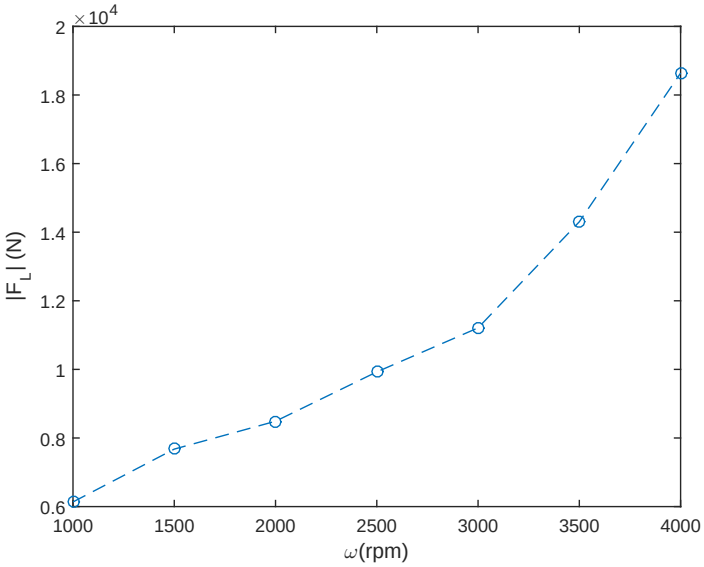

Figure 4.9. The behaviour of $|\mathbf{F}_{\mathrm{L}}|$ with respect to ω.

language used, the compiler, the expertise of the programmer, and the computer used for running the experiments. In fact, it is recommended to implement all the algorithms used in the comparison in order to make it fair. Even so, a fully fair comparison is not guaranteed since it is difficult to ensure that the same amount of effort is put to optimize the code of all the implemented algorithms.

Notice that, in our case, the direct problem is a large scale problem whose solution is a time-consuming task. Then, the number of evaluations of the direct problem to achieve a desired solution quality of the inverse problem, seems to be a good candidate criterion of comparison. Since the gradient of the residual E is not explicitly available, at each step, classical optimization algorithms need to approximate it, by finite differences, for example. Thus, it is ensured several calls to the direct problem during the whole optimization routine, not to mention the calls in the residual itself. Moreover, in $\mathrm{ACO}_{\mathbb{R}}$ at each iteration, several ants solve the direct problem from a probabilistically generated vector solution, to compute their associated cost function. This criterion is insensitive to the programming language, to the compiler and to the characteristics of the computer. The disadvantage is that it does not take into account the time-complexity of the algorithms compared. In addition, $\mathrm{ACO}_{\mathbb{R}}$ is an inherently parallel algorithm; condition that – when exploited – hides the true performance of the metaheuristic, if such comparison criterion is considered. We plan to study a proper criterion for accomplishing a comparison between these kinds of algorithms in future work.

4.3.1 Behaviour of ρ with respect to $|\mathbf{F}_L|$ for the parallel case

In Fig. 4.10 we show the behaviour of ρ with respect to $|\mathbf{F}_L|$ at the equilibrium positions, illustrating how the eccentricity approaches to C when increasing the applied load. The simulation is taken applying the forces at the centre of mass, recreating the parallel case, when both φ and β are equal zero.

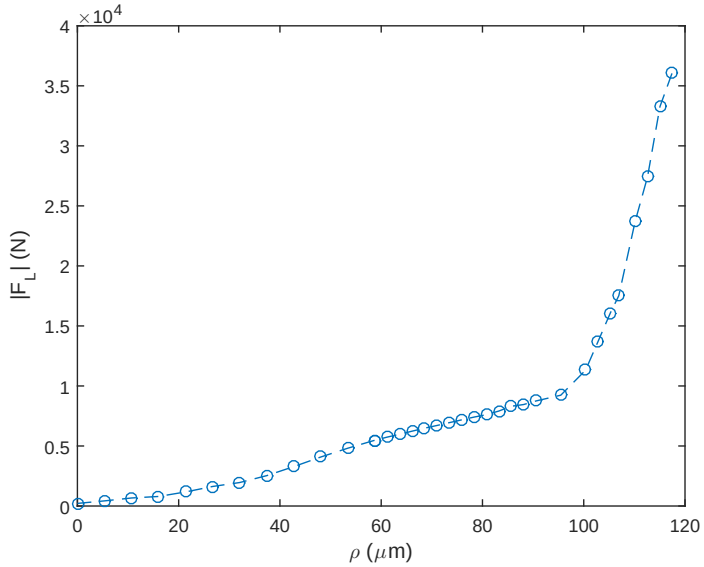

Figure 4.10. The behaviour of ρ with respect to $|\mathbf{F}_L|$.

It should be noticed that $|\mathbf{F}_L|$ is a monotone increasing function, which numerically indicates uniqueness. These results match those observed in (Álvarez and Oujja, 2011). For the parallel case, we also noted that the solution holds under the effect of rotation, i.e., if $(p(\rho,\alpha),h(\rho,\alpha))$ is a solution, then $(p(\rho,\alpha+\theta),h(\rho,\alpha+\theta))$ is also a solution.

4.3.2 Grid convergence study

In this section we conduct a convergence study as in Sect. 3.4.1 to verify the calculations for the direct problem with the Elrod–Adams cavitation model. We follow the procedure as suggested in (Roache, 1994; Roache, 2002). Since the exact force exerted by the fluid pressure is unknown we perform as well three computations of forces, on a different grid each, and compute two GCIs, from fine grid to intermediate (GCI_{12}) and from intermediate to coarse grid (GCI_{23}). Thus, we know how much the computed force will change with an additional refinement of the grid (Roache, 1998). A small value is preferable, since it

suggests the force is within the asymptotic range. The grid information for the convergence study is provided in Table 4.3.

Table 4.3. Grid information for the convergence study.

No	Grid elements	Force ID	Force value (N)
1	400×160	F_1	7.67609×10^3
2	200×80	F_2	7.45791×10^3
3	100×40	F_3	7.37293×10^3

It includes, for each experiment, the corresponding force value for the direct problem, computed for $\alpha = 3.665192$ rad, $\rho = 58.75$ µm, $\beta = 0.000017$ rad and $\varphi = 0.000017$ rad. The geometrical and physical constants used are those in Table 4.2.

We determine the order of convergence c_s according to the force values. As we use in the convergence study a constant refinement ratio $r_t = 2$, we can perform a direct evaluation of c_s by Eq. (4.3.1); see (Roache, 1994) for details:

$$c_s = \ln\left(\frac{F_3 - F_2}{F_2 - F_1}\right) / \ln r_t, \tag{4.3.1}$$

$$c_s = \ln\left(\frac{7.37293 \times 10^3 \text{ N} - 7.45791 \times 10^3 \text{ N}}{7.45791 \times 10^3 \text{ N} - 7.67609 \times 10^3 \text{ N}}\right) / \ln 2,$$

$$c_s = -1.3603.$$

The GCI for the fine grid solution is then computed. It is defined as:

$$GCI_{jk} = \frac{f_s}{({r_t}^{c_s} - 1)} \left|\frac{F_j - F_k}{F_j}\right|,$$

where f_s is a factor of safety, recommended to be $f_s = 1.25$ for comparisons of three grids; see (Roache, 1998) for details. The GCI for grids 1 and 2 is:

$$GCI_{12} = \frac{1.25}{(2^{-1.3603} - 1)} \left|\frac{7.67609 \times 10^3 \text{ N} - 7.45791 \times 10^3 \text{ N}}{7.67609 \times 10^3 \text{ N}}\right|,$$

$$GCI_{12} = -0.0582.$$

Similarly, the GCI for grids 2 and 3 is:

$$GCI_{23} = \frac{1.25}{(2^{-1.3603} - 1)} \left| \frac{7.45791 \times 10^3 \text{ N} - 7.37293 \times 10^3 \text{ N}}{7.45791 \times 10^3 \text{ N}} \right|,$$
$$GCI_{23} = -0.0233.$$

We then check that these solutions are within the asymptotic range of convergence by Eq. (4.3.2):

$$GCI_{23} = r_t^{c_s} GCI_{12}, \tag{4.3.2}$$
$$\frac{-0.0233}{2^{-1.3603} - 0.0582} = 1.0293,$$

which is approximately 1 and indicates that the test succeeded. Based on this study we can also estimate the exact solution F_e by the Richardson extrapolation, using Eq. (4.3.3); see (Roache, 1994) for details:

$$F_e \approxeq F_1 + \frac{F_1 - F_2}{r_t^{c_s} - 1}, \tag{4.3.3}$$
$$F_e \approxeq 7.67609 \times 10^3 \text{ N} + \frac{7.67609 \times 10^3 \text{ N} - 7.45791 \times 10^3 \text{ N}}{2^{-1.3603} - 1},$$
$$F_e \approxeq 7.3187 \times 10^3 \text{ N}.$$

Finally, we could say that the force exerted by the fluid pressure, for the direct problem depicted, is estimated to be 7.3187×10^3 N with an error band of 0.0582.

4.3.3 Validation

We compare the predicted pressure values in the bearing mid-plane, to published experimental data, to validate the whole numerical approach with the Elrod–Adams cavitation model; see Fig. 4.11. For that, the work of Bouyer and Fillon (2002) was used, where the same geometrical and physical constants of the journal bearing were considered. Specifically, we compare our numerical results, after solving the corresponding inverse problem, with the experimental data referred in Fig. 6 of (ibid., p. 315). The experiment is accomplished for a misalignment of 70 N m, an external radial force of 3000 N and a shaft angular velocity of 2000 rpm.

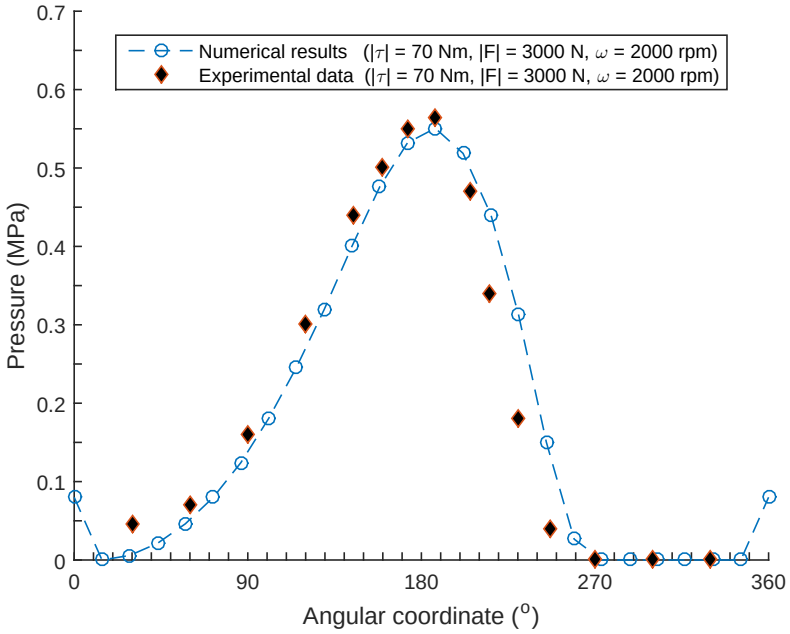

Figure 4.11. Validation of the whole numerical approach with the Elrod–Adams model, comparing the predicted pressure in the bearing mid-plane to experimental data ($|\boldsymbol{\tau}|$=70 N m, $|\mathbf{F}|$=3000 N, ω=2000 rpm).

Comparison between the experimental and the numerical results shows small discrepancies. Again, the differences can be related to the fact that not all the surrounding phenomena (as temperature) are considered in our numerical model. However, the experiment shows an acceptable agreement between the output of our model and the experimental data. Such differences do not influence the determination of the maximum pressure (discrepancy of 0.014276 MPa), which is an essential factor when designing a journal bearing. Thus, the algorithm could be used as a first prediction of the final position of a journal bearing under an imposed radial loading, considering misalignment and the Elrod–Adams cavitation model.

Conclusions

As a major conclusion, based on the results of this dissertation, we draw that our computational algorithm is suitable to determine the shaft position and the pressure distribution in a misaligned journal bearing with radial loading, as a first prediction of contact and cavitation. So, our hypothesis could be verified for both Reynolds and Elrod–Adams cavitation models. Despite we did not include in the analysis other realistic factors, the comparisons between the experimental and numerical results showed small discrepancies that do not influence the determination of the maximum pressure, an essential factor when designing a journal bearing.

Additionally, for the Reynolds cavitation model, it is suitable to tackle the direct problem by minimizing a convex functional using a PCG with both projection and restarting strategies. To address the inverse problem, it is possible to pose a system of non-linear equations and then solving it, in least squares sense, by a trust-region numerical approach. In this context, it provides another way of solution, different from the ones that exist in the literature. Equally important, the numerical simulations showed the existence of contact points for finite loading when misalignment occurs. A mathematical proof was provided in Sect. 3.1 to demonstrate the finite load capacity of the system for the point contact case. Nevertheless, the uniform boundedness of the pressure is not guaranteed. The results also showed the continuous dependence of the maximum load capacity of the bearing on the shaft angular velocity, in such a way that it increases with the latter.

When considering the Elrod–Adams cavitation model, it is possible to find a numerical solution to the direct problem, by minimizing the convex functional proposed in Eq. (4.1.19). Then, it is possible to address the inverse problem related by first posing a system of non-linear equations and then solving it, in least squares sense, through the metaheuristic $ACO_{\mathbb{R}}$. In this context, it provides also another way of solution,

different to the ones existing at this point. The numerical simulations show that the force exerted by the pressure depends continuously on the shaft angular velocity as well. We also noted that, as $|\mathbf{F}|$ increases, the eccentricity increases in a continuous and monotone way as far as the model is valid (i.e. for experimental values $|1 - \bar{\rho}| > 10\text{e-}3$).

Future work

Throughout this dissertation we have developed two different approaches to solve the inverse problem in a misaligned journal bearing with the Reynolds and the Elrod–Adams cavitation model respectively. Despite the encouraging results there are still some improvements that can be added to the present study in order to capture the reality observed in practice. However, to couple most of the improvements is required a large numerical effort.

For instance, a thermal problem must be solved in the lubricant for large values of the eccentricity. Under this circumstance, the energy dissipation by viscous effects is limited to the zone of the fluid film minimum thickness and, in consequence, large variations of temperature may occur along the fluid film. By solving the thermal problem we could obtain the correct values of the lubricant viscosity to be used in the hydrodynamic problem. Besides, if the lubricant viscosity depends on the pressure (piezoviscous regime) we need to introduce the Barus law, as a viscosity-pressure relation.

On the other hand, if high pressure values can deform the surfaces in contact, an elastohydrodynamic regime must be considered, including a pressure gap relation. The Hertz equation should be taken into account to address elastic deformations. Similarly, non-Newtonian fluids must be considered in the analysis since real lubricants have shown that the stress is not directly proportional to the shear strain and in addition can contain additives. This is a wide field of interest in the mechanical literature.

Moreover, if operating conditions become really strong, in a way that the lubricant minimum thickness tends to be small as the order of magnitude of the roughness, the effect of the surface roughness on the behaviour of the lubricant film comes into play. In fact, it is of interest to study the effect of deterministic periodical pattern of roughness for which a mathematical theory is available (homogenization theory).

To consider all these factors (among others), they are plugged into the RE. A wide set of non-linear

equations appears which usually demands a large numerical effort. We plan to consider them in future work, as well as finding a proper criterion to compare quantitatively our proposed metaheuristic with other classical optimization algorithms.

Glossary

abrasive wear A wear caused by the loss of material due to hard particles or hard protuberances that are forced against and move along a solid surface. 2, 74

adhesive wear The result of adhesion between contacting bodies. 2, 74

cavitation wear A wear caused by fast flowing liquids. 2

corrosive wear A wear caused by the fluid material formed by chemical attack of either contacting body. 2

diffusive wear A wear caused at high interface temperatures. 2

erosive wear A wear caused by the impact of particles of solid or liquid against the surface of an object. The impacting particles gradually remove material from the surface through repeated deformations and cutting actions. 2, 74

fatigue wear A milder forms of wear often initiated by fatigue processes due to repetitive stresses under either sliding or rolling. 2

fretting wear A wear caused when the amplitude of movement between contacting bodies is restricted to few micrometres and the film material is trapped within the contact and may eventually become destructive. 2

impact wear A wear caused by impact between two solids. 2

melting wear A wear caused when the contact loads and speeds are sufficiently high to allow for the surface layers of the solid to melt. 2

NP-hard The class of problem for which it is strongly believed that it is not possible to find efficient (i.e., polynomial time) algorithms to solve them optimally. 21

OpenMP An application programming interface (API) for shared-memory parallel programming. 23, 98

oxidative wear A wear caused by atmospheric oxygen as the corroding agent. 2

Acronyms

ACO Ant Colony Optimization. xi, 21, 23, 94–97

ACO$_{\mathbb{R}}$ Ant Colony Optimization for continuous domain. xxi, 6, 7, 23, 25, 87, 94–100, 106, 111

ASME American Society of Mechanical Engineers. 3

CG Conjugate Gradient Method. 69

DACO$_{\mathbb{R}}$ Alternative Ant Colony Optimization for continuous domain. 23

EHL Elastohydrodynamic Lubrication. 15

FDM Finite Difference Method. 18

FEM Finite Element Method. 17–19, 87

FVM Finite Volume Method. 19

GCI Grid Convergence Index. 82, 83, 107, 108

GRE Generalized Reynolds Equation. 27, 44, 48, 49, 51, 52

IACO$_{\mathbb{R}}$-LS Incremental Ant Colony Optimization with Local Search for continuous domain. 23

L-BFGS Limited-Memory Broyden Fletcher Goldfarb Shanno. 87, 93, 98

l.s.c lower semi continuous. xi, 6, 21, 92

MC Method of Characteristics. 19, 21, 87

PCG Preconditioned Conjugate Gradient Method. xvii, 7, 19, 59, 64, 66–69, 73, 74, 111

PDE Partial Differential Equations. 19

PDF probabilistic density function. 96

RE Reynolds Equation. 2–4, 10–12, 17–20, 27, 34, 41, 42, 50, 56, 70, 113

THL Thermohydrodynamic Lubrication. 15

TSP Traveling Salesman Problem. 21

UACO$_{\mathbb{R}}$ Unified Ant Colony Optimization for continuous domain. 23

VAMAS Versailles Project on Advanced Materials and Standards. 2

List of symbols

Symbol	Description	Unit
Γ_2	Front and back boundaries at the active region	dimensionless
Ω^+	Active zone or lubricated region	mm^2
α	Shaft angular coordinate	rad
Φ	Bearing angular coordinate	rad
γ	Angular position at plane X = x	rad
$\mathcal{P}_{ij}^{k}$	The transition probability from city i to city j for the k^{th} ant	dimensionless
$\mathcal{T}_{ij}(t)$	Trail intensity on edge (i, j)	dimensionless
η_{ij}	The ant visibility in the ACO algorithm	dimensionless
k	Artificial time step	dimensionless
$\boldsymbol{\upsilon}$	An artificial velocity field	dimensionless
p_a	Atmospheric pressure	MPa
δ	Meshing attenuation factor	dimensionless
$x^{'}$	Auxiliary coordinate for x	mm
$y^{'}$	Auxiliary coordinate for y	mm
$z^{'}$	Auxiliary coordinate for z	mm
$\bar{\gamma}$	Normalized angular position at plane X = $\bar{x}$	dimensionless
$\bar{\Omega}$	Normalized domain	dimensionless
$\bar{F}_y$	Normalized F_y component	dimensionless
$\bar{F}_z$	Normalized F_z component	dimensionless
$\bar{h}$	Normalized film thickness	dimensionless
$\bar{\lambda}$	Normalized λ	dimensionless
$\bar{p}$	Normalized fluid pressure	dimensionless

Symbol	Description	Unit
$\bar{\rho}$	Normalized shaft eccentricity	mm
$\bar{\phi}$	Normalized test function	dimensionless
$\bar{\tau}_y$	Normalized τ_y component	dimensionless
$\bar{\tau}_z$	Normalized τ_z component	dimensionless
$\overline{W}$	Normalized W	dimensionless
$\bar{\mu}$	Normalized fluid viscosity	Pa s
$\bar{x}$	Normalized axial coordinate	dimensionless
$\bar{z}$	Normalized z	dimensionless
$\bar{p}_s$	Atmospheric pressure	MPa
C	Radial clearance	μm
Γ_1	Front and back boundaries at the cavitation region	dimensionless
Ω^0	Cavitated region	mm^2
ϑ	Lubricant concentration	dimensionless
$\kappa(A)$	Condition number of a matrix A	dimensionless
ζ_j	Correction parameter at iteration j after the restarting procedure in the PCG	dimensionless
D	Bearing diameter	mm
ξ_j	Deflection parameter at iteration j for the PCG	dimensionless
ϱ	Fluid density	$kg\,m^{-3}$
ϑ_j	Discrete concentration value at node j	dimensionless
ϕ_j	Discrete pressure value at node j	MPa
$\mathbf{r}$	Displacement vector from the rotation axis to the point where $\mathbf{F}_q$ is applied	mm
m	Division number along the axial direction	dimensionless
Ω	Domain	mm^2
ξ	Speed of convergence in the $ACO_{\mathbb{R}}$	dimensionless
Σ	Free boundary between Ω^+ and Ω^0	dimensionless
p_s	Atmospheric pressure	MPa
$\mathbf{F}$	External force vector	N m
$\mathbf{F}_L$	Force vector exerted by the lubricant	N m
$\mathbf{F}_q$	Force exerted by the fluid pressure at point $\mathbf{q}$	N
F_y	External force component in the y direction	N

Symbol	Description	Unit
F_z	External force component in the z direction	N
$\mathbf{g}$	Gravity vector	$\mathrm{mm\,s^{-2}}$
g	Gaussian function	dimensionless
G^i	Gaussian kernel	dimensionless
$\mathcal{P}_k$	The probability of choosing the $\mathrm{k^{th}}$ Gaussian function	dimensionless
w_k	Associated weight for the solution k in the $\mathrm{ACO}_{\mathbb{R}}$ algorithm	dimensionless
GCI_{ij}	Grid Convergence Index computed between grids i and j	dimensionless
g	Scalar value for gravity	$\mathrm{mm\,s^{-2}}$
h	Film thickness	μm
H_ϵ	Approximation for the Heaviside function	dimensionless
H	Heaviside function	dimensionless
n_a	Number of ants in the solution archive for the $\mathrm{ACO}_{\mathbb{R}}$ algorithm	dimensionless
L	Journal bearing length	mm
Λ	A parameter grouping the viscosity integrals in the Elrod–Adams model	dimensionless
λ	Eccentricity respect to the global coordinate system	μm
S_y	Component of λ along the (y) direction	mm
S_z	Component of λ along the (z) direction	mm
μ	Mean for the Gaussian kernel G^i	dimensionless
ψ	Misalignment angle	rad
φ	Projection of ψ on the xy-plane	rad
β	Projection of ψ on the xz-plane	rad
m_k	Quadratic model function for the trust-region approach	dimensionless
n	Total number of nodes for the mesh discretization	dimensionless
n_s	Number of new ants probabilistically generated in the $\mathrm{ACO}_{\mathbb{R}}$ algorithm	dimensionless
ν	Eccentricity respect to the auxiliary coordinate system	μm
$\mathbf{n}$	Unit normal vector to Σ	dimensionless
$\mathbf{i}$	Exterior normal unit vector of Ω^0	dimensionless
O_b	Bearing centre	mm
B	The object depth in Fig. 2.3	mm
$\tilde{H}$	Largest distance between the surface and the object in Fig. 2.3	mm

Symbol	Description	Unit
O_j	Shaft centre	mm
ω	Shaft angular velocity	rpm
c_s	Order of convergence in the grid convergence study	dimensionless
O	Origin of coordinate	dimensionless
p	Fluid pressure	MPa
p_c	Cavitation pressure	MPa
ϵ	Penalty parameter in the Heaviside approximation	dimensionless
ϖ	Coefficient related to the evaporation of trail	dimensionless
x_k	Current iterate for the trust-region approach	dimensionless
$\mathbf{q}$	Arbitrary position vector on the bearing surface	mm
Ψ	Lower triangular matrix	dimensionless
M	Preconditioning matrix	dimensionless
q	Locality of the search process in the $ACO_{\mathbb{R}}$ algorithm	dimensionless
q_x	Flow rate in the x direction	$mm^3\ s^{-1}$
q_y	Flow rate in the y direction	$mm^3\ s^{-1}$
R	Shaft radius	mm
Δ_k	Trust-region radius	dimensionless
R_b	Bearing radius	mm
r_t	Refinement ratio in the grid convergence study	dimensionless
μ_0	Reference viscosity	Pa s
r_j	Residual at iteration j defined for the PCG	MPa
E	Residual for the inverse problem	dimensionless
ς	Restart iteration for the PCG	dimensionless
Γ_0	Supply groove	dimensionless
d_j	Search direction at iteration j for the PCG	mm
ρ	Shaft eccentricity	mm
N_j	Shape function for the FEM evaluated at node j	dimensionless
A_n	Solution archive for the $ACO_{\mathbb{R}}$	dimensionless
s	Solution to the system of linear equation in the preconditioning approach	MPa
σ	Standard deviation for the Gaussian kernel G^i	dimensionless

Symbol	Description	Unit
ε_j	Step length for the PCG	mm
s_k	Solution step for the minimization of the residual E	dimensionless
t	Time	s
T_c	Characteristic time	s
ϕ	Test function	MPa
K	Space of test functions for the Reynolds cavitation model	dimensionless
$\mathcal{K}$	Space of test functions for the Elrod–Adams cavitation model	dimensionless
θ	Circumferential coordinate	rad
$\tilde{\gamma}$	Transformed γ	rad
$\tilde{\Omega}$	Transformed normalized domain	dimensionless
$\tilde{h}$	Transformed $\bar{h}$	dimensionless
$\tilde{\lambda}$	Transformed $\bar{\lambda}$	dimensionless
$\tilde{x}$	Transformed $\bar{x}$	dimensionless
$\boldsymbol{\tau}$	External torque vector	N m
τ_y	External torque component in the y direction	N m
τ_z	External torque component in the z direction	N m
u	Fluid velocity component along the x coordinate	mm s^{-1}
U_c	Velocity variation in the x component	mm s^{-1}
v	Fluid velocity component along the y coordinate	mm s^{-1}
V_c	Velocity variation in the y component	mm s^{-1}
$\mathbf{u}$	Fluid velocity vector	mm s^{-1}
$\mathbf{v}$	Object velocity vector	mm s^{-1}
U	Object velocity component along the x coordinate	mm s^{-1}
V	Object velocity component along the y coordinate	mm s^{-1}
W	Object velocity component along the z coordinate	mm s^{-1}
$\mathbf{w}$	Relative velocity vector between the fluid and the object	mm s^{-1}
μ	Fluid viscosity	Pa s
w	Fluid velocity component along the z coordinate	mm s^{-1}
W_c	Velocity variation in the z component	mm s^{-1}
x	Cartesian coordinate	mm

Symbol	Description	Unit
y	Cartesian coordinate	mm
z	Cartesian coordinate	mm

References

Abass, B. A. and M. M. Sahib (2013). "Effect of Bearing Compliance on Thermo-hydrodynamic Lubrication of High Speed Misaligned Journal Bearing Lubricated with Bubbly Oil". In: *Ind. Eng. Lett* 3, pp. 48–60 (cit. on p. 24).

Adams, D. R. (1991). "Design and Analysis: A Perspective for the Future". In: *Vehicle Tribology: Proceedings of the 17th Leeds-Lyon Symposium on Tribology Held at the Institute of Tribology, Leeds University, Leeds, UK, 4th-7th September 1990*. Vol. 18. Elsevier, pp. 7–18 (cit. on p. 13).

Álvarez, S. J. (1986). "Problemas de frontera libre en teoría de lubrificación". PhD thesis. Universidad Complutense de Madrid (cit. on p. 18).

Álvarez, S. J. and R. Oujja (2003). "On the uniqueness of the solution of an evolution free boundary problem in theory of lubrication". In: *Nonlinear Anal-Theor* 54.5, pp. 845–872 (cit. on p. 93).

— (2011). "On the uniqueness of solution in a lubricated device with imposed load". In: *Proceedings of the 4th International Conference on Approximation Methods and Numerical Modelling in Environment and Natural Resources (MAMERN'11)*. (May 23, 2011). Ed. by B. Amaziane, D. Barrera, et al. Saïdia, Morocco: Universidad de Granada, pp. 95–99 (cit. on p. 107).

Arregui, I., J. J. Cendán, and C. Vázquez (2002). "Mathematical analysis and numerical simulation of a Reynolds-Koiter model for the elastohydrodynamic journal-bearing device". In: *ESAIM-Math. Model. Num.* 36.2, pp. 325–343 (cit. on p. 14).

Asanabe, S., M. Akakoski, and R. Asai (1971). "Theoretical and experimental investigation on misaligned journal bearing performance". In: *Industrial lubrication and tribology*. Vol. 23. 6, p. 208 (cit. on pp. 17, 78).

Bayada, G. and M. Chambat (1986a). "Sur quelques modélizations de la zone de cavitation en lubrification hydrodynamique". In: *J. Theor. and Appl. Mech.* 5.5, pp. 703–729 (cit. on pp. 18, 19).

— (1986b). "The transition between the Stokes equation and the Reynolds equation: A mathematical proof." In: *Appl. Math. Opt.* 14.1, pp. 73–93 (cit. on pp. 10, 18).

Bayada, G., M. Chambat, and C. Vázquez (1998). "Characteristics method for the formulation and computation of a free boundary cavitation problem". In: *J. Comput. Appl. Math.* 98.2, pp. 191–212 (cit. on p. 19).

Bayada, G., S. Martin, and C. Vázquez (2005a). "An average flow model of the Reynolds roughness including a mass-flow preserving cavitation model". In: *J. Tribol-T. ASME.* 127.4, pp. 793–802 (cit. on p. 24).

— (2005b). "Homogenization of a nonlocal elastohydrodynamic lubrication problem: a new free boundary model". In: *Math. Mod. Meth. Appl. S.* 15.12, pp. 1923–1956 (cit. on p. 24).

— (2005c). "Homogneisation du modle d'Elrod-Adams hydrodynamique". In: *Asymptotic. Anal.* 44, pp. 75–110 (cit. on p. 24).

— (2005d). "Two-scale homogenization of a hydrodynamic Elrod-Adams model". In: *Asymptotic. Anal.* (Cit. on p. 24).

— (2006). "Micro-roughness effects in (elasto) hydrodynamic lubrication including a mass-flow preserving cavitation model". In: *Tribol. Int.* 39.12, pp. 1707–1718 (cit. on p. 24).

Bayada, G. and C. Vázquez (2007). "A survey on mathematical aspects of lubrication problems". In: *Boletín SeMA* 39, pp. 37–74 (cit. on p. 18).

Bazaraa, M. S., H. D. Sherali, and C. M. Shetty (2006). *Nonlinear Programming. Theory and Algorithms*. John Wiley & Sons, Inc (cit. on pp. 64, 65, 69).

Bermúdez, A. and J. Durany (1989). "Numerical Solution of Cavitation Problems in Lubrication". In: vol. 75, pp. 455–466 (cit. on p. 19).

Bermúdez, A. and C. Moreno (1981). "Duality Methods for Solving Variational Inequalities". In: *Comp. Math. with Appls.* 7, pp. 43–58 (cit. on pp. 20, 90).

Blum, C., P. Cardoso, and F. Herrera (2009). "ACO$_{\mathbb{R}}$ híbrido con múltiples colonias para problemas de optimización continua". In: *VI Congreso Español sobre Metaheurísticas, Algoritmos Evolutivos y Bioinspirados (MAEB'09)* (cit. on p. 96).

Blum, C., M. Y. Vallès, and M. J. Blesa (2008). "An ant colony optimization algorithm for DNA sequencing by hybridization". In: *Computers & Operations Research* 35.11, pp. 3620–3635 (cit. on p. 22).

Boedo, S. and J. F. Booker (2004). "Classical bearing misalignment and edge loading: a numerical study of limiting cases". In: *J. Tribol-T. ASME.* 126.3, pp. 535–541 (cit. on pp. 3, 17, 61–63).

Boucherit, H., M. Lahmar, and B. Bou-Said (2008). "Misalignment effects on steady-state and dynamic behaviour of compliant journal bearings lubricated with couple stress fluids". In: *Lubr. Sci.* 20.3, pp. 241–268 (cit. on p. 24).

Bouyer, J. and M. Fillon (2002). "An experimental analysis of misalignment effects on hydrodynamic plain journal bearing performances". In: *J. Tribol.* 124.2, pp. 313–319 (cit. on pp. 16, 74, 85, 100, 109).

— (2003). "Improvement of the THD performance of a misaligned plain journal bearing". In: *J. Tribol.* 125.2, pp. 334–342 (cit. on p. 24).

Brézis, H. (1984). *Análisis funcional*. Alianza Editorial (cit. on p. 92).

Brito, F. P. (2009). "Thermohydrodynamic performance of twin groove journal bearings considering realistic lubricant supply conditions: a theoretical and experimental study". PhD thesis. Universidade do Minho (cit. on p. 50).

Calvo, N., J. Durany, and C. Vázquez (1997). "Comparación de algoritmos numéricos en problemas de lubricación hidrodinámica con cavitación en dimensión uno". In: *Rev. Int. Metod. Numer.* 13.2, pp. 185–209 (cit. on pp. 19, 20, 66, 88, 90).

Capriz, G. and G. Cimatti (1983). "Free boundary problems in the theory of hydrodynamic lubrication: A survey". In: *Free boundary problems: theory and applications*. Ed. by A. Fasano and M. Primicerio. Vol. 2. Research Notes in Mathematics 79. Pitman, pp. 613–635 (cit. on p. 18).

Chelouah, Rachid and Patrick Siarry (1999). "Enhanced continuous tabu search: An algorithm for optimizing multiminima functions". In: *Meta-Heuristics. Advances and Trends in Local Search Paradigms for Optimization*. Springer. Chap. 4, pp. 49–61 (cit. on p. 23).

Chelouah, Rachid and Patrick Siarry (2000). "A continuous genetic algorithm designed for the global optimization of multimodal functions". In: *Journal of Heuristics* 6.2, pp. 191–213 (cit. on p. 23).

Christopherson, D. G. (1941). "A new mathematical method for the solution of film lubrication problems". In: *Inst. Mech. Engrs. J. Proc.* 146, pp. 126–135 (cit. on pp. 12, 18).

Cimatti, G. (1984). "On certain nonlinear problems arising in the theory of lubrication". In: *Appl. Math. Opt.* 11.1, pp. 227–245 (cit. on p. 18).

— (1986). "Existence and uniqueness for nonlinear Reynolds equations". In: *Int. J. Eng. Sci.* 24.5, pp. 827–834 (cit. on p. 18).

Ciuperca, I. S., I. Hafidi, and M. Jai (2006). "Singular perturbation problem for the incompressible Reynolds equation". In: *Electr. J. Differ. Equ.* 2006.83, pp. 1–19 (cit. on pp. 20, 59).

Ciuperca, I. S., M. Jai, and J. I. Tello (2009). "On the existence of solutions of equilibria in lubricated journal bearings". In: *SIAM J. Math. Anal.* 40.6, pp. 2316–2327 (cit. on pp. 17, 20, 59).

— (2017). "Equilibrium analysis for a mass-conserving model in presence of cavitation". In: *Nonlinear Analysis: Real World Applications* 35, pp. 250–264 (cit. on pp. 4, 21).

Ciuperca, I. S. and J. I. Tello (2011a). "Lack of contact in a lubricated system". In: *Q. Appl. Math.* 69.2, pp. 357–378 (cit. on p. 21).

— (2011b). "On a variational inequality on elasto-hydrodynamic lubrication". In: *J. Math. Anal. Appl.* 383.2, pp. 597–607 (cit. on p. 21).

Coleman, T. F. and Y. Li (1996). "An interior trust region approach for nonlinear minimization subject to bounds". In: *SIAM Journal on Optimization* 6, pp. 418–445 (cit. on pp. 71–73).

Conte, S.D. and C.W. De Boor (1980). *Elementary Numerical Analysis: An Algorithmic Approach*. McGraw-Hill Book Company. Chap. 7, p. 294 (cit. on p. 90).

Cryer, C. W. (1971). "The method of Christopherson for solving free boundary problems for infinite journal bearings by means of finite differences". In: *Math. Comput.* 25.115, pp. 435–443 (cit. on p. 18).

Cuvelier, C. (1979). "A free boundary problem in hydrodynamic lubrication including surface tension". In: *Sixth International Conference on Numerical Methods in Fluid Dynamics*. Ed. by H. Cabannes, M. Holt, and V. Rusanov. Lecture Notes in Physics 90. Springer-Verlag, Berlin, Heidelberg, pp. 143–148 (cit. on pp. 18, 19).

Das, S., S. K. Guha, and A. K. Chattopadhyay (2002). "On the steady-state performance of misaligned hydrodynamic journal bearings lubricated with micropolar fluids". In: *Tribol. Int.* 35.4, pp. 201–210 (cit. on p. 24).

Díaz, J. I. and J. I. Tello (2004). "A note on some inverse problems arising in lubrication theory". In: *Differ. Integral. Equ.* 17, pp. 583–592 (cit. on p. 20).

Díaz, M., H. Lombera, et al. (2015). "An Approach for Assembly Sequence Planning Based on Max-Min Ant System". In: *IEEE Latin America Transactions* 13.4, pp. 907–912 (cit. on p. 22).

Dorigo, M (1992). "Optimization, learning and natural algorithms". Italian. PhD thesis. Milan, Italy: Dipartimento di Elettronica, Politecnico di Milano (cit. on pp. 21, 22).

Dorigo, M., V. Maniezzo, and A. Colorni (1996). "Ant system: optimization by a colony of cooperating agents". In: *IEEE Transactions on Systems, Man, and Cybernetics, Part B (Cybernetics)* 26.1, pp. 29–41 (cit. on p. 22).

Dowson, D. (1962). "A generalized Reynolds equation for fluid film lubrication". In: *Int. J. Mech. Sci.* 4, pp. 159–170 (cit. on p. 44).

— (1979). *History of tribology*. Addison-Wesley Longman Limited (cit. on p. 1).

Dowson, D. and C. M. Taylor (1979). "Cavitation in bearings". In: *Annu. Rev. Fluid Mech.* 11.1, pp. 35–65 (cit. on p. 3).

Dubois, G.B., H.H. Mabie, and F.W. Ocvirk (1951). *Experimental investigation of oil film pressure distribution for misaligned plain bearings*. Tech. rep. KittyHawk, NC, USA: National Advisory Committee for Aeronautics (cit. on pp. 16, 17).

Durany, J., G. García, and C. Vázquez (2002). "Numerical simulation of a lubricated hertzian contact problem under imposed load". In: *Finite. Elem. Anal. Des.* 38.7, pp. 645–658 (cit. on pp. 20, 21).

Durany, J., J. Pereira, and F. Varas (2006). "A cell-vertex finite volume method for thermohydrodynamic problems in lubrication theory". In: *Comp. Meth. in Appl. Mech. and Eng.* 195.44, pp. 5949–5961 (cit. on p. 4).

— (2008). "Numerical solution to steady and transient problems in thermohydrodynamic lubrication using a combination of finite element, finite volume and boundary element methods". In: *Finite. Elem. Anal. Des.* 44.11, pp. 686–695 (cit. on pp. 20, 91).

Durany, J., J. Pereira, and F. Varas (2010). "Dynamical stability of journal-bearing devices through numerical simulation of thermohydrodynamic models". In: *Tribol. Int.* 43, pp. 1703–1718 (cit. on pp. 20, 21, 90, 91).

Durany, J. and C. Vázquez (1992). "Numerical Approach of Lubrication Problems in Journal Bearing Devices with Axial Supply". In: *Numerical Methods in Engineering* 92, pp. 839–844 (cit. on pp. 4, 19).

Eck, N. J. van and L. Waltman (2015). *VOSviewer. The Visualization of Science viewer*. v1.6.2. Leiden University. URL: http://www.vosviewer.com/Download (cit. on p. 14).

El Alaoui Talibi, M. and G. Bayada (1991). "Une méthode du type caractéristique pour la résolution d'un problème de lubrification hydrodynamique en régime transitoire". In: *ESAIM-Math. Model. Num.* 25.4, pp. 395–423 (cit. on p. 19).

Elrod, H. G. and M. L. Adams (1975). "A computer program for cavitation and starvation problems". In: *Cavitation and related phenomena in lubrication: proceedings of the 1st Leeds-Lyon Symposium on Tribology*. Mech. Eng. Publ, pp. 37–42 (cit. on p. 19).

Frêne, J., D. Nicolas, et al. (1997). *Hydrodynamic lubrication: bearings and thrust bearings*. Vol. 33. Elsevier (cit. on pp. 3, 9, 11, 12, 27, 30).

Gambardella, L. M., É. Taillard, and G. Agazzi (1999). "MACS-VRPTW: A multiple ant colony system for vehicle routing problems with time windows". In: *New Ideas in Optimization*. Ed. by D. Corne, M. Dorigo, and F. Glover. McGraw-Hill, London, UK. Chap. 5, pp. 63–76 (cit. on p. 22).

Garcia-Najera, A. and J. A. Bullinaria (2007). "Extending $ACO_{\mathbb{R}}$ to solve multi-objective problems". In: *Proceedings of the UK Workshop on Computational Intelligence*. London, UK (cit. on p. 23).

Gómez-Mancilla, J. and V. Nosov (2001). "Short journal bearing with misaligned axes". In: *Proceedings 1st International Symposium on control of rotating machinery* (cit. on pp. 16, 17, 27).

— (2002). "Perturbed pressure field solution for misaligned short journal bearings". In: *Proceedings 9th International Symposium on Transport Phenomena and Rotating Machinery. ISROMAC-9, Hawaii, EU* (cit. on pp. 4, 17, 78).

Guha, S. K. (2000). "Analysis of steady-state characteristics of misaligned hydrodynamic journal bearings with isotropic roughness effect". In: *Tribol. Int.* 33.1, pp. 1–12 (cit. on p. 24).

He, Z., J. Zhang, et al. (2012). "Misalignment analysis of journal bearing influenced by asymmetric deflection, based on a simple stepped shaft model". In: *Journal of Zhejiang University SCIENCE A* 13.9, pp. 647–664 (cit. on p. 24).

Holmberg, K. and A. Erdemir (2015). "Global impact of friction on energy consumption, economy and environment". In: *FME Trans* 43, pp. 181–185 (cit. on p. 3).

Jang, J. Y. and M. M. Khonsari (2004). "Design of bearings on the basis of thermohydrodynamic analysis". In: *Proceedings of the Institution of Mechanical Engineers, Part J: Journal of Engineering Tribology*. Vol. 218. 5. SAGE Publications, pp. 355–363 (cit. on p. 49).

— (2015). "On the Characteristics of Misaligned Journal Bearings". In: *Lubricants* 3.1, pp. 27–53 (cit. on pp. 1, 2, 17, 24).

Jang, J. Y., M. M. Khonsari, and S. Bair (2007). "On the elastohydrodynamic analysis of shear-thinning fluids". In: *Proceedings of the Royal Society of London A: Mathematical, Physical and Engineering Sciences*. Vol. 463. 2088. The Royal Society, pp. 3271–3290 (cit. on p. 24).

Knabner, P. and L. Angermann (2003). *Numerical methods for elliptic and parabolic partial differential equations*. Vol. 44. Springer Verlag (cit. on pp. 66, 69).

Kumar, P. and M. M. Khonsari (2009). "Traction in EHL line contacts using free-volume pressure-viscosity relationship with thermal and shear-thinning effects". In: *J. Tribol.* 131.1, p. 011503 (cit. on p. 24).

Leguizamón, G. and C. A. Coello (2010a). *A study of the scalability of ACO$_{\mathbb{R}}$ for continuous optimization problems*. Tech. rep. The Evolutionary Computation Group at CINVESTAV-IPN (cit. on p. 23).

— (2010b). "An Alternative ACO$_{\mathbb{R}}$ Algorithm for Continuous Optimization Problems". In: *Swarm Intelligence: 7th International Conference, ANTS 2010*. Vol. 6234. Lecture Notes in Computer Science. Brussels, Belgium: Springer Berlin Heidelberg, pp. 48–59 (cit. on pp. 23, 100).

Liao, T. (2011). "Improved ant colony optimization algorithms for continuous and mixed discrete-continuous optimization problems". MA thesis. Université Libre de Bruxelles, Belgium (cit. on p. 22).

Liao, T., M. A. Montes de Oca, et al. (2011). "An incremental ant colony algorithm with local search for continuous optimization". In: *Proceedings of the 13th annual conference on Genetic and evolutionary computation*. ACM, pp. 125–132 (cit. on pp. 23, 95).

Liao, T., T. Stützle, et al. (2014). "A unified ant colony optimization algorithm for continuous optimization". In: *European Journal of Operational Research* 234.3, pp. 597–609 (cit. on p. 23).

Liñan, A. (1999). *Curso de Mecánica de Fluidos*. Tech. rep. Universidad Politécnica de Madrid (cit. on p. 34).

Liu, G. (2004). "Dual variational principles for the free-boundary problem of cavitated bearing lubrication". In: *Complementarity, Duality and Symmetry in Nonlinear Mechanics: proceedings of the IUTAM Symposium*. Ed. by David Yang Gao. Vol. 6. Springer Science & Business Media, pp. 179–189 (cit. on p. 18).

Lombera, H. and J. I. Tello (2014). "A numerical approach to solve an inverse problem in lubrication theory". In: *RACSAM. Rev. R. Acad. A.* 108.2, pp. 617–631 (cit. on pp. 20, 21).

Luenberger, D. G. and Y. Ye (2008). *Linear and Nonlinear Programming*. Springer Science + Business Media, LLC. Chap. 9, p. 263 (cit. on p. 64).

Martin, S. (2005). "Contribution à la modélisation de phénomènes de frontière libre en mécanique des films minces". PhD thesis. INSA de Lyon (cit. on p. 93).

— (2008). "Influence of multiscale roughness patterns in cavitated flows: Applications to journal bearings". In: *Math. Probl. Eng.* 2008, pp. 1–26 (cit. on pp. 19, 24).

McKee, S. A. and T. R. McKee (1932). "Pressure distribution in oil films of journal bearings". In: *ASME* 54, pp. 149–165 (cit. on p. 16).

Moré, J. J. and D. J. Thuente (1994). "Line Search Algorithms with Guaranteed Sufficient Decrease". In: *ACM Transactions on Mathematical Software* 20, pp. 286–307 (cit. on pp. 93, 98).

Nikolakopoulos, P. G. and C. A. Papadopoulos (1994). "Non-linearities in misaligned journal bearings". In: *Tribol. Int.* 27.4, pp. 243–257 (cit. on p. 17).

Nocedal, J. and S. J. Wright (2006). *Numerical Optimization*. 2nd ed. Springer Science + Business Media, LLC (cit. on pp. 21, 71, 72, 93).

Ocvirk, F. W. and G. B. DuBois (1953). *Analytical derivation and experimental evaluation of short-bearing approximation for full journal bearings*. Tech. rep. 1157. NACA (cit. on p. 12).

Osman, T. A. (2001). "Misalignment effect on the static characteristics of magnetized journal bearing lubricated with ferrofluid". In: *Tribol. Lett.* 11.3-4, pp. 195–203 (cit. on p. 24).

Pedraza, G., M. Díaz, and H. Lombera (2016). "An Approach for Assembly Sequence Planning by Genetic Algorithms". In: *IEEE Latin America Transactions* 14.5, pp. 2066–2071 (cit. on p. 23).

Pierre, I., J. Bouyer, and M. Fillon (2002). "Thermohydrodynamic study of misaligned plain journal bearings-comparison between experimental data and theoretical results". In: *Applied Mechanics and Engineering* 7.3, pp. 949–960 (cit. on p. 24).

Pierre, I., E. de France, et al. (2004). "Thermohydrodynamic Behavior of Misaligned Plain Journal Bearings: Theoretical and Experimental Approaches". In: *Tribol. Trans.* 47.4, pp. 594–604 (cit. on pp. 24, 74, 84).

Piggott, R. J. S. (1942). "Bearings and lubrication. Bearing troubles traceable to design can be avoided by engineering study". In: *Mech. Eng.* 64, p. 259 (cit. on p. 16).

Piniganti, L. (2014). "A Survey of Tabu Search in Combinatorial Optimization". MA thesis. University of Nevada, Las Vegas (cit. on p. 23).

Pinkus, O. and S. S. Bupara (1979). "Analysis of misaligned grooved journal bearings". In: *J. Tribol.* 101.4, pp. 503–509 (cit. on pp. 17, 78).

Pinkus, O. and B. Sternlicht (1961). *Theory of hydrodynamic lubrication*. McGraw-Hill, New York (cit. on p. 17).

Pope, J. E. (1996). *Rules of thumb for mechanical engineers*. Gulf Professional Publishing (cit. on p. 1).

Quarteroni, A., R. Sacco, and F. Saleri (2007). *Numerical Mathematics*. 2nd ed. Springer Berlin Heidelberg (cit. on p. 90).

Reynolds, O. (1886). "On the theory of lubrication and its application to Mr. Beauchamp Tower's experiments, including an experimental determination of the viscosity of olive oil." In: *Phil. Trans. Roy. Soc. A* 117, pp. 157–234 (cit. on p. 10).

Roache, P. J. (1994). "Perspective: a method for uniform reporting of grid refinement studies". In: *J. Fluids Eng.* 116.3, pp. 405–413 (cit. on pp. 82, 83, 107–109).

— (1998). *Verification and validation in computational science and engineering*. Albuquerque, New Mexico: Hermosa (cit. on pp. 82, 83, 107, 108).

— (2002). "Code verification by the method of manufactured solutions". In: *Journal of Fluids Engineering* 124.1, pp. 4–10 (cit. on pp. 82, 107).

Rodrigues, J. F. (1993). "Remarks on the Reynolds problem of elastohydrodynamic lubrication". In: *Eur. J. Appl. Math.* 4.01, pp. 83–96 (cit. on p. 18).

Rohde, S.M. and G.T. McAllister (1975). "A variational formulation for a class of free boundary problems arising in hydrodynamic lubrication". In: *Int. J. Eng. Sci.* 13.9-10, pp. 841–850 (cit. on p. 18).

Sharma, S. C., S. C. Jain, and T. Nagaraju (2002). "Combined influence of journal misalignment and surface roughness on the performance of an orifice compensated non-recessed hybrid journal bearing". In: *Tribol. Trans.* 45.4, pp. 457–463 (cit. on p. 24).

Siarry, Patrick, Gérard Berthiau, et al. (1997). "Enhanced simulated annealing for globally minimizing functions of many-continuous variables". In: *ACM Transactions on Mathematical Software (TOMS)* 23.2, pp. 209–228 (cit. on p. 23).

Socha, K. (2008). "Ant Colony Optimization for Continuous and Mixed-Variable Domains". PhD thesis. Belgium: Université Libre de Bruxelles (cit. on pp. 23, 97, 98).

Socha, K. and M. Dorigo (2008). "Ant colony optimization for continuous domains". In: *European Journal of Operational Research* 185.3, pp. 1155–1173 (cit. on pp. 23, 94, 95, 98).

Srinivas, M. and L. M. Patnaik (1994). "Genetic algorithms: A survey". In: *Computer* 27.6, pp. 17–26 (cit. on p. 23).

Stachowiak, G. and A. W. Batchelor (2013). *Engineering tribology*. Butterworth-Heinemann (cit. on pp. 1–3, 10, 11, 24).

Stieber, W. (1933). *Das Schwimmlager*. Tech. rep. Ver. Dtsch. Ing. (Berlin) (cit. on pp. 12, 41).

Stützle, T. and H. Hoos (2000). "MAX-MIN Ant System". In: *Future generation computer systems* 16.8, pp. 889–914 (cit. on pp. 22, 96, 97).

Sun, J., M. Deng, et al. (2010). "Thermohydrodynamic lubrication. Analysis of misaligned plain journal bearing with rough surface". In: *J. Tribol.* 132.1, p. 011704 (cit. on p. 24).

Sun, J., X. Zhu, et al. (2014). "Effect of surface roughness, viscosity-pressure relationship and elastic deformation on lubrication performance of misaligned journal bearings". In: *Industrial Lubrication and Tribology* 66.3, pp. 337–345 (cit. on p. 24).

Swift, H. W. (1932). "The stability of lubricating films in journal bearings". In: *Journal of Institution of Civil Engineers* 233.Part 1, pp. 267–288 (cit. on pp. 12, 41).

Thomsen, K. and P. Klit (2012). "Improvement of journal bearing operation at heavy misalignment using bearing flexibility and compliant liners". In: *Proceedings of the Institution of Mechanical Engineers, Part J: Journal of Engineering Tribology* 226.8, pp. 651–660 (cit. on p. 24).

Vijayaraghavan, D. and T.G. Keith (1989). "Effect of cavitation on the performance of a grooved misaligned journal bearing". In: *Wear* 134.2, pp. 377–397 (cit. on p. 19).

— (1990). "Analysis of a finite grooved misaligned journal bearing considering cavitation and starvation effects". In: *J. Tribol-T. ASME.* 112.1, pp. 60–67 (cit. on pp. 4, 17, 19, 78).

Williams, J. (2005). *Engineering Tribology*. Cambridge University Press. 512 pp. (cit. on p. 80).

Xu, G., J. Zhou, et al. (2015). "Research on the static and dynamic characteristics of misaligned journal bearing considering the turbulent and thermohydrodynamic effects". In: *J. Tribol.* 137.2, p. 024504 (cit. on p. 24).

Zhang, Y., S. Wang, and G. Ji (2015). "A comprehensive survey on particle swarm optimization algorithm and its applications". In: *Mathematical Problems in Engineering* 2015 (cit. on p. 23).

Zienkiewicz, O. C. and R. L. Taylor (2000). *The Finite Element Method*. 5th ed. Vol. 1. The Basis. Butterworth-Heinemann (cit. on p. 62).

Printed in: Polytechnic University of Madrid

Generated with LaTeX 2_ε: Tuesday 21st November, 2017: 11:14am